UCLA
UCLA Electronic Theses and Dissertations

Title

Investigating Basal Ganglia Circuitry and Function using Silicon Microprobes and Optogenetic Techniques

Permalink

https://escholarship.org/uc/item/01z5q78d

Author

Claar, Leslie

Publication Date

2018

Peer reviewed|Thesis/dissertation

UNIVERSITY OF CALIFORNIA

Los Angeles

Investigating Basal Ganglia Circuitry and Function

using Silicon Microprobes and Optogenetic Techniques

A dissertation submitted in partial satisfaction of the

requirements for the degree

Doctor of Philosophy in Bioengineering

by

Leslie Dyan Claar

2018

ABSTRACT OF THE DISSERTATION

Investigating Basal Ganglia Circuitry and Function

using Silicon Microprobes and Optogenetic Techniques

by

Leslie Dyan Claar

Doctor of Philosophy in Bioengineering

University of California, Los Angeles, 2018

Professor Sotirios Masmanidis, Co-Chair

Professor Wentai Liu, Co-Chair

The basal ganglia are a system of subcortical nuclei that are known to be involved in
movement, reward processing, associative learning, and some forms of memory. Basal ganglia
disorders, such as Parkinson's disease and Huntington's disease, cause a wide range of severe
motor impairments. In addition, the basal ganglia have been implicated in a multitude of
neuropsychiatric disorders, including obsessive-compulsive disorder, Tourette syndrome, and
even depression and addiction. Progress has been made in the last century to map out basal
ganglia circuitry, identify its inputs and outputs, and elucidate its functions. However, due to its
complexity, many questions remain. Here we aimed to study the basal ganglia by exploring
interactions between nuclei and important input structures, examining neural activity in the most
prominent nucleus during movement generation, and investigating the role of inputs during

reward-guided behaviors. Chapter one discusses the development of a three-dimensional silicon microprobe capable of simultaneously recording extracellular activity from hundreds of neurons spatially distributed throughout the basal ganglia and input structures such as the cortex and ventral tegmental area. Chapter two examines activity of the direct and indirect pathways, the two major pathways from basal ganglia input to output. It describes coordinated activation of optogenetically identified cells measured in the striatum during motivated movement initiation. Chapter three describes optogenetic manipulation of dopaminergic signaling during reward-guided behavior and provides strong causal evidence that phasic dopamine responses to rewarding stimuli are necessary and sufficient for associative learning. Taken together these findings have significant implications for basal ganglia function.

The dissertation of Leslie Dyan Claar is approved.

Mark S. Cohen

Dejan Markovic

Wentai Liu, Committee Co-Chair

Sotirios Masmanidis, Committee Co-Chair

University of California, Los Angeles

2018

This work is dedicated to the mice without whose sacrifice this dissertation would lack substance. Thank you for licking when I wanted you to (for the most part) and only biting me a few times.

TABLE OF CONTENTS

LIST OF FIGURES

CHAPTER 3

ABBREVIATIONS

3D	three-dimensional
A2a	adenosine A2a receptor
AAV	adeno-associated vector
ACSF	artificial cerebrospinal fluid
ADC	analog to digital conversion
Ag	silver
ANOVA	analysis of variance
Au	gold
BG	basal ganglia
CCG	cross correlogram
Cl	chloride
CR	conditioned response
CS	conditioned stimulus
CS-	conditioned stimulus paired with nothing
CS+	conditioned stimulus paired with reward
CTX	orbitofrontal cortex
D1	D1-type dopamine receptor
D2	D2-type dopamine receptor
DAT	dopamine transporter
FC	functionally connected
FSI	fast-spiking interneuron
GABA	*gamma*-Aminobutyric acid

GP	globus pallidus
GPe	external segment of the globus pallidus
ITI	inter-trial interval
LFP	local field potential
MDB	midbrain
MEMS	microelectromechanical systems
MSN	medium spiny neuron
NA	numerical aperture
NpHR3.0	halorhodopsin
PBS	phosphate-buffered saline
PCA	principal component analysis
PCB	printed circuit board
pSTR	posterior striatum
Pt	platinum
RM	repeated measures
$r_{observed}$	observed correlation coefficient
RPE	reward prediction error
r_{rest}	resting state correlation
$r_{shuffled}$	shuffled correlation coefficient
r_{signal}	signal correlation
s.c.	subcutaneous
SALT	Stimulus-Associated spike Latency Test
SEM	standard error of the mean

Si	silicon
SN	substantia nigra
SNc	substantia nigra pars compacta
SNr	substantia nigra pars reticulata
SNR	signal-to-noise ratio
SPN	spiny projection neuron
STN	subthalamic nucleus
STR	striatum
TAN	tonically active neuron
US	unconditioned stimulus
VTA	ventral tegmental area
YFP	yellow fluorescent protein

EDUCATION

B.S., Biological Systems Engineering, with Honors   **2011**

University of California, Davis

PUBLICATIONS

J.L. Shobe*, L.D. Claar*, S. Parhami, K.I. Bakhurin, and S.C. Masmanidis. Brain activity
mapping at multiple scales with silicon microprobes containing 1,024 electrodes. *Journal of
Neurophysiology, 114 (3): 2043-2052 (2015).* *co-first author

J.L. Shobe, K.I. Bakhurin, L.D. Claar, and S.C. Masmanidis. Selective modulation of
orbitofrontal network activity during negative occasion setting. *Journal of Neuroscience, 37
(39): 9415-9423 (2017).*

K.I. Bakhurin, V. Goudar, J.L. Shobe, L.D. Claar, D.V. Buonomano, and S.C. Masmanidis.
Differential Encoding of Time by Prefrontal and Striatal Network Dynamics. *Journal of
Neuroscience, 37 (4): 854-870 (2017).*

W.C. Smith, M.H. Rosenberg, L.D. Claar, V. Chang, S.N. Shah, W.M. Walwyn, C.J. Evans, and
S.C. Masmanidis. Frontostriatal Circuit Dynamics Correlate with Cocaine Cue-Evoked
Behavioral Arousal during Early Abstinence. *eNeuro, 3 (3): online (2016).*

INTRODUCTION

The basal ganglia represent the largest subcortical structures in the human forebrain [2]. They receive inputs from large areas of the cortex and have a significant influence over thalamic neurons that project back to the cortex and ultimately to the brainstem. It is for these reasons that the basal ganglia are thought to have profound influence over brain functions. Individual basal ganglia nuclei were first anatomically described by a series of scientists over a period spanning the 17th through the 19th centuries [3]. At this point in history scientists were just beginning to observe connectivity between these distinct regions in the basal ganglia, and also began speculating about their function. In the 20th century, however, scientists performing pathological and physiological studies of patients suffering from basal ganglia disorders shed some light on the functions of these interconnected nuclei [4].

The striatum, the main input hub of the basal ganglia, primarily receives excitatory glutamatergic input from many cortical areas, and dense modulatory dopaminergic innervation from the ventral tegmental area and the substantia nigra pars compacta. The striatum sends afferents to the basal ganglia output nucleus called the substantia nigra pars reticulata, via two pathways: the direct pathway and the indirect pathway. Early publications describing the two pathways proposed that the direct and indirect likely had opposing effects on the thalamic targets and, potentially, motor control as well [5]–[7]. This model was largely supported by physiological studies of patients with movement disorders. For example, in Parkinson's disease the dopamine neurons in the substantia nigra pars compacta degenerate and lead to an imbalance of activity between the direct and indirect pathways which is thought to be the cause of hypokinetic motor symptoms [5]. Huntington's disease is marked by degeneration of neurons in the striatum, typically indirect pathway neurons first [8], and is characterized by hyperkinetic

motor symptoms [5]. This classical, antagonistic model of direct and indirect pathway function has been supported via causal behavioral experiments [9]. However more recently, there is evidence that supports a more nuanced model suggesting coordinated activity in both pathways occurs during movement generation [10]–[13]. Further studies are needed to elucidate the function of basal ganglia nuclei with regard to motor control.

In addition to being strongly linked to severe motor impairments, the basal ganglia have also been implicated in neuropsychiatric disorders such as obsessive-compulsive disorder and schizophrenia and are involved in some types of learning [2]. Evidence suggests that the striatum, in particular, is an important information processing center and site of plasticity in reinforcement learning [14]–[17]. Consistent with this theory, the striatum is known to receive dense dopaminergic innervation [5], [15], [18] and many studies have supported the role of dopamine as a neural substrate for reward prediction error learning models [19]–[23].

The basal ganglia and related circuits are thought to participate in motor control and reward learning, as mentioned above, and many other processes, such as action selection, arousal, and memory [24]. It is a well-studied group of nuclei in terms of both structure and function, however many questions remain unanswered. With the innovations in neuroscience techniques that allow for larger-scale electrophysiology with higher temporal and spatial resolution, specific targeting of genetically defined cell populations, and bidirectional, temporally precise control over neuronal activity, the basal ganglia field is well poised to answer these questions. This work describes the development, characterization, and implementation of innovative techniques for studying basal ganglia circuitry and function.

Due to the distributed nature of the basal ganglia nuclei, new tools that allow simultaneous monitoring of distal regions that span a three-dimensional volume are needed.

Chapter one describes how we precisely assembled a recording device that could simultaneously record from multiple nuclei in the basal ganglia and important input structures such as the cortex and the ventral tegmental area. The device consisted of four two-dimensional microprobes precisely placed to target the regions of interest, with a total of 1,024 electrodes. In addition to building the probe device, hardware and software was developed to support experimental automation and data acquisition. We then validated the technology by performing recordings in mice participating in a Pavlovian conditioning task. The data showed that task-evoked neuron population activity was very similar between the rewarded and unrewarded cue at an interregional level. In addition, we identified significant signal and resting state correlations between neurons from the same as well as different regions. Recordings of this scale in awake, behaving mice can reveal multiregional circuit dynamics and can potentially answer long-standing questions concerning basal ganglia function.

The technology discussed in chapter one allowed us to record from ~50-100 well-isolated neurons in each of the targeted regions. We were able to putatively identify neuron types based on spike waveform and firing rate characteristics [16], [25]. Chapter two describes the characterization and implementation of an optogenetic photo-tagging protocol for use with our silicon microprobes upgraded with attached optical fibers. We aimed to study the direct and indirect pathways of the basal ganglia by performing electrophysiological recordings of striatal neurons and by examining neural activity dynamics in the D1 and D2 dopamine receptor expressing neuron populations [26]. Using the Stimulus-Associated spike Latency Test [27] and a spike waveform correlation threshold we positively identified 87 neurons expressing the D1 receptor and belonging to the direct pathway and 74 neurons expressing the D2 receptor and belonging to the indirect pathway. We examined the firing dynamics of these positively

identified neurons while the mice were licking in response to a reward-predicting odor stimulus. We showed that both populations increased their mean firing rate during lick initiation. This finding is consistent with recent evidence suggesting that the direct and the indirect pathways are co-activated during movement generation [12], [13]. We also observed a significantly increased reward response in the D1 neurons compared to the D2 neurons. This is consistent with the idea that reward delivery triggers dopamine release in the striatum and D1 dopamine receptor expressing neurons are positively modulated by dopamine signaling [15], [28]. Chapter two demonstrates that optogenetic identification of neuronal subtypes in the striatum can further elucidate the role of these two pathways in the basal ganglia.

The ventral tegmental area and substantia nigra pars compacta contain dopamine neurons that send efferent projections to a large portion of the basal ganglia. Dopamine is known to play a role in motor control as evidenced by the fact Parkinson's disease is characterized by dopamine neuron loss and results in severe movement disorders [5]. There is also evidence supporting dopamine as the neural substrate for reward prediction error in associative learning tasks [19]–[23]. Chapter three describes a set of experiments involving optogenetic manipulation of dopamine signaling during performance of a learned Pavlovian association task. To our knowledge, this is the first study involving bidirectional modulation of dopamine neurons with precise temporal control in a Pavlovian conditioning task. We showed that dopamine neuron inhibition during reward consumption can cause extinction even in the presence of the food reward, and dopamine neuron stimulation can prevent extinction even in absence of the food reward. Dopamine signaling at the time of reward is both necessary and sufficient to maintain the learned association between a conditioned stimulus and a reward. We performed a temporal dissection of the reward-evoked dopamine response by incrementally varying the delay between

4

the food reward and the dopamine neuron inhibition and showed that the dopamine response to the reward is necessary for approximately 500 ms following reward delivery. Surprisingly, we did not find a significant behavioral effect when we inhibited dopamine neurons during the odor cue delivery and the delay period. These results support the proposed role of dopamine in reward learning and maintenance of cue-reward associations.

This dissertation provides details regarding the development, characterization, and implementation of innovative techniques for studying basal ganglia circuitry and function. Together, these findings give a clearer picture of basal ganglia neural activity patterns and function in a Pavlovian conditioning task. Our studies implementing large-scale electrophysiological recordings in distributed basal ganglia circuits, optogenetic identification of neuronal subtypes, and optogenetic manipulation of behavioral output support basal ganglia participation in stimulus and reward processing, motivated motor control, and reinforcement learning.

CHAPTER 1

Brain activity mapping at multiple scales with silicon microprobes containing 1,024 electrodes

This chapter is a reproduction of an article published in *Journal of Neurophysiology* [1]. This work was co-authored by Justin Shobe, Leslie Claar, Sepideh Parhami, Konstantin Bakhurin, and Sotiris Masmanidis. Acknowledgements are detailed in the Acknowledgements section (xiii) of the dissertation and at the end of this chapter.

1.1 Abstract

The coordinated activity of neural ensembles across multiple interconnected regions has been challenging to study in the mammalian brain with cellular resolution using conventional recording tools. For instance, neural systems regulating learned behaviors often encompass multiple distinct structures that span the brain. To address this challenge we developed a three-dimensional (3D) silicon microprobe capable of simultaneously measuring extracellular spike and local field potential activity from 1,024 electrodes. The microprobe geometry can be precisely configured during assembly to target virtually any combination of four spatially distinct neuroanatomical planes. Here we report on the operation of such a device built for high throughput monitoring of neural signals in the orbitofrontal cortex and several nuclei in the basal ganglia. We perform analysis on systems-level dynamics and correlations during periods of conditioned behavioral responding and rest, demonstrating the technology's ability to reveal functional organization at multiple scales in parallel in the mouse brain.

1.2 Introduction

Extracellular microelectrode arrays provide large-scale measurements of neural spiking and local oscillatory fields that are currently not possible with other recording techniques [29]. Generally, conventional electrode arrays with tens of sites are deployed in single anatomical areas, or divided across multiple areas [30]. But these configurations provide a sparse view of how local neural information processing is coordinated across anatomically distributed circuits. Thus, there is a strong need to increase the number of electrodes at multiple spatial scales, at the

level of both local microcircuits as well as macroscopic circuits containing distally located interconnected regions [31].

The challenge of realizing recordings at multiple length scales has been addressed to some degree by implanting a large number of electrode microwires [32], or by relying on microfabrication techniques to increase the density of electrode arrays [33]–[36]. However, further increasing the electrode number, density, or the number of regions sampled in parallel may pose difficulties with these approaches in terms of device fabrication, assembly, or tissue displacement. An alternative approach to monitoring activity is to image calcium dynamics; however, calcium imaging is inherently limited in its temporal resolution, and given existing methods it is not possible to observe more than two separate regions in parallel in the mammalian brain [37]. Scalability with current electrode and optical-based tools is especially challenging in the mouse. Mice are an attractive mammalian model for studying brain network dynamics in light of their genetic accessibility, but their relatively small size presents a significant obstacle in terms of accessible space and weight load on the head. Fortunately, a variety of behavioral tasks have been adapted for recordings in head-fixed animals [38], [39], which could mitigate potential size and weight limitations of a large-scale recording system. One approach to developing such a system in a mouse would involve placement of multiple high-density, minimally invasive electrode arrays throughout the brain. These recording tools could dramatically expand the ability to study brain dynamics in the awake behaving mouse, helping to link different scales of brain function, and informing computational and network science approaches to modeling neural systems.

Here we leverage advancements in silicon device microfabrication and assembly techniques to develop a three-dimensional (3D) microelectrode array that can be precisely

configured to record from four distinct regions in the mouse brain. The microprobe is built to densely sample activity from local microcircuits with miniaturized silicon prongs containing up to 64 closely packed electrodes, as well as macroscopic circuits using over a dozen such prongs separated by submillimeter length scales. We introduce a 3D microprobe containing 1,024 electrodes monitored in parallel, surpassing the number of simultaneously recorded signals of other in vivo electrode arrays. We evaluate the technology's capabilities by capturing task-evoked and resting state network dynamics in awake head-fixed mice responding to olfactory and appetitive stimuli. This technology has broad applicability in systems-level neuroscience due to its customizable 3D configuration and ability to provide large-scale and high throughput electrophysiological data.

1.3 Materials and Methods

3D silicon microprobe recording system development

In order to develop a technology suitable for mapping brain activity at multiple scales in the mouse, we addressed several technical challenges related to high-density electrode array fabrication, instrumentation to monitor electrical signals, and assembly. First, we relied on wafer-scale microfabrication techniques for the production of newly designed silicon devices with microelectrodes dispersed along implantable silicon prongs (Fig. 1A). The fabrication was carried out in a silicon microelectromechanical systems (MEMS) foundry (Innovative Micro Technology) on 150 mm silicon-on-oxide wafers. The fabrication process was adapted from a previously described method resulting in submicron electrical interconnects [40], but was improved in terms of device yield thanks to the larger wafer diameter (now producing over 200

functional probes per wafer) and maximum number of electrodes per device (now increased to 256). Fabrication involved a combination of material deposition (Au for the electrodes, leads and wire bond contacts, stress-free silicon nitride for the upper and lower dielectric layers), photolithography for masking, and dry etching processes with various chemistries to selectively and nonisotropically pattern metal, dielectrics, and silicon. Following fabrication, devices were released from a carrier substrate by immersing in water heated to 80°C, cleaned with deionized water and ethanol, and stored for later use.

The minimum device feature size was 0.4 μm, corresponding to the narrowest width of the conducting Au wires. The microprobes consisted of 22 μm thick Si for mechanical support, ~0.5 μm bottom insulating nitride, 0.1 μm Au, and ~0.5 μm top nitride layers. To enable high-density recordings from local microcircuits, up to 64 electrodes were patterned on the top face of each silicon prong. The Au recording sites had dimensions of 10 μm x 10 μm and a center-to-center neighbor spacing of 25 μm, except near the tips, where spacing was slightly modified to accommodate the tapered prong profile. The 25 μm spacing was selected to provide a dense and often redundant sampling of extracellular fields along the depth of the array, and was based on prior experimental measurements and biophysical models [41], [42]. Prongs had a maximal width of 86 μm that tapered to a point at the tip, and were separated by 300 to 400 μm to provide sampling at multiple proximal locations in the same or nearby brain structure. Thus the overall silicon prong dimensions were 7 mm x 86 μm x 23 μm (l x w x t).

Devices containing 256 electrodes were attached and wire bonded to a custom-built printed circuit board (PCBs manufactured at Hughes Circuits; wire bonding at IDAX Microelectronics). PCBs contained four compact 64 pin electrical connectors (Molex Inc, Slimstack 502430-6410) for head stage access (Fig. 1B). The wire bond pads were encapsulated

with epoxy (Resinlab EP965 black), which was cured at 50 °C. Each recording site was gold

plated (Sifco 80535500) with constant potential pulses (-2.5 V relative to a Pt wire reference, 1-5

seconds) to reduce impedance below 0.5 MΩ in order to improve the signal-to-noise ratio (SNR)

[40].

To extend the recording tools into the third dimension for making simultaneous

recordings from multiple distinct areas, we developed an assembly method for rigidly combining

four separate layers. Each layer consisted of a 256 electrode array bonded to a PCB. To permit

electrical access to the interior PCBs, two of the layers, targeting the outermost areas, were

electrically connected to narrow PCBs, whereas the two inner layers were connected to wide

PCBs (Fig. 1B). During assembly, the position and orientation of silicon prongs in each layer

was controlled with micrometer precision using a motorized micromanipulator providing

translation in three axes (Sutter Instruments MP-285), as well as optomechanical parts providing

roll and pitch (Thor Labs dual axis goniometer GN2), and yaw (Thor Labs rotation platform

RP01). The combined positioning system provided 6 independently controlled degrees of

freedom to achieve 3D alignment of four electrode arrays. The first layer in the 3D microprobe

was bonded with epoxy to an aluminum rod for mechanical support (Fig. 1C). Each successive

layer was aligned and then rigidly and permanently bonded together for mechanical support

before adding the next layer (Fig. 1D).

Here we demonstrate this technology with a 3D configuration targeting several

interconnected nuclei in the basal ganglia including the striatum, globus pallidus (GP), ventral

tegmental area (VTA), and substantia nigra (SN), and the orbitofrontal cortex, which projects to

the striatum [43]. To specifically target these structures in the mouse, we spaced successive

silicon layers by ~1 to 3 mm. Collectively, this 3D microprobe contained 1,024 recording sites

with precisely known spatial positions (Fig. 1E).

We used a multiplexed signal readout method to minimize the recording system's

external wiring requirements [40], which reduced the external cable to just 65 wires (Fig. 1F).

Readout was achieved via 8 custom-built 128 channel detachable head stage modules (Fig. 1B).

Head stages contained commercial integrated electronic circuits (Intan Technologies RHA-

2164B) [44] providing signal multiplexing (32 electrodes per multiplexed output wire),

amplification (gain=200), and filtering (0.1-8000 Hz) functions. Each head stage contained two

64 pin connectors (Molex Inc, Slimstack 502426-6410) connecting to the PCBs bonded to the

silicon microprobes. Analog signals were transmitted through thin flexible cables and

subsequently digitized on four 16 bit analog to digital conversion (ADC) cards (USB-6356,

National Instruments), each card supporting 256 channels, and each channel representing one

recording electrode. Signals from all 1,024 channels were simultaneously and continuously

sampled at a rate of 25 kHz per channel, with some representative signals that were filtered

offline shown in Fig. 1G. There was a sampling delay of 40 μs between the first and last channel

corresponding to the multiplexed switching time, but since this delay is significantly less than

electrophysiological timescales of action potentials it does not degrade the overall system

performance. Mouse behavioral parameters including licking activity and spherical treadmill

rotation were monitored at a rate of 10 kHz with an additional ADC card (USB-6351, National

Instruments). All ADC cards were synchronized via a shared internal clock. Local field

potential (LFP) signals were downsampled offline to 1 kHz. All data acquisition, as well as

control of stimulus timing was performed with custom LabVIEW scripts. All data analysis was

carried out with custom Matlab scripts.

Animal surgical, behavioral, and recording procedures

All procedures were approved by the University of California, Los Angeles Chancellor's Animal Research Committee. Singly housed male C57Bl/6J mice (n=6, 12-16 weeks old, The Jackson Laboratory) were used in the experiments. Animals underwent an initial surgery under isoflurane anesthesia in a stereotaxic apparatus to bilaterally fix stainless steel head restraint bars on the skull (10 mm x 7.5 mm, 0.6 g, laser cut at Fab2Order). Animals were anesthetized with isoflurane for a second surgery on the recording session day to make three rectangular craniotomies for microprobe insertion. The dura mater was opened to facilitate insertion. An additional craniotomy was made over the posterior cerebellum for placement of an electrical reference wire.

After recovery from the first surgery, animals were food restricted and fed daily after each training session to maintain ~90% of their baseline weight. They received water ad libitum. During daily training sessions, animals were mounted with the head bar bracket on a behavioral testing rig and on top of a rotatable spherical treadmill (200 mm diameter, Graham Sweet Studios, free to rotate forward and backward when animals walk or run). The treadmill's linear velocity was monitored with an optical mouse [45]. A reward solution (5 µL, 10% sweetened condensed milk) was dispensed from a tube positioned between an infrared beam lick meter (Island Motion), and its delivery was signaled by an audible solenoid valve actuation (Neptune Research 161T010). Initially, animals were habituated to head fixation and trained to respond to reward. During these sessions mice received rewards alone (lick tube; maximum 100 rewards per session, 13-21 s inter-trial interval, ITI), and a constant flow of odorless air (1.5 L/min) through an air tube. Thus mice learned to associate the solenoid actuation sound with a reward, and after consuming at least 90% delivered rewards for two consecutive days, they began

Pavlovian conditioning with olfactory cues. Odorants were introduced via an olfactometer by bubbling air (0.15 L/min) through aromatic liquids diluted 1:10 in mineral oil (Sigma-Aldrich), and mixing this product with the 1.5 L/min main stream of air. Odors were presented in pseudorandom order (1s duration, 17-29 s ITI, 100 rewarded CS+ and 100 unrewarded CS- trials). The odor corresponding to CS+ trials was amyl acetate, and citral for CS- trials. During training mice began to lick in anticipation of the reward (in the interval between odor and reward; 0-2.5 s). In the recording session animals received 100 CS+ with 85% reward probability and 100 CS- stimuli with no reward. To quantify performance, a correct CS+ trial was defined as initiation of licking 0-2.5 s post cue onset. A correct CS- trial was defined as withholding of licking 0-5 s post cue onset.

After the craniotomy surgery, animals recovered from anesthesia in their home cage for ~2 hr before being placed on the testing rig. An Ag/AgCl reference wire was placed on the cerebellar surface, covered in ACSF-saturated water absorbing foam (Gelfoam, Pfizer) to improve electrical contact, and sealed with silicone elastomer (Kwik-Cast, WPI). The silicon microprobes were coated with fluorescent dye (Invitrogen DiD), and slowly lowered to stereotaxically defined coordinates with a micromanipulator (MP-285, Sutter Instruments). The insertion was monitored with a surgical microscope (Zeiss OPMI pico). After reaching the target depth a drop of mineral oil was placed on the exposed cortical surface, and a 45 min settling period elapsed before beginning the behavioral task and data acquisition. Mice were given occasional rewards (every 2-5 min) during the settling period to help maintain a high level of motivation. Following each recording probes were cleaned in trypsin solution (Invitrogen), rinsed with deionized water and ethanol, and stored for reuse.

Histology and electrode position determination

Following each experiment, the brain was coronally sectioned at 100 μm on a -20 °C cryostat and individual sections were placed in order into a 24 well plate containing cold cryoprotectant solution. We then performed immunohistochemistry using standard procedures on slices in the regions of interest to determine the exact placement of the silicon prongs in each region. Sections were stained for neuronal nuclei with rabbit α NeuN (Cell Signaling Technology D3S3I) and for dopamine terminals with sheep α tyrosine hydoxylase (Millipore AB1542), in addition to the DiD which diffusively labeled tissue near the probe insertion sites. Each of the 1,024 recording sites were assigned a coordinate in 3D Cartesian space based on the expected location relative to bregma, and assigned to a brain region based on brain slice confocal imaging (Fig. 2A). The following possible region assignments were used: orbitofrontal cortex (CTX); anterior striatum (STR); posterior striatum (pSTR); globus pallidus (GP); VTA; SN; other midbrain areas; and other unspecified areas. The single-unit analysis did not use signals from other midbrain areas outside the VTA and SN, or other unspecified areas. Furthermore, data from the VTA and SN were combined. Local field potential (LFP) coherence maps were constructed using all recording sites.

Spike sorting and single-unit position determination

The 1,024 electrode array was first subdivided into multiple sets of 2 to 5 local electrodes. Due to the proximity of neighboring recording sites, units were often recorded on multiple electrodes (Fig. 2B). To minimize globally correlated signal artifacts, the mean background signal was removed from each electrode by subtracting the mean voltage of all electrodes on the corresponding silicon prong. Signals were then filtered in the 600-6500 Hz band, and spikes were detected on the spike trough with an SNR threshold of ~3 (Fig. 2C).

Putative units were then isolated on this local set of electrodes. We isolated units by automatically generating waveform-based templates using data from the first 5 min of the recording session, and then matching spikes from the entire session to those templates. Possible duplicate units occurring on more than one local set of electrodes were automatically identified by comparing mean spike waveform, and discarded. Time stamps from the remaining units were used to repeat waveform collection under a wider frequency band (300-6500 Hz) for visualization and manual scoring. Finally, all units were manually inspected and discarded if their waveforms appeared to represent a signal artifact, or if they did not meet minimum waveform amplitude (50 µV) or spike number criteria (at least 150 across the recording session). Based on the targeted electrode positions, single units were assigned an estimated 3D coordinate as well as a histologically determined brain region. The estimated position coincided with the recording site exhibiting the highest spike amplitude for that unit (Fig. 2B).

Signal and resting state neural correlations

For signal correlations (r_{signal}) we calculated the Pearson correlation coefficient from the mean cue-triggered firing rate during correct CS+ trials 0-2.5 s after cue onset, in 50 ms bins. For resting state correlations (r_{rest}) we defined resting periods as intervals of at least 2 s during which animals did not make any movements (running, licking) and were not presented with any external stimuli (cues and reward). We serially concatenated spiking activity occurring within these epochs to create a continuous time series vector (maximum 500 s, 50 ms bins) representing the resting state activity. We calculated resting state activity for each individual unit, and then obtained the pairwise Pearson correlation coefficient corresponding to r_{rest} using these vectors. To identify significant resting state correlations, we performed a permutation test for correlations

(see Statistical Tests). We defined a pair of units as significantly correlated, hence functionally connected (FC), if the test showed a p-value of less than 0.01.

K-means clustering

The signal correlation of evoked unit activity during correct CS+ trials was clustered using a custom k-means algorithm. K-means clustering was performed separately in five regions (cortex, striatum, posterior striatum, GP, and VTA/SN). Based on a qualitative assessment of cluster quality, the number of clusters k into which cells were grouped was set to three in the cortex and striatum and two in the posterior striatum, GP, and VTA/SN nuclei. Results were compiled into a single correlation matrix containing five nested matrices representing the independently calculated intraregional k-means clusters, as well as interregional signal correlation values which were not explicitly clustered.

Statistical Tests

We used custom Matlab scripts to perform nonparametric permutation tests to determine the significance of paired group comparisons, unpaired group comparisons, and pairwise correlations. For very large sample sizes the permutation tests are nearly indistinguishable from standard parametric tests (e.g., the unpaired t-test is comparable to the unpaired group permutation test); however, as sample size is often small ($n<10$), permutation tests provide a more reliable estimate of significance as there are no assumptions about the underlying distribution of data values [46]. All statistical test functions used in this work are provided as a Data Supplement, and are briefly described below.

For unpaired group comparisons (unpaired group permutation test), we calculated the observed difference in means between the two groups, pooled all of the data, and randomly

assigned data points into two shuffled groups. We then calculated the difference in means between the shuffled groups, repeating this step 10000 times. This resulted in a distribution of possible between-group differences in means that could be expected by chance. The fraction of difference values from the random distribution that was greater than the observed mean over the total number of iterations was reported as the p-value for the test. For paired group comparisons (paired group permutation test), paired values from the same subject were never uncoupled during the randomization; otherwise the algorithm was identical to the unpaired test.

The permutation test for correlations involved calculating the observed correlation coefficient ($r_{observed}$) between two array values being compared, then shuffling the values in one array relative to the other and recalculating the shuffled correlation coefficient ($r_{shuffled}$, 1000 to 10000 iterations). This resulted in a distribution of possible correlation coefficients that could be expected by chance. The fraction of $r_{shuffled}$ values with absolute value greater than $r_{observed}$ was reported as a p-value for the permutation test for correlations.

1.4 Results

Recording system demonstration

To demonstrate our recording system's capabilities, we conducted acute recordings with the device in 6 cognitively alert head-fixed mice (one recording session per animal, duration of ~90 minutes). The anatomical placement of each individual silicon prong was verified histologically after every experiment. This allowed us to accurately estimate the location of each recording site in the brain (Fig. 2A). We restricted our single-unit analysis to cells from histologically identifiable regions of interest (orbitofrontal cortex, striatum, GP, and VTA/SN,

hereafter referred to collectively as the recording field). These regions were chosen because of their interconnectivity [43], their involvement in reward-guided actions [47] and because such large-scale recordings have never been carried out in these areas at the same time. We used a semi-automated spike sorting algorithm for high density electrode array recordings to extract putative single unit spiking information (Fig. 2B). Each recording session yielded an average of 315±80 (mean±1 SD; range: 222 to 418) simultaneously measured units across all electrodes on the 3D microprobe. The extracellular spike characteristics of these units were of high quality as measured by their SNR (median=8.4; Fig. 2C), and were broadly separable into two categories corresponding to narrow (mean±1 SD: 0.3±0.1 ms) and wide (0.8±0.2 ms) waveforms (Fig. 2D). This dissociation is consistent with recordings from a heterogeneous population containing broad and narrow spiking cells [48]–[50]. Here we analyzed the dynamics of the combined population. We tested the power of the 3D silicon microprobe device to reveal widespread modulation and correlation of neural activity by rewarding stimuli and cues that predict them (Fig. 2E). The results we present here focus on analytical approaches facilitated by this technology's ability to record at high throughput and large scale.

Mapping neural dynamics at multiple scales

To explore behaviorally modulated network dynamics across the orbitofrontal cortex and basal ganglia, we trained mice to perform olfactory discrimination with a Pavlovian reward conditioning task [51]. Our experimental setup allowed us to deliver external olfactory and reward stimuli, and monitor licking to assess behavioral performance (Fig. 3A). Over several sessions, animals were repeatedly presented with a conditioned stimulus paired with a reward (CS+ trials), and a second neutral stimulus that was delivered without reward (CS- trials). During training mice acquired an anticipatory licking response that was selective to CS+ over

CS- cues, indicating mice had learned to discriminate the two olfactory stimuli (Fig. 3B). Recordings were carried out in well-trained animals following 5 to 7 daily training sessions.

To visualize the task-evoked dynamics of the entire simultaneously recorded ensemble from an individual animal (308 units), we first performed dimensionality reduction using principal component analysis (PCA) on mean stimulus-triggered firing rate (Fig. 3C) [52]. The CS+ and CS- trajectories overlapped during the first second of the trial which corresponded to time during odor presentation. However, shortly after odor offset, CS- activity diverged and returned to its original state. In contrast the CS+ trajectory followed a longer path before its return. This divergence likely reflects the differential neural representation between CS+ and CS- odors, with the longer trajectory of CS+ trials encoding the ensuing anticipatory behavior as well as reward consumption.

To map the spatiotemporal organization of these activity patterns, we first subdivided the mean population firing rate at the level of individual silicon prongs. The mean population activity from all recording sessions qualitatively showed regional and subregional variations in both the evoked response strength and timing to different olfactory cues, as well some marked similarities (Fig. 3D). Next we examined regional population dynamics by visualizing the mean normalized response of individual cells combined from all animals (1,609 units; Fig. 3E). A prominent feature is the appearance of continuously modulated activity patterns that persist longer for CS+ than CS- trials.

In order to examine the spatiotemporal relationship of task modulated activity, we obtained signal correlation coefficients, calculated in correct CS+ trials. We then performed k-means clustering on r_{signal} values from each region separately [53]–[55], and used the resulting parameters to compile a correlation matrix representing the entire recording field (Fig. 3F).

Clusters within each region represented a population of similarly tuned cells (positive r_{signal}).

Intriguingly, the quilt-like pattern of highly correlated clusters across the matrix implies that the

organization of modules of functionally related cells is preserved across different brain

structures, suggesting a substantial amount of similarity in the dynamics of ensembles in

different regions. Overall, the microcircuitry in each region was organized such that closely

spaced cells were more similarly tuned during behavioral response than distally distributed cells

(Fig. 3G), consistent with other studies showing a higher connectivity among local microcircuits

[56]. The visualization of these high-throughput recordings using different analytical approaches

demonstrates the high throughput activity mapping capabilities of the 3D microprobe.

Mapping task-evoked and spontaneous network correlations

The similar tuning properties of many neurons across the recording field suggests specific

cells are predisposed to fire together through common wiring [57]. Such shared connectivity

should influence spontaneously generated synchronous activity, outside of overt behavioral

events [58]–[60]. To examine these intrinsic dynamics, we took advantage of the large scale of

the recordings to calculate pairwise spike count correlations, r_{rest}, coinciding with the animal's

behavioral resting state. Resting intervals corresponded to periods of immobility (no treadmill

rotation and no licking) in the absence of explicitly presented stimuli (Fig. 4A). To examine the

relationship between spontaneous and task-evoked neural activity, we compared resting and

signal correlations, and found a significant correlation between r_{rest} and r_{signal} values. The large

scale of our recordings made this effect evident within an individual animal (r=0.1, p<0.0001,

permutation test for correlations; Fig. 4B), as well as in the combined population from all

animals (r=0.1, p<0.0001 permutation test for correlations; Fig. 4C), implying this is a robust

phenomenon. Moreover, the distribution of r_{rest} values within each region exhibited a distance-

dependent decrease that was qualitatively similar to that for r$_{signal}$ (Fig. 4D). further supporting a link between resting and signal correlations.

We next determined the proportion of statistically significant pairwise correlations in the resting state, which we refer to as the network's functional connectivity (Fig. 4E). We reasoned that since shared synaptic inputs to a subset of neurons is likely to promote a similar activation pattern during the behavioral task, signal correlations should be higher among functionally connected cells. As predicted, cell pairs with significant resting correlations (i.e., functionally connected pairs) had higher r$_{signal}$ values during CS+ trials than uncorrelated pairs ($p=0.03$, paired group permutation test; Fig. 4F), consistent with a network architecture in which cells with overlapping inputs are more likely to display similar task-evoked activity patterns. Together, these results demonstrate our novel recording technology's ability to map correlated activity within and across multiple regions, enabling functional connectivity analysis at a large scale in the mouse brain in vivo. In mammals, this multiregional analysis is usually confined to neuroimaging methods which provide a large-scale view of correlated brain network activity [61], [62] but without cellular resolution. Thus the 3D microprobe technology helps to link together these macroscopic measurements with single-cell studies of brain circuit function.

Mapping state-dependent local field potential coupling

Coherent oscillatory activity is another common hallmark of synchronized neural activity in both cortical [63] and basal ganglia [64], [65] circuits. Since local field potential (LFP) signals are related to the state of local synaptic inputs [66], [67], a coherent signal between spike and LFP activity is thought to indicate an interaction between two recording locations [68]. In order to understand the functional relationship between distally distributed circuits, simultaneous multiregional recordings of unit and LFP activity are necessary. To explore the application of

the recording technology to studying oscillatory interaction patterns, we first characterized the task-evoked fluctuations in spike-LFP coherence between the orbitofrontal cortex and striatum. We found a transient increase in gamma (45-65 Hz) frequency coherence during CS+ trials (Fig. 5A), consistent with the putative involvement of gamma rhythms in coupling distally connected circuits during behavior [69]. To visualize how these oscillatory patterns interact across the recording field, we constructed matrices of the mean change in gamma LFP coherence in discrete time epochs of the behavioral task (Fig. 5B). These high-resolution coherence maps, captured in a single animal and recording session, show substantial heterogeneity in functional circuit coupling at the level of both intra- and inter-regional level, likely reflecting anatomical differences in connectivity and microcircuits that drive gamma oscillations.

We next analyzed spike-LFP coherence in the resting state. Specifically, we examined the corticostriatal spike-triggered average LFP signal to identify any preferred oscillatory modes of synchrony. The cross correlation between the activity of a cortical unit and striatal LFP signal displayed an oscillatory relationship with a period of 300 ms and hence frequency of ~3 Hz, which is consistent with the delta frequency band (Fig. 5C). Furthermore, coupling in the opposite direction (i.e., striatal unit activity and cortical LFP signal) showed a weaker response, demonstrating that interregional synchronization preferentially occurs from the cortex to striatum [70], consistent with corticostriatal wiring. To further elucidate the spectral properties of this oscillatory coupling, we calculated the spike-LFP coherence in the resting state and found that the strongest frequency mode indeed occurred in the delta band (mean±SD: 2.8±0.5 Hz; Fig. 5D). In agreement with a directionally selective coupling from the cortex to striatum, the spike-LFP coherence in the delta band was asymmetric (p<0.0001, unpaired group permutation test). Finally, we mapped resting state delta band coherence across the 3D microprobe (Fig. 5E).

Cortical delta oscillations are frequently reported during periods of quiet wakefulness [71], [72]. Here we found that this rhythm is also highly coherent within the anterior striatum [64], [65], and that delta band coherence is heterogeneously organized across cortical and basal ganglia structures [73]. Together, these maps demonstrate our ability to resolve behavioral state and frequency-dependent variations in oscillatory network coupling with hundreds of simultaneously recorded units and LFP signals.

1.5 Discussion

The 3D microprobe technology presented here uniquely combines several innovative advances in electrode-based sensing: (i) silicon-based probes with submicron minimum feature size leading to narrower structures than other microfabricated devices with a comparable number of electrodes, (ii) multiplexed readout of electrical signals to reduce external wire bundle sizes 15-fold relative to standard readout methods, and (iii) compact three-dimensional assembly, to provide precise, reproducible, and easily customizable anatomical targeting of multiple separate regions of the mouse brain. Leveraging the substantial gains in device miniaturization and scalability in the number of electrodes that these improvements provide, we carried out simultaneous in vivo measurements with 1,024 electrodes, the largest number reported so far in any rodent experiment. This improvement is of particular benefit for mouse studies where electrode-based tools require the highest degree of miniaturization. These methods are further expandable to thousands of electrodes for the mouse brain, and by extrapolation, potentially tens of thousands of electrodes for larger rodent and primate brain activity mapping in any 3D configuration.

Components of this technology are broadly accessible thanks to a number of commercially available services. Planar silicon probes were fabricated entirely at a MEMS foundry specializing in silicon etching and patterning of metals and insulators with submicron resolution. The production process yields hundreds of assorted functional probes per wafer batch with 64, 128, and 256 electrodes, lowering the effective cost per device. Other recording system components are available from third-party manufacturers at relatively low cost to build a complete 1,024 electrode probe. Moreover, an advantage of recording acutely in head-fixed animals is that the device is indefinitely reusable, thereby reducing assembly time and expense. All electronic components comprising the head stage are available commercially, and as a consequence of newly available multiplexed amplifier systems and open-source approaches in electrophysiology [74], the cost of measuring signals from thousands of electronic channels has also dropped dramatically in the past few years. Finally, with parallel advances in surgical automation for making craniotomies [75], the preparation time prior to carrying out recordings in mice could be further reduced, and the recording procedures themselves eventually automated.

The assembly of 3D structures has been greatly simplified with our multilayer stacking and alignment method, which, unlike previous approaches involving mechanical scaffolds [76], does not require any customized components to create a specific configuration, thus can be rapidly adapted to changing experimental needs. A set of wide and narrow PCBs allowed us to space consecutive PCB layers by as little as 0.8 mm, with a further reduction to ~0.4 mm possible using thinner PCBs. In principle, the multilayer assembly approach can be expanded to more than four layers and is ultimately only limited by available space. The probe assembly system is built with standard optomechanical parts, motorized micromanipulators, and inexpensive machined components. A potential limitation of this assembly method is that layers

targeting individual regions are rigidly bonded together and their depth cannot be independently adjusted. On the other hand, the millimeter-scale span of the electrode array on the silicon prongs helps compensate for small targeting errors, increasing the likelihood that at least some electrodes will reach the area of interest.

The advantage of monitoring neural activity across multiple scales is evident by our recordings in the mouse orbitofrontal cortex and several basal ganglia nuclei, which revealed information regarding the multiregional organization of circuit dynamics during periods of behavioral responding and rest. The dynamics contained some marked similarities at the inter-regional level as seen by their response to cues. We also showed that local circuits preferentially perform specialized computations, as seen by subregional variations in activity and spatially decaying correlations. Furthermore, we identified a significant correlation between signal and resting state correlations, similar to phenomena found in human fMRI measurements at a larger albeit coarser scale [77]. Similar relationships between noise and signal correlations have been found in previous electrophysiological studies [56], [78], but at a smaller scale and with a lower throughput than demonstrated by our 3D microprobe. The high throughput of these recordings can greatly accelerate experimentation by enabling functional screening of multiple distal brain areas in parallel and thereby reduce animal usage. We simultaneously recorded hundreds of units in an individual session, and compiled data from over 1,600 units in just 6 sessions. A pitfall of conducting these measurements in head-fixed mice is that they are limited to a single recording session per animal. Thus, studying neural activity as animals learn complex behavioral tasks may require several independent cohorts of animals representing different stages of training. Alternatively, studies could rely on relatively simple tasks that can be acquired within one training session [79].

This recording technology opens up new possibilities for using mouse models to understand how neurological and psychiatric disorders alter systems-level brain functions [80]. For instance, recording across the basal ganglia could reveal abnormal feedback loop dynamics in addiction or movement disorders. Neuroscience has only recently begun to access the large-scale multiregional regime of brain activity with cellular resolution [33], [37], [81], and the recording capabilities of 3D silicon microprobes offer unique opportunities for mapping network dynamics in the mouse.

Author Contributions

J.L.S., L.D.C., K.I.B., and S.C.M. conceived the experiments, analyzed data, and wrote the manuscript. J.L.S. also carried out surgical procedures, behavioral testing, electrophysiological

recordings, histological analysis, and analyzed task-evoked network dynamics. L.D.C. also

assembled the 3D microprobe, developed the 1,024 channel data acquisition system, assisted

with electrophysiological recordings, and analyzed network correlations. K.I.B. wrote code for

unit activity analysis. S.P. wrote code for k-means clustering of the signal correlation matrix.

Disclosures

The authors declare the absence of any conflict of interest.

1.6 Figures
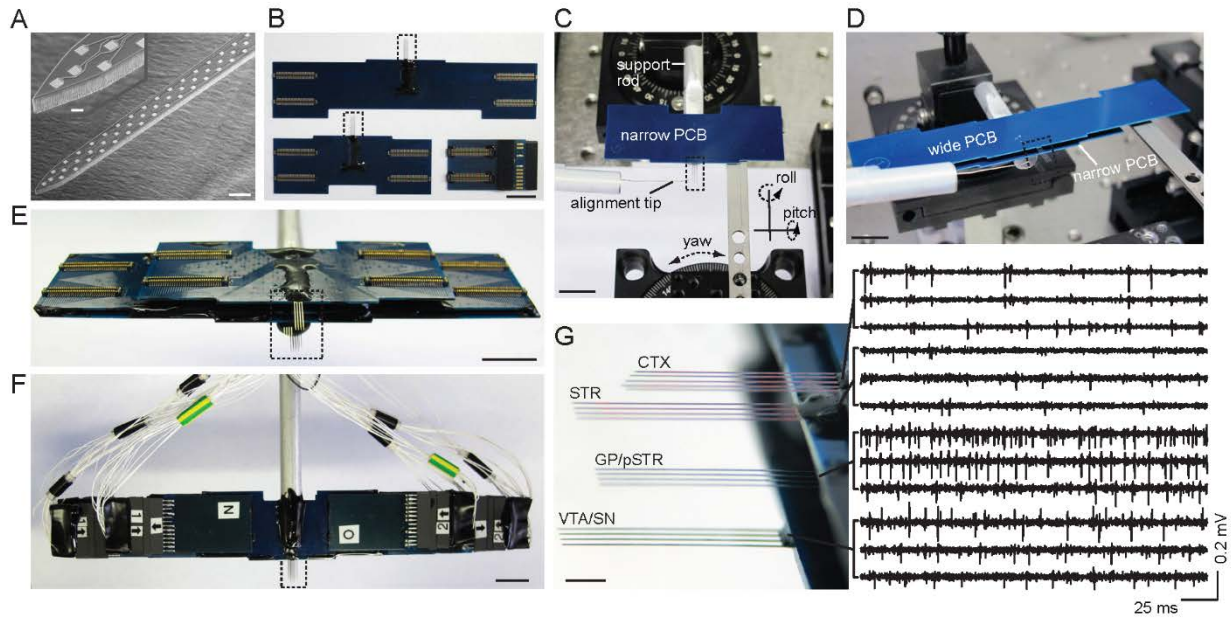
Figure 1: 3D silicon microprobe development.

A. Scanning electron micrograph of a microfabricated silicon prong containing a high density 64 electrode array. The electrode array spans 1 mm from end to end. Scale bar represents 50 μm. Inset shows a higher magnification view of the tip (10 μm scale bar).

B. Wide-winged (top) and narrow (bottom left) PCBs used to create a stacked multilayer 3D microprobe. Each PCB is attached to a multipronged 256 electrode silicon probe (boxed areas). Bottom right: One of eight 128 channel head stages used to read out electrophysiological signals. Scale bars in B-F represent 10 mm.

C. Alignment of the first layer consisting of a narrow PCB to an aluminum support rod. The alignment tip is used to orient the silicon prongs parallel to the insertion axis.

D. Alignment of the second layer consisting of a wide PCB to the underlying narrow PCB.

E. Fully assembled 1,024 electrode 3D microprobe combining 2 narrow and 2 wide-winged PCB layers each containing a 256 electrodes array.

F. Fully connected ready-to-use 3D microprobe with 1,024 electrodes. The 3D microprobe is imaged with all head stages and wires attached, in preparation for recording. Note the significant reduction in external wires relative to the number of electrodes due to multiplexing circuitry on the head stages. There are a total of 8 head stages, with half not visible as they plugged into the bottom side of the structure.

G. Left: High magnification view of the boxed area in (E) showing the exact 3D configuration. Right: representative bandpass filtered signals (600-6500 Hz) from three electrode recording sites in each layer. Scale bar represents 2 mm.
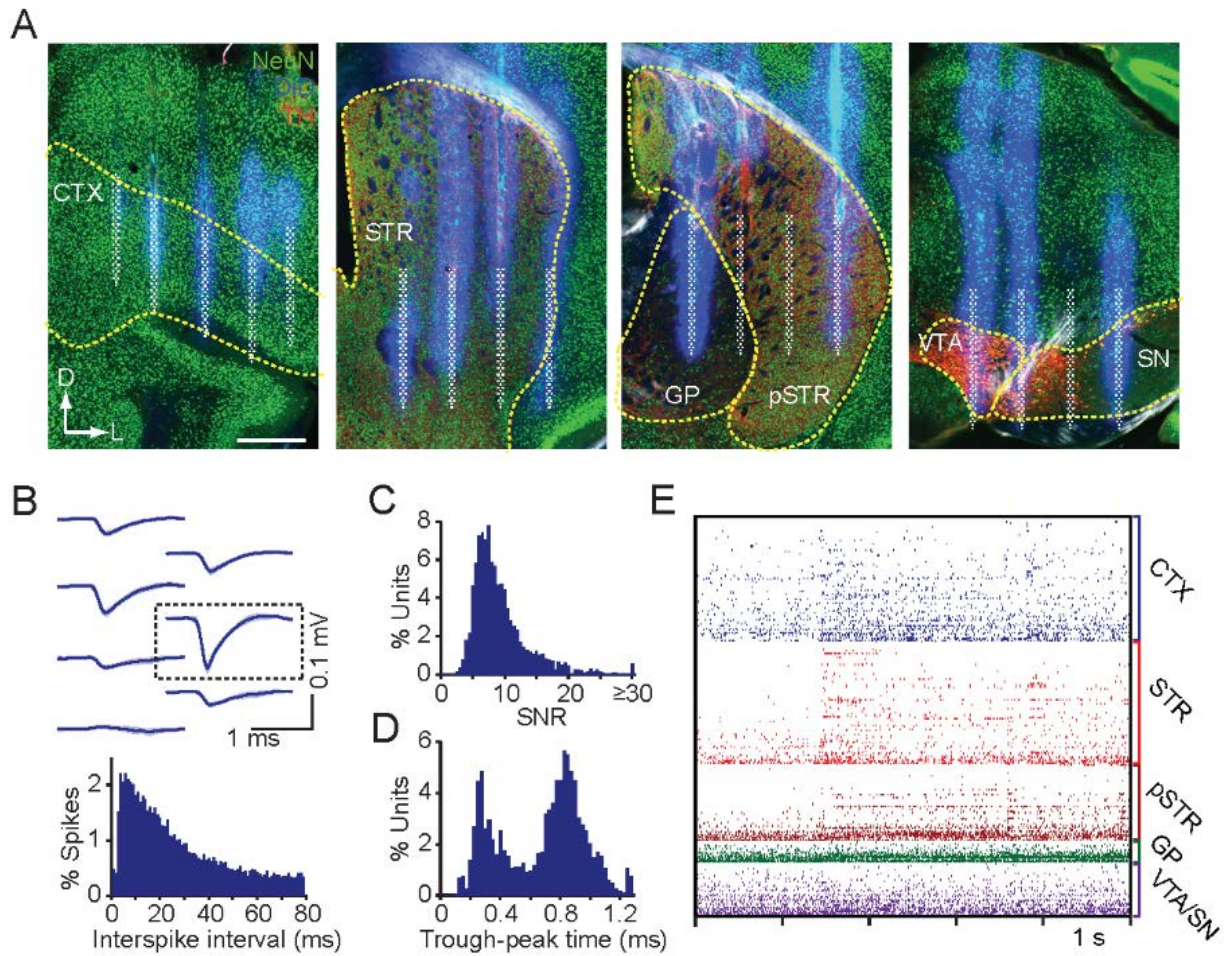
Figure 2: Histology and single-unit characteristics.

A. Confocal microscope images of the coronal brain sections from four simultaneously targeted areas. The DiD fluorescence signals indicate the silicon prong insertion sites, from which the electrode positions were reconstructed. The approximate location of the electrode arrays are superimposed in white. Sections are co-labeled with antibodies against NeuN and tyrosine hydroxylase. Dashed lines indicate boundaries of the regions of interest. Scale bar represents 0.5 mm.

B. Top: Representative mean spike waveform of a putative cortical unit on a local cluster of electrodes. The boxed area corresponds to the electrode where the unit is approximately located. Bottom: Interspike interval distribution for the above unit.

C. Signal-to-noise (SNR) distribution of all putative single-units from 6 recording sessions.

D. Bimodal spike width (trough-to-peak time) distribution of all putative single-units.

E. Activity raster of 308 (95 orbitofrontal, 155 striatal, 17 pallidal, and 41 VTA/SN) simultaneously recorded units from 1 animal during an olfactory stimulus presentation.
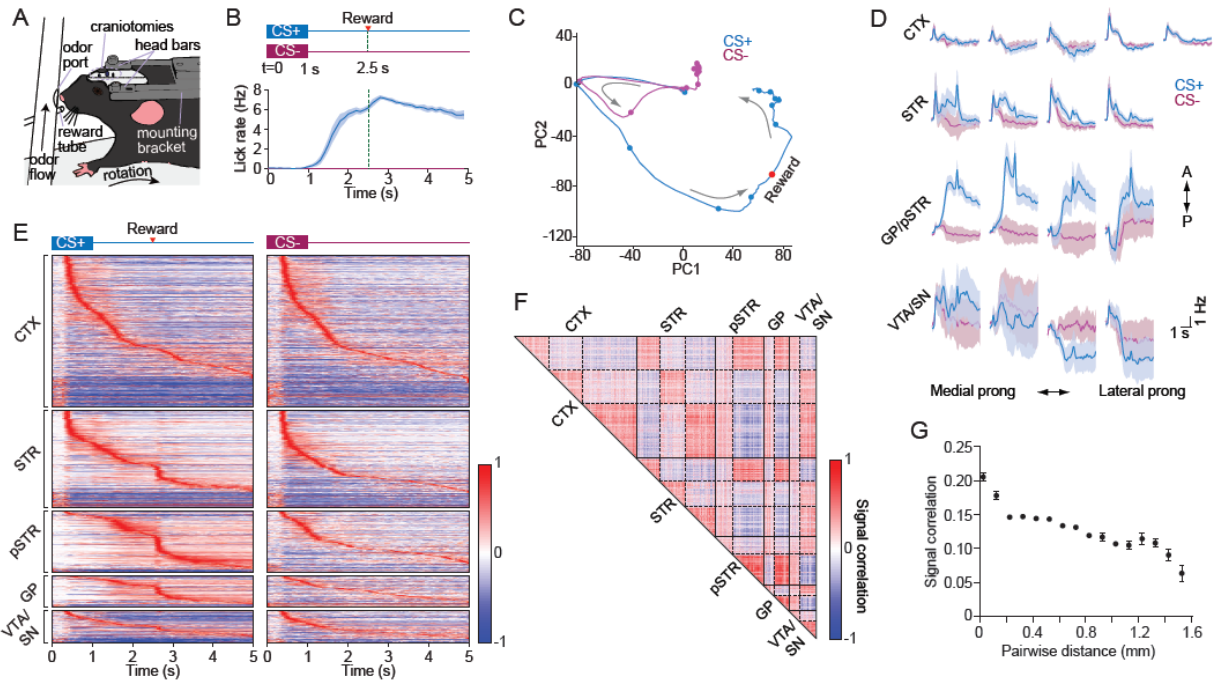
Figure 3: Mapping of network dynamics at multiple scales.

A. Behavioral testing and recording setup for a head fixed mouse mounted on top of a spherical treadmill.

B. Top: Reward conditioning scheme showing the two types of stimulus conditions: CS+ odor (1 s duration) paired with a reward at 2.5 s, and unpaired CS- odor (1 s duration). Bottom: Mean lick rate of all animals triggered on correct CS+ (anticipatory licking) and CS- (withheld licking) trials. Dashed green line represents time of reward delivery for CS+ trials. Shading represents ±SEM.

C. PCA trajectory of the mean activity of 308 simultaneously recorded units from 1 animal under different stimulus conditions. The trajectories start near the origin. Black dots denote 500 ms time intervals. The red dot indicates the reward delivery time. Arrows indicate the trajectory direction.

33

D. Mean change in population firing rate of units recorded on the 17 silicon prongs comprising the 3D microprobe. Activity is plotted from t=0 to t=5 s post stimulus onset. Data represent combined recordings from 6 animals. Shading represents ±SEM.

E. Mean evoked activity of units in different regions triggered on correct CS+ (left) and CS- (right) trials. Data represent 1,609 units combined from 6 animals. Activity is plotted as the normalized difference in firing rate relative to a baseline period prior to cue onset. Units are ordered according to their latency to peak firing separately within each region and stimulus condition.

F. Signal correlation matrix for mean task-evoked activity during CS+ trials. Data correspond to the units displayed in (e) combined from 6 animals. Matrix elements were arranged by independent k-means clustering in each of the anatomical areas indicated. Three clusters were assigned to the cortex and striatum, and the other areas were assigned two clusters. Solid lines demarcate the brain areas where k-means clustering took place separately. Dashed lines indicate the cluster boundaries within each area.

G. Mean signal correlation versus pairwise distance between units located in the same brain region (CTX, STR, pSTR, GP, or VTA/SN). Data are combined from all simultaneously recorded cell pairs in 6 animals. Points denote mean±SEM binned in increments of 0.1 mm.
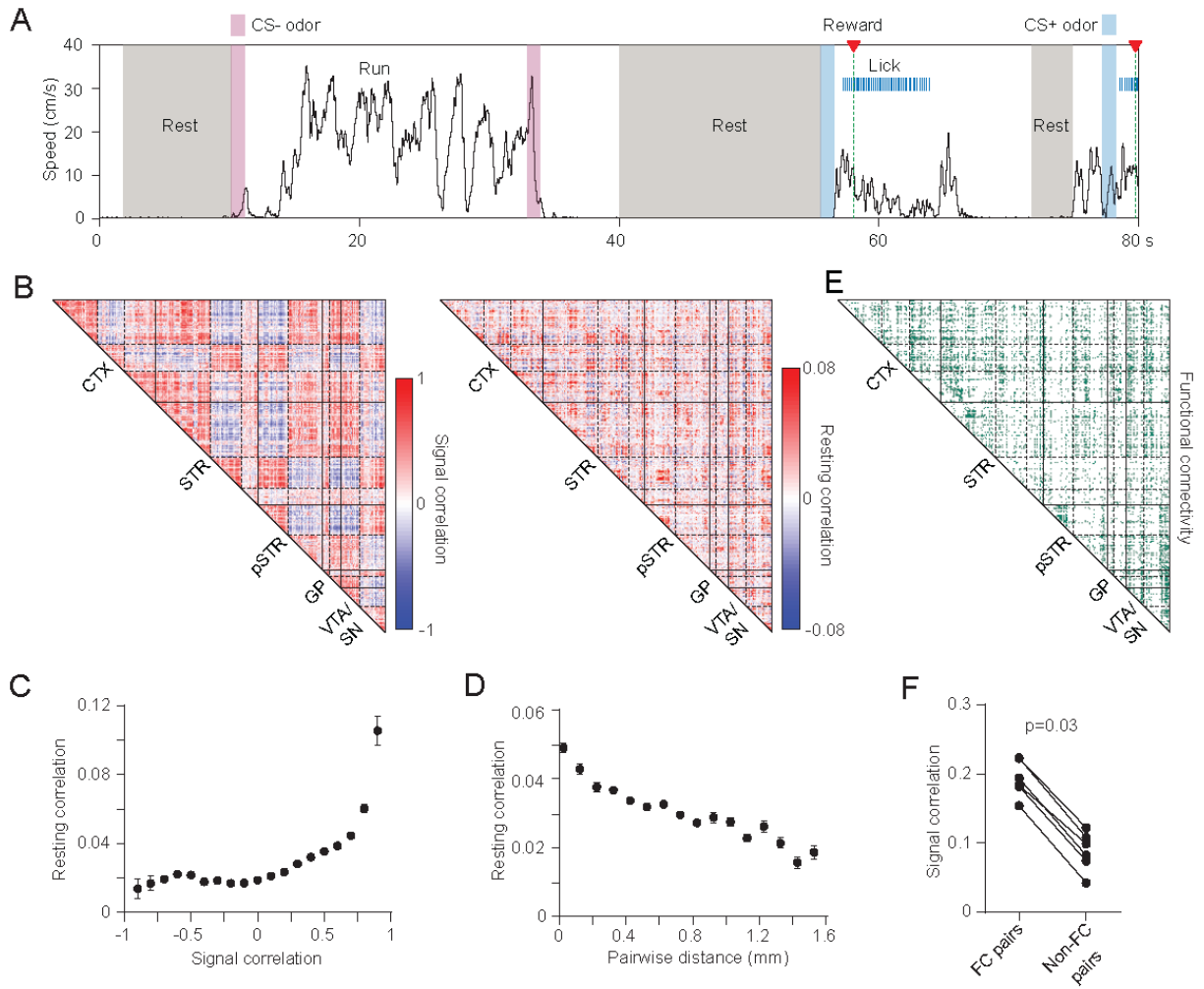
Figure 4: Large-scale analysis of network correlations.

A. Example of resting state intervals corresponding to idle periods during behavioral testing.

B. Left: Signal correlation (r_{signal}) matrix for mean task-evoked activity during CS+ trials. Data represent simultaneously recorded units from 1 animal. Matrix elements were arranged by independent k-means clustering in each of the anatomical areas indicated. Three clusters were assigned to the cortex and striatum, and the other areas were assigned two clusters. Solid lines demarcate the brain areas where k-means clustering took place separately. Dashed lines indicate the cluster boundaries within each area. Right: Resting correlation

35

(r_{rest}) matrix using the cell ordering identified from k-means clustering of the signal correlations. The matrices are correlated (r=0.1, p<0.0001, permutation test for correlations).

C. Mean resting state correlation coefficient as a function of signal correlation during correct CS+ trials. Individual r_{rest} and r_{signal} values are correlated (r=0.1, p<0.0001, permutation test for correlations). Data are combined from all simultaneously recorded cell pairs in 6 animals. Points denote binned mean±SEM.

D. Mean resting state correlation coefficient as a function of pairwise distance between units located in the same brain region. Data are combined from all simultaneously recorded cell pairs in 6 animals. Points denote mean±SEM binned in increments of 0.1 mm.

E. Matrix identifying pairs of simultaneously recorded cells with a significant resting state correlation, considered a functional connection. The cell ordering was identified from k-means clustering of the corresponding signal correlations in (B).

F. The signal correlation during correct CS+ trials is higher between functionally connected (FC) cells. Points denote the mean signal correlation coefficient between all functionally connected or unconnected pairs per animal.
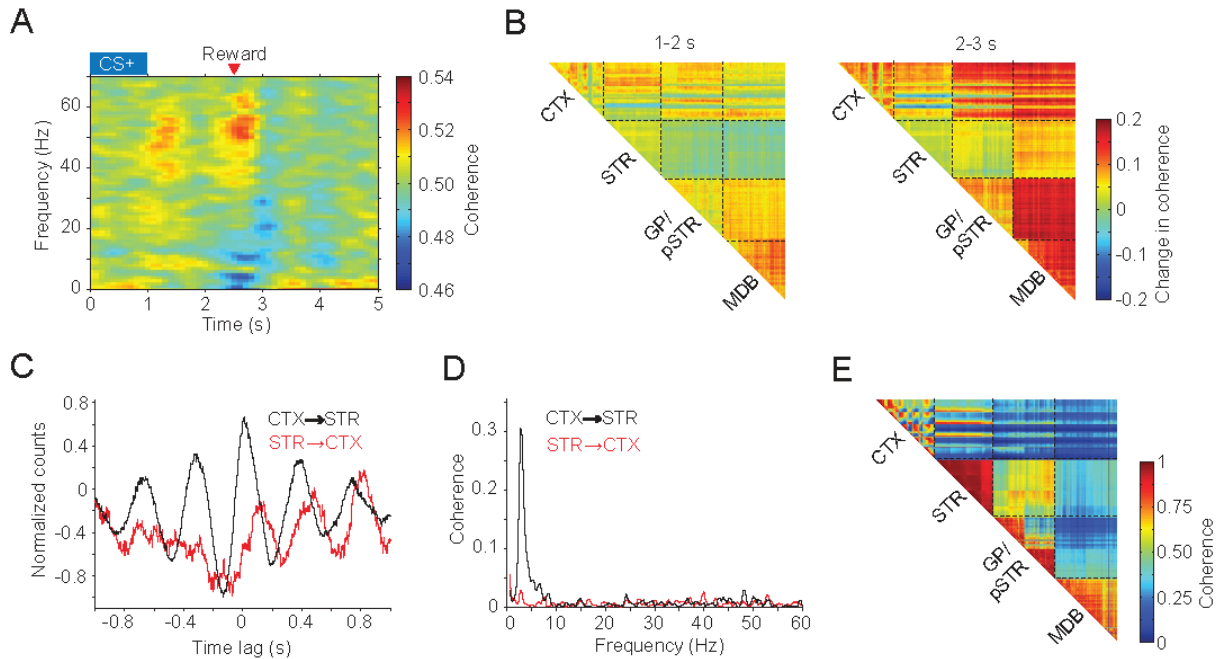
Figure 5: Mapping of local field potential activity.

A. Mean corticostriatal spike-LFP coherence spectrogram during correct CS+ trials. Data represent 1 animal.

B. Two time-lapse matrices of mean 45-65 Hz LFP coherence stepped in 1 s intervals during correct CS+ trials. Coherence values are measured relative to a baseline period 1 s before the cue onset. Data represent simultaneous recordings from 1 animal. Dashed lines indicate the boundary between different layers in the 3D microprobe each containing 256 electrodes. MDB represents the midbrain, which includes the VTA/SN nuclei.

C. Spike-LFP cross correlogram (CCG) during spontaneous resting state activity. Black line denotes the CCG between spikes of one unit in the orbitofrontal cortex and LFP from one electrode in the striatum. Red line denotes the CCG with the spikes and LFP selected from the opposite locations.

D. Spike-LFP coherence spectrum of the data used to calculate the results in (C).

E. Matrix of 2-4 Hz LFP coherence in the resting state across the four separate sections targeted by the 1,024 electrode microprobe. MDB: midbrain, which includes the VTA, SN, and other nearby midbrain nuclei. Data represent simultaneous recordings from 1 animal.

CHAPTER 2

Direct and indirect pathway neural dynamics during Pavlovian conditioning

2.1 Introduction

Movement disorders affect many people and have a wide range of symptoms and severity, but while decent therapies exist for some disorders, there is much room for improvement. The basal ganglia (BG), a network of subcortical nuclei with complex interconnectivity, is a target for many studies of movement disorders and their respective therapies. Movement disorders that are thought to arise due to abnormalities in the BG can have distinct and seemingly opposing symptoms. For instance, Parkinson's disease causes hypokinetic motor impairments in patients, whereas Huntington's disease gives rise to hyperkinetic symptoms [5]. In addition, there are disorders such as Dystonia and Tourette syndrome that are characterized by involuntary repetition of stereotyped movements [82]. Research into these disorders typically targets the main input hub for afferents into the BG called the striatum. Studies performed in the 1980s revealed evidence of two distinct pathways that project from the striatum to the BG output nucleus, the substantia nigra pars reticulata (SNr). The "direct" pathway referred to an inhibitory projection from the striatum to the SNr and the "indirect" pathway referred to an overall excitatory projection from the striatum to the SNr through the external segment of the globus pallidus (GPe) and the subthalamic nucleus (STN) [6]. It was proposed by Alexander and Crutcher that the pathways likely had opposing effects on the BG output and the thalamic targets as well. Another perspective published at the same time suggested that shifts in the balance between direct and indirect pathways could account for the opposing effects of hypo- and hyperkinetic symptoms of the BG-related disorders [7].

The striatum is a unique and complex structure, and is largely an inhibitory microcircuit. The principal projection cell of the striatum, the medium spiny neuron (MSN) - also referred to as the spiny projection neuron (SPN) - receives excitatory, glutamatergic input from the cortex

and sends inhibitory signals in the form of GABAergic efferents to the targets of the direct and indirect pathway. About 95% of the neurons in the striatum are MSNs [83] and they are classically divided into direct and indirect pathway MSNs based on their projections. Another distinguishing feature between the two subpopulations is their expression of dopamine receptors, as the striatum receives dense dopaminergic innervation from the ventral tegmental area and the substantia nigra pars compacta [5], [18], [84]. Gerfen and colleagues showed that MSNs of the direct pathway mainly express D1 dopamine receptors and are positively modulated by dopamine, whereas MSNs of the indirect pathway express D2 dopamine receptors and are negatively modulated by dopamine [26]. Continued research has shown deviation from perfect segregation, as some MSNs express both types of dopamine receptors, but the reported numbers are low ($< 5\%$ of MSNs outside of the nucleus accumbens, [85], [86]). For the remainder of this chapter, D1 will refer to cells in the direct pathway that express D1 dopamine receptors, and D2 will refer to cells in the indirect pathway that express D2 dopamine receptors.

In addition to being the main projection cells in the striatum, MSNs also send dense lateral GABAergic projections to other MSNs. Recent studies have focused on how lateral MSN signaling functions in concert with direct and indirect pathway signaling to influence motor and motivated behaviors, as well as learning. Classical models of BG function describe the direct and indirect pathways as "go/no-go" pathways, respectively, and suggest that they act antagonistically to promote and inhibit movement [2], [5], [7]. A study by Kravitz et al. showed that optogenetic excitation of the D2 MSNs elicited a parkinsonian state in mice, and excitation of the D1 MSNs reduced symptoms and increased locomotion in a mouse model of Parkinson's [9]. However, other studies propose that coordinated activity between both pathways is necessary for performing motor behaviors [10], [11]. Jin and colleagues performed extracellular

recordings of D1 and D2 MSNs as well as neurons in the GPe and SNr, and showed that

different subsets of neurons in both pathways were activated during action sequence initiation,

execution, and termination [13].

In order to better understand direct and indirect pathway function in motivated behaviors,

we studied single unit activity of D1- and D2-receptor expressing cells in the lateral striatum in

mice performing a conditioned response during a Pavlovian association task. This work details

the optimization of an optogenetic photo-tagging protocol for use with silicon-based

microelectrode arrays, with discussion of special considerations allowed when performing

optogenetic tagging in the striatal microcircuit. Additionally, the study presents the relationship

between D1 and D2 population dynamics during a motivated or conditioned response.

2.2 Methods

Surgical procedures

All procedures were approved by the University of California, Los Angeles Chancellor's

Animal Research Committee. Singly housed male and female D1-cre and A2a-cre mice (n = 9

D1 and n = 8 A2a, 12-20 weeks old) were used in the experiments. Animals underwent a

surgical procedure under isoflurane anesthesia and aseptic conditions in a stereotaxic apparatus.

The procedure entailed attachment of stainless steel head restraint bars to the skull (10 mm x 7.5

mm, 0.6 g, laser cut at Fab2Order) and infusion of an adeno-associated virus (AAV, University

of North Carolina Vector Core). A volume of 750 nL of AAV5/Svn-Flex-Chrimson R-tdTomato

was injected unilaterally using glass micropipettes (Nanoject II, Drummond Scientific) into the

lateral striatum at a rate of 50 nL/minute. Injection coordinates targeting the striatum were 1.0

mm anterior, 2.1 mm lateral, and 3.4 mm ventral to bregma, experiments were counterbalanced

by randomizing which hemisphere was injected. Mice received a carprofen injection (5 mg/kg, s.c.) on the day of the surgical procedure and daily injections for the subsequent two days. Mice were also given ibuprofen and amoxicillin in their drinking water for a week following surgery. After mice were trained on the behavioral task, a second aseptic surgical procedure was performed to make a rectangular craniotomy and remove the dura above the injected striatum to allow for placement of the recording device. In addition, a small craniotomy was made above the posterior cerebellum for placement of a silver/silver-chloride reference wire. Mice were given a carprofen injection during this surgery as well.

Behavioral task

After one week of recovery from the surgery, animals were single-housed, food restricted, and fed daily after each training session to maintain ~90% of their baseline weight. They received water ad libitum. During daily training sessions, animals were mounted with the head bar bracket on a behavioral testing rig and on top of a fixed spherical treadmill (200 mm diameter, Graham Sweet Studios). A reward solution (5 μL, 10% sweetened condensed milk) was dispensed from a tube positioned between an infrared beam lick meter (Island Motion), and its delivery was signaled by an audible solenoid valve actuation (Neptune Research 161T010). Initially, animals were habituated to head fixation and trained to consume the reward. During the habituation phase mice learned to associate the solenoid actuation sound with a reward, and after consuming at least 90% delivered rewards for two consecutive days, they began Pavlovian conditioning with olfactory cues. Odorants were introduced via an olfactometer by bubbling air (0.15 L/min) through aromatic liquids diluted 1:10 in mineral oil (Sigma-Aldrich), and mixing this product with the 1.5 L/min main stream of air. The odor used for the cue was amyl acetate (banana). The odor was presented for 1 s, followed by a delay of 2

43

s, then delivery of 5 µL of the reward solution (18-30 s ITI, 100 rewarded trials per day). During training mice started to lick in anticipation of the reward (in the interval between odor onset and reward; 0-3 s). Mice experienced three to five days of Pavlovian training prior to the second surgical procedure and subsequent recording session.

Electrophysiology with optogenetic stimulation

Mice were given 12-24 hours to recover from the second surgical procedure before being placed on the behavioral testing rig for electrophysiological recording. The lateral striatum was targeted with a 256 electrode silicon microprobe comprised of 4 prongs spaced 200 µm apart, with 64 electrodes each [1]. The target coordinates of the most lateral prong in striatum were: 1.0 mm anterior, 2.4 mm lateral, 4.0 mm ventral to bregma. In order to genetically identify D1 or D2 cells optogenetic stimulation was performed using a pair of optical fibers (200 µm diameter, 0.22 NA) connected to the silicon microprobe with their centers spaced 400 µm apart (this integrated device is referred as an opto-microprobe) [16]. The optical fibers were coupled to a laser (589 nm, Changchun New Industries Optoelectronics; or 532 nm, Opto Engine). Coupling was carried out via a 50/50 optical splitter (Thorlabs) and power output was calibrated before each experiment.

During the electrophysiological recording, mice were presented with 100 to 150 cue and reward trials. Following completion of the behavior portion of the recording, the tissue surrounding the opto-microprobe was stimulated with 50 laser pulses (100 ms continuous pulse) at three laser powers (1, 5, and 10 mW), for a total of 150 laser pulses per animal (5 s inter-pulse interval).

A subset of the mice (n = 1 D1-cre and n = 6 A2a-cre mice) underwent a second craniotomy surgery and a second electrophysiological recording in the lateral striatum that had

no viral injection. During these recordings mice received only the laser stimulation protocol. The data gathered during these recordings served as a control for genetic identification of neurons based on optogenetic stimulation, since there were no cells expressing the opsin in the control hemisphere.

Data analysis and optogenetic tagging criteria

Spike sorting and all neural activity analysis was carried out with custom Matlab scripts. Striatal units were identified using previously described electrophysiological criteria based on spike waveform duration [16], [25]. Firing rate was calculated by convolving spike times with a Gaussian filter (SD = 25 ms) in time steps of 5 ms.

The test for determining whether a unit was significantly activated or "tagged" by the 100 ms laser pulses was based off of a test devised by Kvitsiani and colleagues called the Stimulus-Associated spike Latency Test (SALT) [27]. SALT is a statistical test that measures whether optogenetic activation changes a cell's spike timing with respect to the light stimulus. It looks at windows of time associated with baseline firing (when no outside stimulus has been presented) and windows that coincide with the onset of the laser stimulus. A histogram of the latencies to the first spike within the window is created for many baseline-associated windows and the laser-associated windows. The distances between the latency distributions are calculated using a modified Jensen-Shannon divergence measure. Using this metric, SALT tests the hypothesis that the laser-associated distribution is different from the baseline distributions and gives each unit a p-value. We ran the SALT test with a window size of 30 ms and "tagged" units that had p < 0.01. One final criterion we used was the baseline spike waveform had to be similar to the laser-induced spike waveform. We calculated the Pearson's correlation coefficient, r, of the mean baseline spike waveform and the mean first laser-induced spike waveform. Units with a SALT p

< 0.01 and a waveform correlation r > 0.85 were labeled as "tagged" and used in subsequent analyses as a D1 cell if it was from a D1-cre mouse and a D2 cell if it was from an A2a-cre mouse.

Histology and optical fiber position determination

Following the completion of the electrophysiology experiment, the brain was coronally sectioned at 100 μm on a vibrating blade microtome (VT1000E, Leica) and individual sections were placed in order into a 24-well plate containing phosphate-buffered saline (PBS). We then imaged the slices using a confocal microscope to confirm opsin expression and correct placement of the opto-microprobe in the striatum. Only mice with equivalent levels of expression and correct positioning of the probe within the region of expression were included in the analysis.

Statistical Tests

All statistical analyses were performed using standard Matlab functions and Prism software. Information about the exact value of n, what n represents, statistical test used, and p-value is provided in the main text and/or figure captions. All plotted data represent mean ± SEM. In the figure legends, **** denotes $p < 0.0001$, ** $p < 0.01$, and * $p < 0.05$.

2.3 Results

Genetically identifying cell types using an optogenetic photo-tagging protocol

The BG are a well-known target for research concerning movement disorders, such as Parkinson's disease, Huntington's disease, dystonia, etc. The BG are known to be an integral part of the circuit involved in motor control. The circuit goes as follows: sensorimotor cortical regions send afferents to the striatum, which functions as the input hub of the BG; striatum

projects through the rest of the BG and influences neural activity in the thalamus; the thalamus then sends signals back to the cortex and to the brainstem to control motor actions, thus completing the motor loop [5]. In the late 1980s, studies of the BG circuitry revealed two distinct pathways from the striatum to the output nucleus, SNr [6]. An inhibitory projection from the striatum straight to the SNr was described as the "direct" pathway. While a more circuitous pathway, termed the "indirect" pathway, consisted of an inhibitory projection from the striatum to the GPe, an inhibitory projection from the GPe to the STN, and finally an excitatory projection from the STN to the SNr (Figure 1A). It was also proposed that, due to the inhibitory and excitatory nature of each segment, the direct pathway likely facilitated movement and the indirect pathway inhibited it [2], [5], [7]. Using optogenetic manipulations of the direct pathway via D1 dopamine receptor-expressing medium spiny neurons (D1 MSNs), studies have shown that activation of the D1 MSNs alleviate hypokinetic movement symptoms in a parkinsonian mouse model [9]. Kravitz et al. also showed activation of the indirect pathway via D2 dopamine receptor-expressing MSNs (D2 MSNs) causes freezing and reduces initiation of locomotion.

MSNs are the principal cell type in the striatum, comprising 95% of the total cell count [83]. They send inhibitory projections to the targets of the direct and indirect pathways and they exert collateral GABAergic control over each other. Though there are equal numbers of D1 and D2 MSNs and both subpopulations synapse onto both types, there is evidence that D2 MSNs are more connected to the D1s and D2s than are D1 MSNs [87], [88]. The other 5% of cells in the striatum are various interneurons (Figure 1B-C): the fast-spiking interneurons (FSIs) exert strong GABAergic inhibition over large populations of D1 and D2 MSNs [88]–[90]; and the tonically active neurons (TANs) release acetylcholine and extend wide lateral excitatory projections to many MSNs [91]. This work focuses on the neural dynamics of the D1 and D2 cells because

47

they are the only projection neurons of the striatum, and they are presumed to represent activity in the direct and indirect pathways, respectively [26].

Recent studies have proposed an alternative to the seminal "go/no-go" model of BG function. This more nuanced model suggests that coordinated activity from both pathways is necessary for animals to perform motor behaviors [10]–[12]. Evidence supporting the model can be found in extracellular recordings of D1 and D2 MSNs that showed that both types were activated during action sequence initiation, execution, and termination [13]. In order to study the direct and indirect pathways in the context of a simple, motivated behavior, we measured neural activity of genetically identified D1 and D2 cells while mice performed a Pavlovian association task. We expressed light-activated ion channels in D1 or D2 cells by injecting an adeno-associated virus expressing ChrimsonR [92] in a Cre-dependent manner into the lateral striatum of mice expressing Cre recombinase in D1 dopamine or A2a receptor-expressing cells, respectively (n = 9 D1-cre and 8 A2a-cre mice, Figure 1D). We used an opto-microprobe (Figure 1E) to record single unit activity during a behavioral task where an odor cue presented for 1 s was paired with a sweetened condensed milk reward after a 3 s delay (100 to 150 trials) followed by light stimulation (150 continuous laser pulses, 100 ms duration, Figure 1F). We recorded activity from greater than 50 well-isolated single units per animal. Single units had a wide variety of activation patterns both to the behavioral task and the light stimulation (Figure 2).

Currently, there are many methods used to identify cells that are activated by laser stimulation. The most common criteria are thresholds on the level of laser-associated activation and the latency to fire [13], [93], [94]. These methods require either using *in vitro* methods to determine appropriate thresholds for activation and latency or existence of a bimodal distribution

in the data set. We wanted to use an identification method that did not rely upon the setting of potentially arbitrary thresholds. We chose to use the Stimulus-Associated spike Latency Test (SALT) developed by Kvitsiani et al. that tests the null hypothesis that a neuron's spike timing is not altered by laser stimulation [27]. It analyzes the latency to first spike in windows that are associated with baseline spiking (spiking that is not associated with any outside stimulus, laser or otherwise) and windows associated with laser-associated spiking. The distances between baseline- and laser-associated latency distributions are calculated using a modified Jensen-Shannon divergence measure. For each cell, the distance between baseline and laser-associated distributions for a cell is compared to a null distribution of the baseline distances and a p-value is assigned to the cell (Figure 3). We implemented SALT using a window size of 30 ms and accepted cells as tagged if $p < 0.01$. In addition to SALT, we tested the similarity between the baseline spike waveform and the light-induced spike waveform using the Pearson's correlation coefficient, r (Figure 4). All units that had a SALT p-value < 0.01 and a high spike waveform correlation, $r > 0.85$, were identified as "tagged" and included in further analysis.

We performed extracellular recordings in eight D1-cre mice (n = 87 positively identified D1 cells, Figure 5A) and in nine A2a-cre mice (n = 74 positively identified D2 cells, Figure 5B). To control for any effects of the laser not related to the light activating the opsin, we performed recordings in some mice (n = 1 D1-cre and 6 A2a-cre mice) by inserting the opto-microprobe into the lateral striatum that did not receive the viral infusion, and thus did not have cells expressing ChrimsonR. Using the same SALT and waveform criteria, we tagged only 11 cells (Figure 5C) meaning that our false-positive identification rate is low.

Because we used SALT to identify tagged cells based on their spike latency, we wanted to check whether the positively identified D1 and D2 cells increased their firing rates during the

laser stimulation. We used a measure that relates the firing rate during the 100 ms laser pulse to the distribution of baseline firing rates, called the z-score. Both D1 and D2 cells significantly increased their firing above baseline compared to untagged cells from the respective recordings during laser stimulation (unpaired t test, D1-cre: $p < 0.0001$, A2a-cre: $p < 0.0001$; Figure 5D). We stimulated with different laser powers in order to determine the appropriate stimulation parameters for identifying cells. D1 and D2 cells, however, were maximally activated even at the lowest power setting we used (1 mW per fiber, measured 1 mm from the tip of the optical fibers). The D1 and D2 populations did not have significantly different baseline firing rates or standard deviations of the baseline rate (Figure 5E-F).

D1 and D2 populations co-activated during Pavlovian task

We first examined neural activity during the Pavlovian task by averaging the neuron's firing rate across all correct trials (trials where the mouse initiated licking prior to reward delivery, 0-3 s) aligned to the time of cue onset. There appears to be a number of D1 cells that are activated above baseline during the delay between the cue and reward when mice are initiating licking behavior and at the time of reward delivery (Figure 6A). A similar response of a lesser magnitude is seen in the D2 cells (Figure 6B). By process of elimination, the neural activity of untagged cells in Figure 6C likely reflects a large number of D2 cells and any D1 cells that either were not light-activated enough to be tagged or did not express ChrimsonR. The opposite is true for Figure 6D (more D1 cells than D2), which displays a larger proportion of cells activated during cue, delay, and reward time, similar to the tagged D1 cells. The average tagged D1 population activity is similar to the untagged population activity, but with more elevated firing during the delay and after reward delivery (Figure 6E). There is not much difference between the average population activity of tagged D2 cells compared to untagged

50

cells (Figure 6F). Directly comparing the population dynamics of the tagged D1 cells to the

tagged D2 cells, shows that the D1 cells do have an exaggerated reward response (Figure 7A).

This difference in mean firing rate is not due to differences in licking behavior between the two

groups of mice (Figure 7B). Population firing rates are similar during the cue period (t = 0 to t =

1 s post cue onset, Figure 7C). The D1 population had significantly higher firing rates than the

D2 population during the reward delivery period (t = 3 to t = 3.25 s post cue onset, unpaired t

test, p = 0.0333; Figure 7D).

D1 and D2 populations are co-activated during movement initiation and termination

We were interested in how the direct and indirect pathways contribute to movement

initiation, execution, and termination, since others have found evidence that suggests the

pathways are co-activated during these times [12], [13]. Because mice initiate licks with varying

delays from cue onset throughout the session, we realigned the neural activity to the first initiated

lick within the 0-3 s cue-reward delay. We observed interesting firing patterns due to licking

behavior when examining all recorded cells (Figure 8A-F). Importantly, comparing just the

identified D1 and D2 populations, activity in both populations is elevated at the time of lick

initiation (Figure 9A) and licking behavior of both groups is similar (Figure 9B). Quantifying

the level of population activation in a window around the first lick shows a trend towards higher

activation of D1 cells, but this difference is not significant (Figure 9C). The D1 and D2

populations both have higher firing rates during the lick-initiation window when compared to

their mean baseline firing rates. We realigned the firing rates to the final lick in the licking bouts

initiated prior to reward delivery and observed neural dynamics for all cells (Figure 10A-F).

Again comparing the D1 and D2 cells, both populations show elevated, but similar, firing

dynamics (Figure 11A). Licking behavior when realigned to the final lick was also similar

51

(Figure 11B). D1 and D2 cells are comparably activated during the 1 s window surrounding the final lick issued (Figure 11C). Genetically identified D1 and D2 neurons display coordinated, elevated neural dynamics at the time of lick initiation, during continued licking, and at the time of lick termination.

2.4 Discussion

The BG play an important role in motor planning, action selection, and motivated behaviors [24]. Much has been learned about BG circuitry and the striatum, in particular, due to the number of neural disorders that affect these regions. Though studying neural disorders, such as Parkinson's disease and Huntington's disease, has led to many theories concerning BG motor circuit function, many questions remain regarding how the direct and indirect pathways function in order to produce self-initiated or motivated movements. A better understanding of the dynamic relationship between these two projections will further elucidate how the BG functions in the motor circuit with the cortex and thalamus, and could lead to new or improved therapies for movement disorders.

In this study, we optimized an optogenetic photo-identification protocol for use with silicon microprobe electrophysiological recordings in the striatum, a mostly inhibitory circuit [95]. Using this protocol, we recorded single unit activity of genetically identified D1 and D2 cells in the lateral striatum of behaving, head-fixed mice. We observed significantly increased firing during the light stimulus in the tagged cells when compared to the untagged cells. The D2 tagged cells appear to have enhanced activity compared to the D1 tagged cells. This result is consistent with a previous studies *in vitro* showing that D1 cells are less excitable than D2 cells in striatal slices from rats and mice [28], [96].

In terms of movement, previous studies have demonstrated that activation of the indirect pathway caused mice to freeze and reduced locomotion, and that activation of the direct pathway relieved hypokinetic symptoms in a parkinsonian mouse model [9]. These findings and observations of patients with movement disorders have led some researchers to believe that the direct and indirect pathways have antagonistic effects on movement [2], [5], [7]. There is increasing evidence of a more nuanced model involving co-activation in both pathways during movement and behavior [12], [13], [97], [98]. Our findings are consistent with this more complex view of BG function. We observed that both D1 and D2 cells were more active during lick initiation, continued licking, and licking termination. Our findings also support an emerging idea that specific subpopulations of D1 cells facilitate certain movements and corresponding D2 cells inhibit competing movements [99]. We also observed a significant reward response in D1 cells compared to D2 cells that is likely to due to modulation by the reward-related phasic dopamine response [19]. Evidence from *in vitro* studies [28] supports the hypothesis that D1 dopamine receptor expressing cells are positively modulated by dopamine release and D2 cells are negatively modulated [15]. To our knowledge, this is the first *in vivo* demonstration that D1 cells have an enhanced response following reward delivery. This finding suggests that the direct and the indirect pathways may have distinct functions with regard to reward learning.

Part of this study involved developing an optogenetic photo-identification protocol for use with silicon microprobe recordings of striatal dynamics. During these recordings, the silicon microprobes exhibited large voltage deflections when the laser was actuated on and off. Much of the light-associated noise was removed during pre-processing (background subtraction and bandpass filtering). However, remnants of the light artifact were sometimes counted as neuronal spiking during the laser stimulation. We believe this to be the reason that some neurons were

"tagged" in the control recordings. Other optogenetic tagging studies are careful to use only cells that respond with very short latencies (5-10 ms) in order to exclude cells that are indirectly activated by opsin-expressing neighbors. The mean latency to fire for the D1 and D2 tagged cells in this study was between 20 and 25 ms. Due to the predominantly inhibitory nature of the striatal microcircuit, we do not believe the delayed latencies reflect indirect activation, but rather are evidence of the relatively hyperpolarized resting potential of MSNs [28], [96].

This study has described D1 and D2 neural activity during a simple, Pavlovian association task, where mice perform a conditioned response (anticipatory licking) to a reward predicting cue. It would be interesting to record D1 and D2 neuron responses in a slightly more complicated task that included a cue requiring mice to withhold responding. This would allow us to compare D1 and D2 population activity during suppressed movement and potentially identify the group of D1 cells responsible for initiating a licking response and the group of D2 cells responsible for inhibiting a licking response. It would also be a natural extension of our technology to perform simultaneous recordings of D1 or D2 populations in the striatum and populations in the SNr, thalamus, or even the cortex. This might allow one to see evidence of direct and indirect pathway dynamics and resulting activity in downstream regions.

The findings reported here demonstrate that both D1 and D2 neurons show increased firing rates during movement initiation and continued action. These observations are consistent with recent evidence showing coordinated activation of direct and indirect pathways within the BG during self-initiated movement and motivated behaviors. This paper also describes a significantly higher reward response in D1 cells compared to D2 cells which could signify a unique role for the direct pathway in reinforcement learning. Further studies of the direct and indirect pathways will help to clarify their respective roles in processes that involve BG circuitry.

54

2.5 Figures
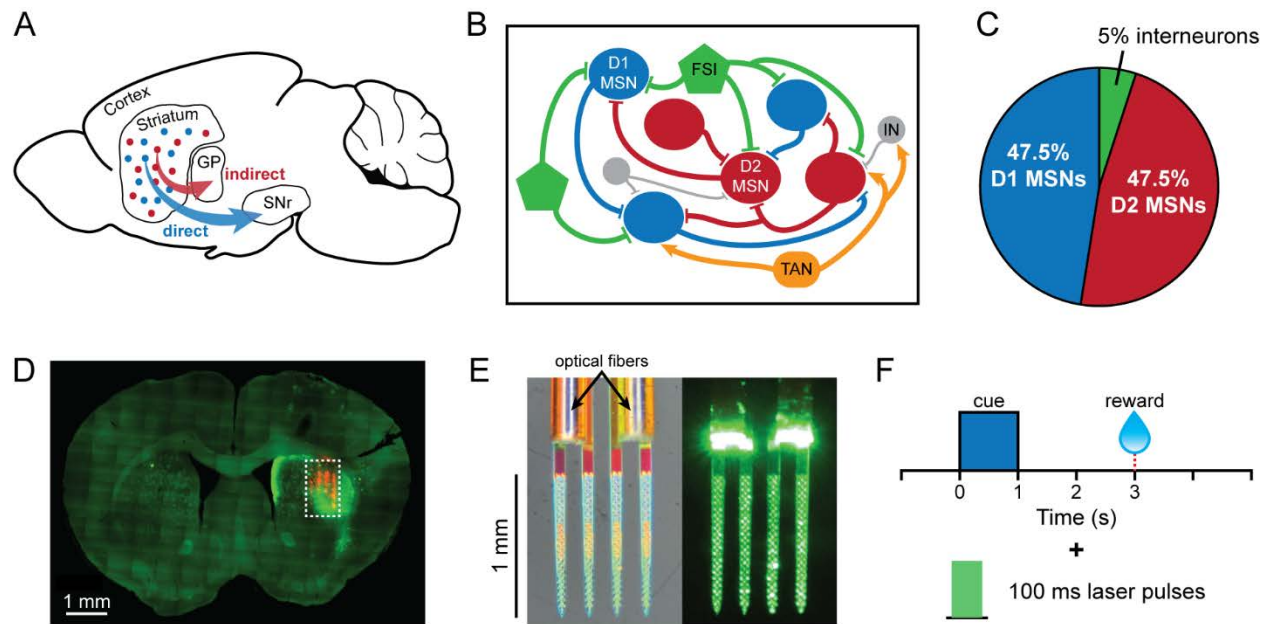
Figure 1: Optogenetically targeting the direct and indirect pathways

A. Sagittal depiction of the direct pathway projection from the striatum to the substantia nigra pars reticulata (SNr) and the indirect pathway projection from the striatum to the external segment of the globus pallidus (GPe).

B. Simplified diagram of the striatal microcircuit depicting collateral projections between both populations of D1 (direct pathway projecting) and D2 MSNs (indirect pathway projecting).

C. Breakdown of striatal cell type. Together D1 and D2 MSNs make up ~95% of the total neuron population. The other 5% are interneurons of various types.

D. Confocal microscope image of opsin expression and opto-microprobe placement (white dashed rectangle) in the lateral striatum. The brain was coronally sectioned at 100 µm and imaged for tdTomato, the fluorescent reporter on the opsin, and DiD, a fluorescent dye painted on the opto-microprobe prior to each recording.

E. Image of the opto-microprobe used for electrophysiological recording in this study with laser off (left) and laser on (right). It is a 256 electrode silicon microprobe with two optical fibers (200 µm diameter, 0.22 NA) attached for local light delivery.

F. On the recording day, mice experienced 100-150 pairings of a previously trained odor cue (1 s duration) and reward (3 s delay from cue onset). A light stimulation protocol followed the behavior session. We stimulated using 100 ms continuous laser pulses, 50 each at three power levels: 1 mW, 5 mW, and 10 mW.
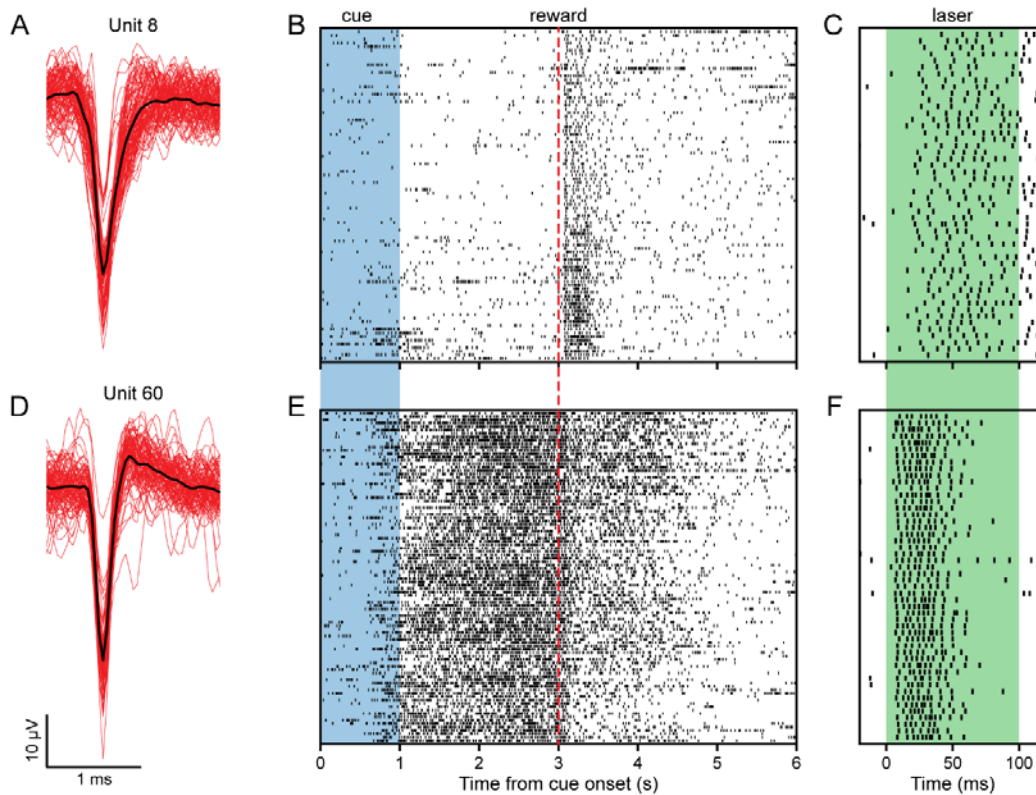
Figure 2: Single units had varying responses to the behavioral task and light stimulation

A. The mean waveform (black) plotted over individual spike waveforms (red) for sample unit 8.

B. Spiking raster plot for unit 8 with time from cue onset as the x-axis and different presentations of the cue-reward pairing on the y-axis. Unit 8 fires more after reward delivery.

C. Spiking raster plot for unit 8 with respect to 50 laser pulses.

D. The mean waveform (black) plotted over individual spike waveforms (red) for sample unit 60.

E. Spiking raster plot for unit 60 with time from cue onset as the x-axis and different presentations of the cue-reward pairing on the y-axis. Unit 60 begins firing during the odor cue presentation and continues for several seconds following reward delivery.

F. Spiking raster plot for unit 60 with respect to 50 laser pulses.
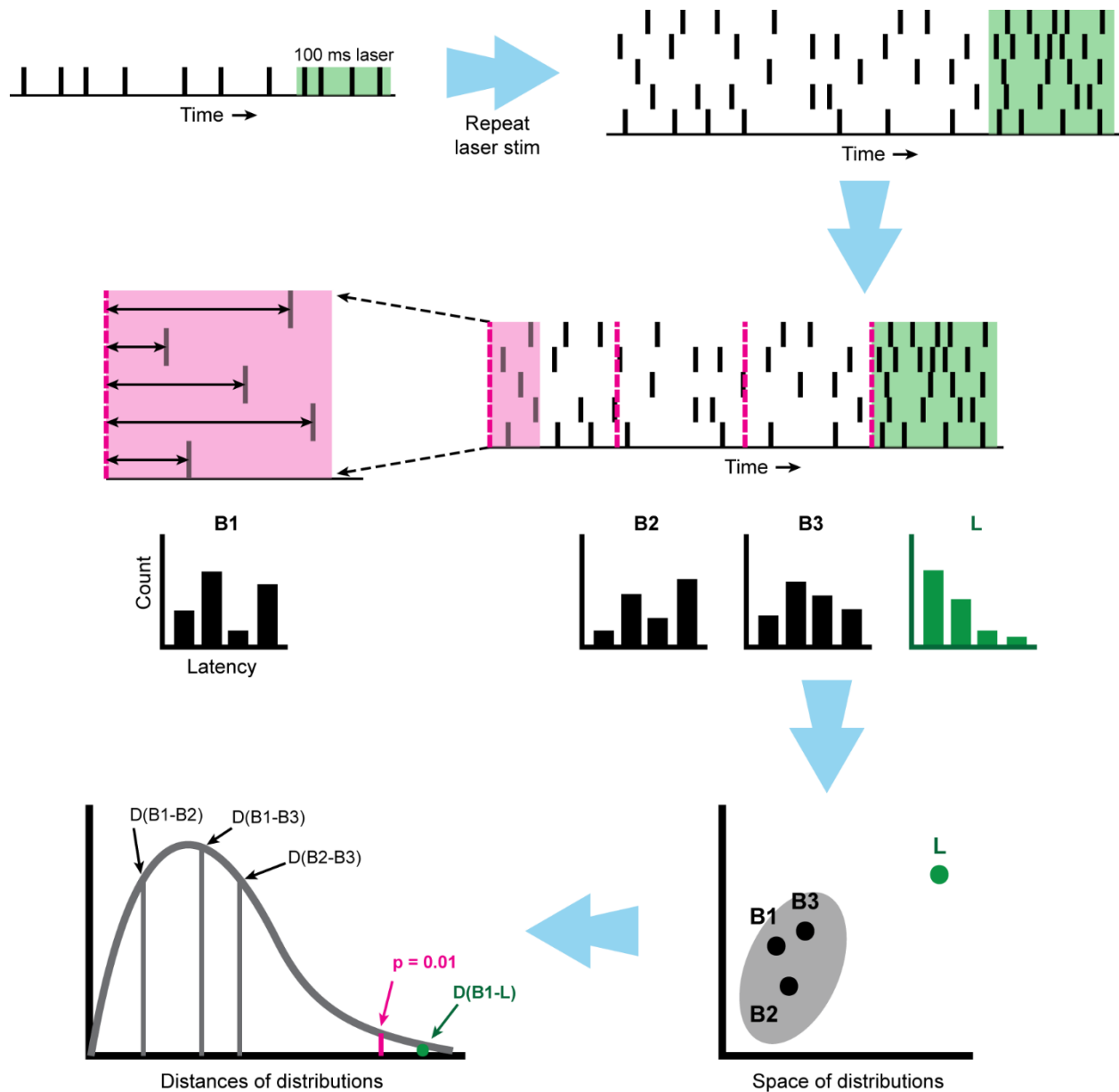
Figure 3: Stimulus-Associated spike Latency Test diagram

The test for determining whether a unit was significantly activated or "tagged" by the 100 ms

laser pulses was devised by Kvitsiani and colleagues called the Stimulus-Associated spike

Latency Test (SALT). SALT is a statistical measure of whether optogenetic stimulation changes

a cell's spike timing. It looks at windows of time associated with baseline firing (when no

outside stimulus has been presented) and windows that coincide with the onset of the laser

stimulus. A histogram of the latencies to the first spike within the window is created for multiple baseline-associated windows and the laser-associated window. The distances between the latency distributions are calculated using a modified Jensen-Shannon divergence measure. Using this metric, SALT tests the hypothesis that the laser-associated distribution is different from the baseline distributions and gives each unit a p-value. We ran the SALT test with a window size of 30 ms and "tagged" units that had p < 0.01. This diagram is a reproduction of Supplementary Figure 11: Visual description of optical tagging test (SALT), from [27].
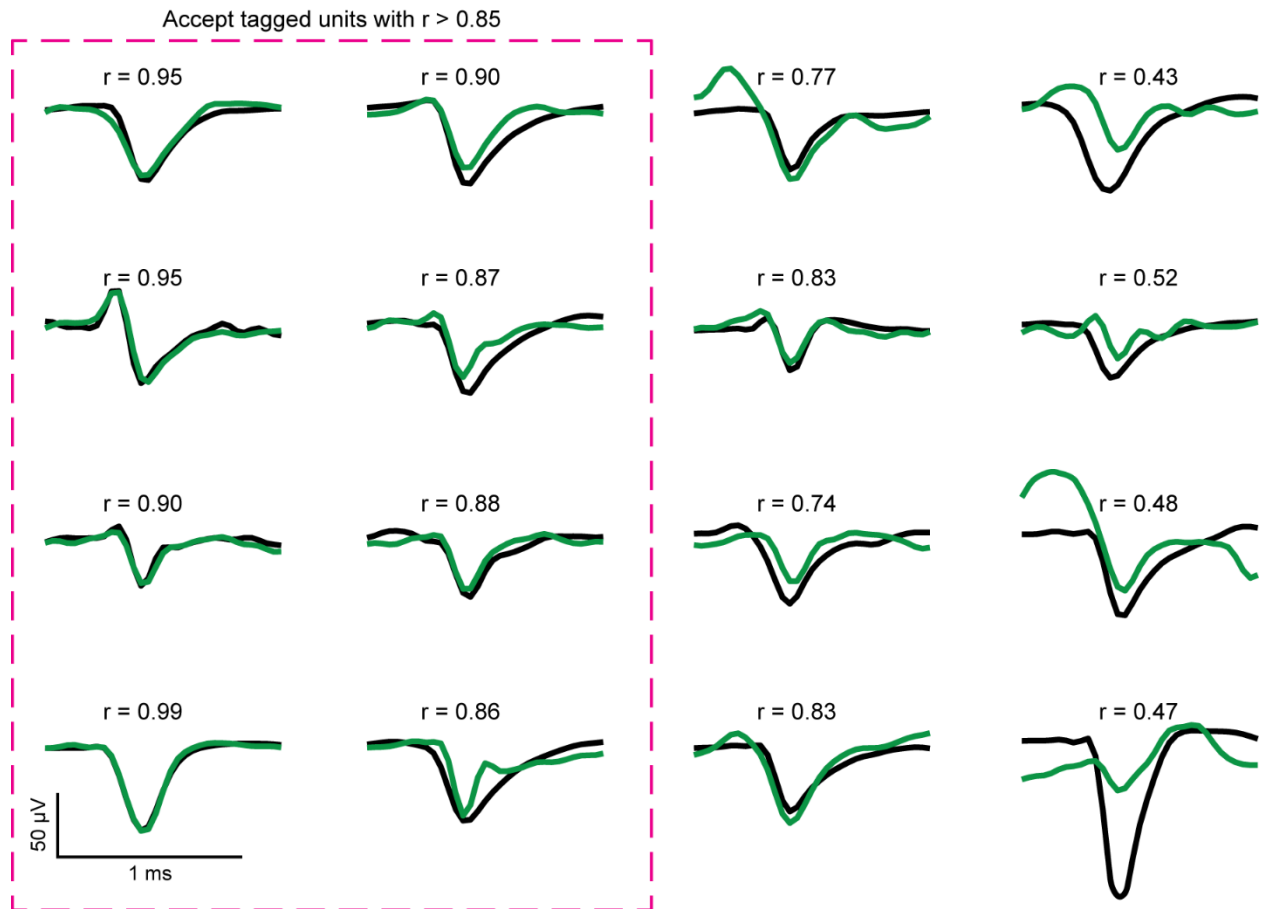
Figure 4: Spike waveform correlation of sample units

We calculated the Pearson's correlation coefficient, r, of the mean baseline spike waveform (black) and the mean first laser-induced spike waveform (green) for all units. Units with a waveform correlation r > 0.85 (outlined by pink dashed line) were accepted as "tagged" if they also passed SALT.
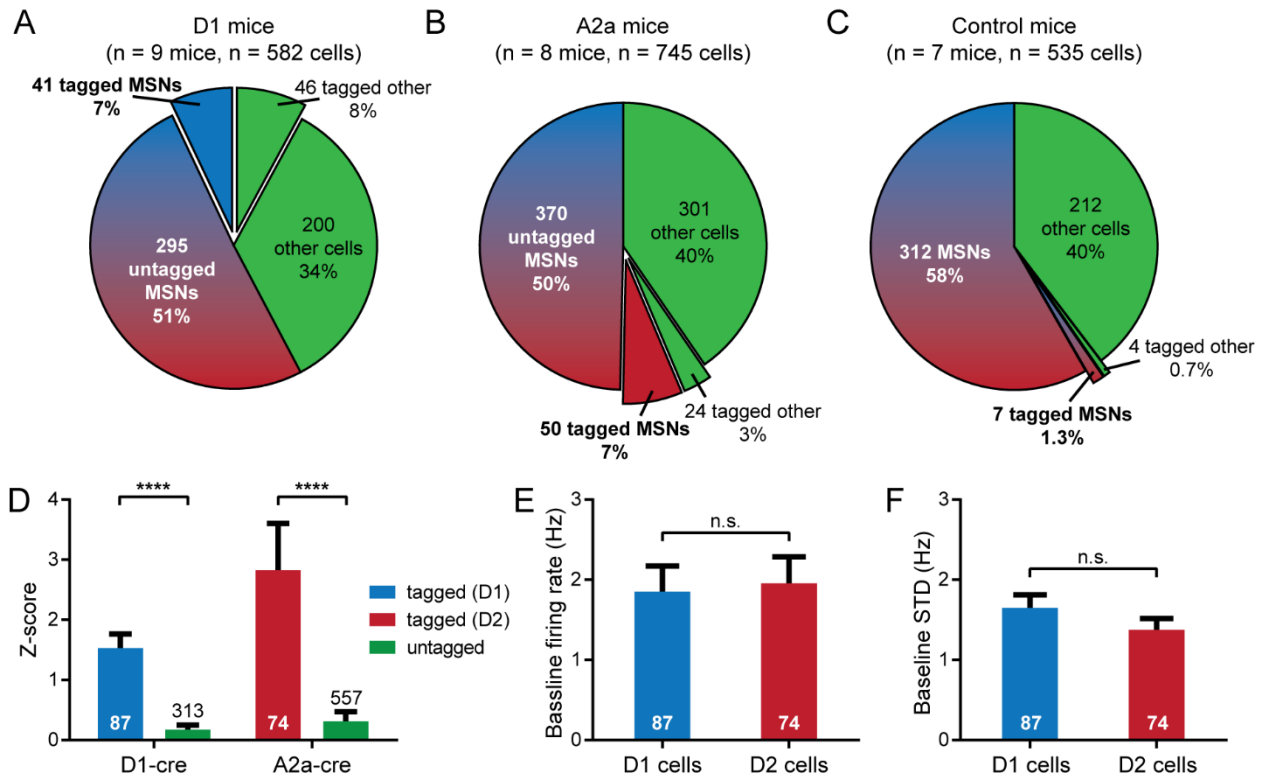
Figure 5: Optogenetically identified D1 and D2 cells show similar baseline firing characteristics

A. We recorded from D1-cre mice (n = 9 mice, n = 582 single units) expressing ChrimsonR in D1 cells (direct pathway). Tagged cells (n = 87) represent positively identified D1 cells.

B. We recorded from A2a-cre mice (n = 8 mice, n = 745 single units) expressing ChrimsonR in D2 cells (indirect pathway). Tagged cells (n = 74) represent positively identified D2 cells.

C. We performed control recordings in a subset of animals (n = 1 D1- and 6 A2a-cre mice, n = 535 single units) by inserting the opto-microprobe in the non-injected striatum. Tagged cells (n = 11) represent the low numbers of false positive tagged cells.

D. Mean z-score of light-stimulated firing of all cells from D1-cre mice (left) and A2a-cre mice (right) during the 10 mW laser pulses. The tagged cells from the D1-cre mice (blue) were significantly more activated by the laser than the untagged cells from these recordings

(green) (n = 87 tagged and 313 untagged, unpaired t test, p < 0.0001). The tagged cells from

the A2a-cre mice (red) were also significantly more activated by the laser than the untagged

cells from these recordings (green) (n = 74 tagged and 557 untagged, unpaired t test, p <

0.0001).

E. Mean baseline firing rates for D1 cells (blue) were not significantly different from mean

baseline firing rates for D2 cells (red) (n = 87 D1 and 74 D2 cells, unpaired t test, p = 0.804).

F. Standard deviation of baseline firing rates for D1 cells (blue) were not significantly different

from those for D2 cells (red) (n = 87 D1 and 74 D2 cells, unpaired t test, p = 0.141).
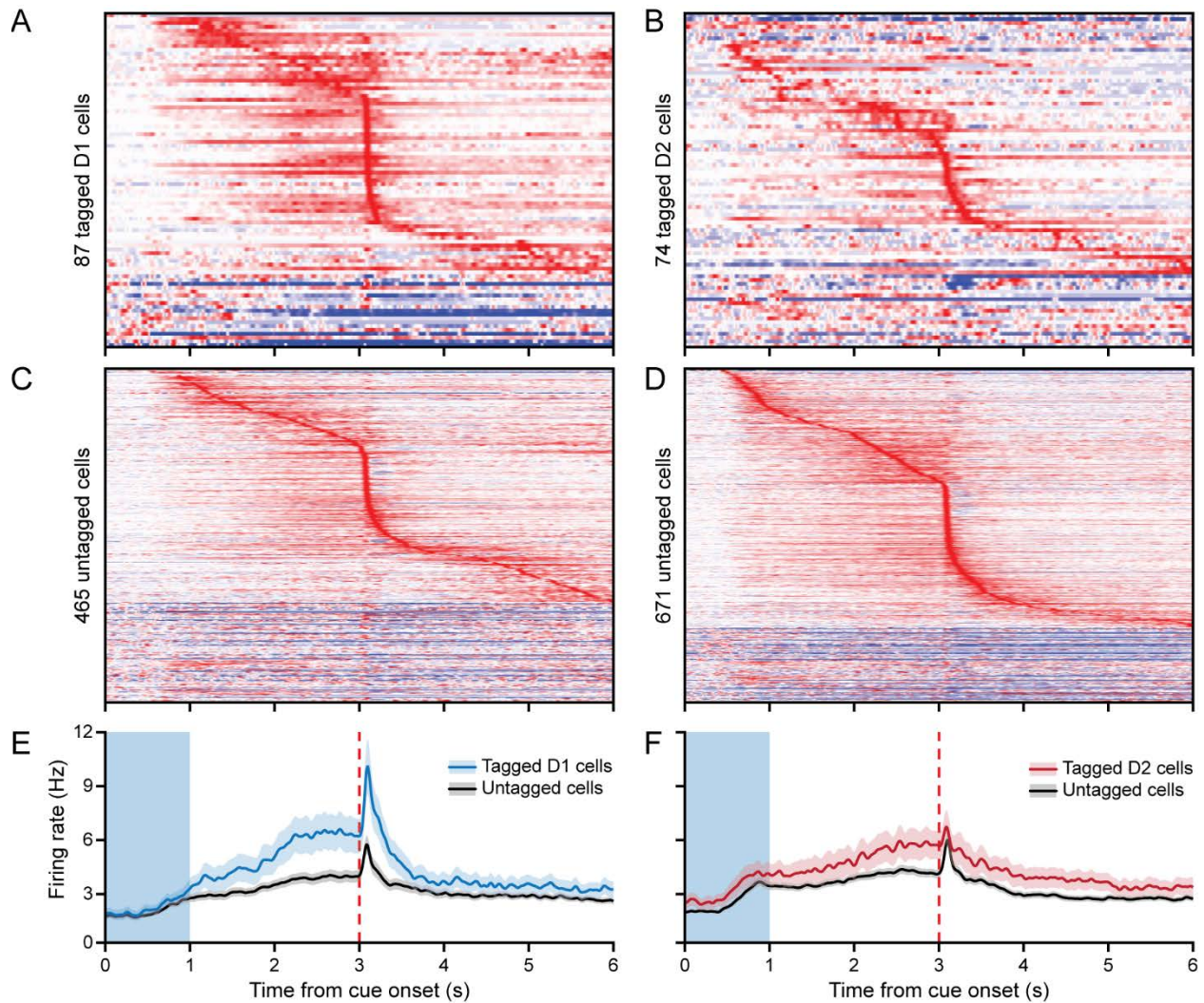
Figure 6: Strong activation to Pavlovian task features in D1 and D2 cells, as well as untagged cell populations

A. Mean evoked activity of positively identified D1 cells (n = 87) aligned to cue onset for correct trials. Activity is plotted from t = 0 to t = 6 s post stimulus onset as the normalized difference in firing rate relative to a baseline period prior to cue onset. Units are ordered according to their latency to peak firing.

B. Mean evoked activity of positively identified D2 cells (n = 74). Activity is plotted as described in **A**.

63

C. Mean evoked activity of all untagged cells from D1 recordings (n = 465). This subpopulation likely represents a large proportion of D2 cells and some D1 cells that were not tagged.

D. Mean evoked activity of all untagged cells from A2a recordings (n = 671). This subpopulation likely represents a large proportion of D1 cells and some D2 cells that were not tagged.

E. Mean population firing rate of positively identified D1 cells (blue) and all untagged cells from the D1-cre recordings (black). Activity is plotted from t = 0 to t = 6 s post stimulus onset. Blue shaded rectangle from t = 0 to t = 1 s represents the cue period and the red dashed line at t = 3 s denotes time of reward delivery.

F. Mean population firing rate of positively identified D2 cells (red) and all untagged cells from the A2a-cre recordings (black). Activity is plotted as described in **E**.
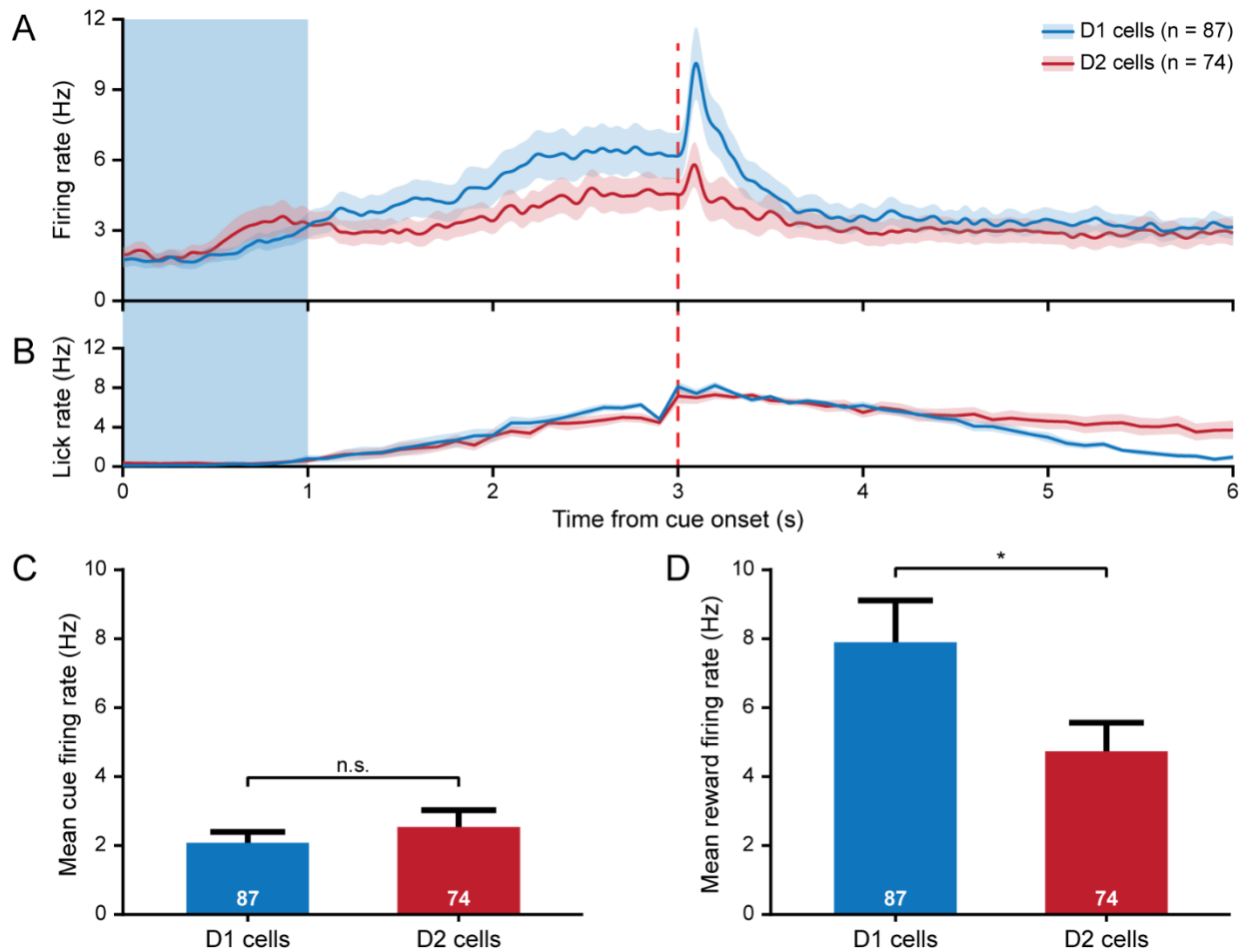
Figure 7: D1 and D2 task-evoked activation patterns show a significantly elevated reward response in the D1 population

A. Mean population firing rate of positively identified D1 cells (blue, n = 87) and positively identified D2 cells (red, n = 74). Activity is plotted from t = 0 to t = 6 s post stimulus onset. Blue shaded rectangle from t = 0 to t = 1 s represents the cue period and the red dashed line at t = 3 s denotes time of reward delivery.

B. Mean lick rate of D1-cre mice (blue, n = 9 mice) and A2a-cre mice (red, n = 8 mice) on correct trials. Licking behavior is plotted as described in **A**.

C. Mean cue-evoked firing rates (t = 0 to t = 1 s post cue onset) for D1 cells (blue) were not significantly different from mean cue-evoked firing rates for D2 cells (red) (n = 87 D1 and 74 D2 cells, unpaired t test, p = 0.3819).

D. Mean reward-evoked firing rates (t = 3 to t = 3.25 s post cue onset) for D1 cells (blue) were significantly elevated compared to mean reward-evoked firing rates for D2 cells (red) (n = 87 D1 and 74 D2 cells, unpaired t test, p = 0.0333).
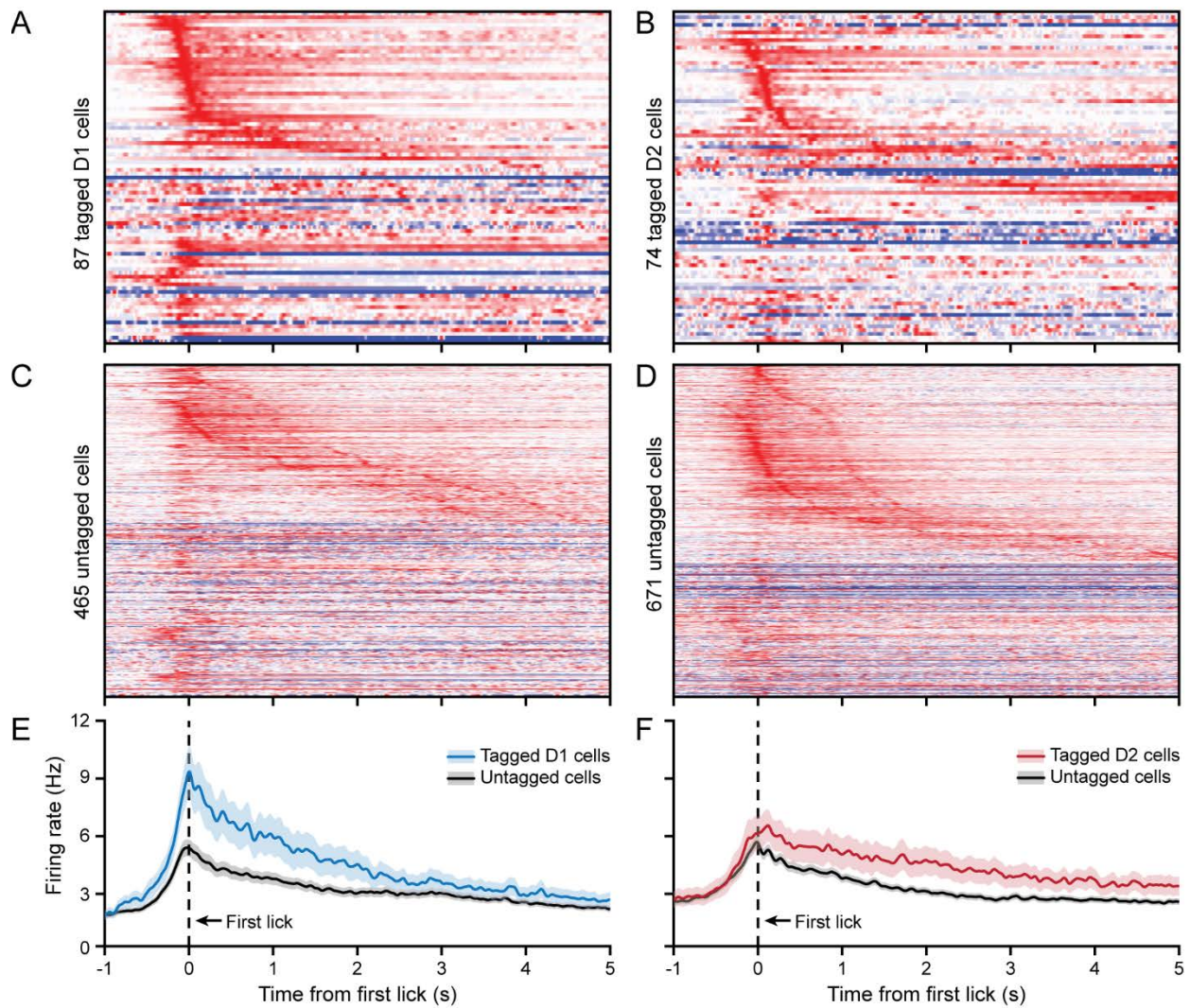
Figure 8: Dynamic activity patterns for D1 and D2 populations aligned to first lick

A. Mean evoked activity of positively identified D1 cells (n = 87) aligned to anticipatory lick initiation for correct trials. Activity is plotted from t = -1 to t = 5 s post lick initiation as the normalized difference in firing rate relative to a baseline period prior to trial onset. Units are ordered according to their latency to peak firing.

B. Mean evoked activity of positively identified D2 cells (n = 74).

C. Mean evoked activity of all untagged cells from D1 recordings (n = 465).

D. Mean evoked activity of all untagged cells from A2a recordings (n = 671).

E. Mean population firing rate of positively identified D1 cells (blue) and all untagged cells from the D1-cre recordings (black). Activity is plotted from $t = -1$ to $t = 5$ s post lick initiation. Black dashed line at $t = 0$ s denotes time of first anticipatory lick.

F. Mean population firing rate of positively identified D2 cells (red) and all untagged cells from the A2a-cre recordings (black). Activity is plotted as described in **E**.
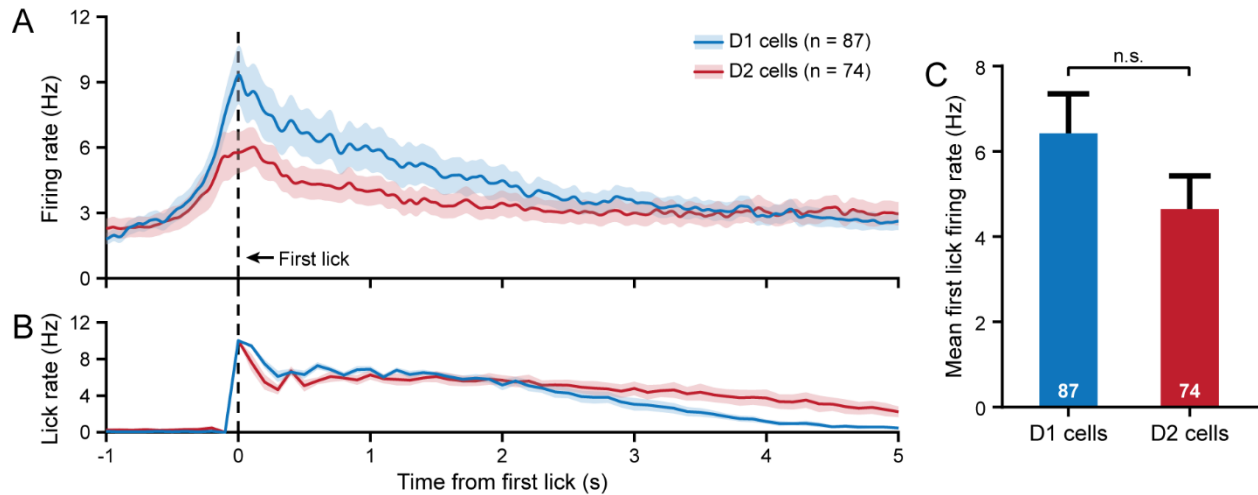
Figure 9: D1 and D2 lick-evoked activation patterns show enhanced firing for both populations during lick initiation and continued licking

A. Mean population firing rate of positively identified D1 cells (blue, n = 87) and positively identified D2 cells (red, n = 74). Activity is plotted from t = -1 to t = 5 s post lick initiation. Black dashed line at t = 0 s denotes time of first anticipatory lick.

B. Mean lick rate of D1-cre mice (blue, n = 9 mice) and D2-cre mice (red, n = 8 mice) on correct trials. Licking behavior is plotted as described in **A**.

C. Mean licking-evoked firing rates (t = -0.5 to t = 0.5 s post lick onset) for D1 cells (blue) and D2 cells (red) were elevated, but not significantly different from each other (n = 87 D1 and 74 D2 cells, unpaired t test, p = 0.1394).

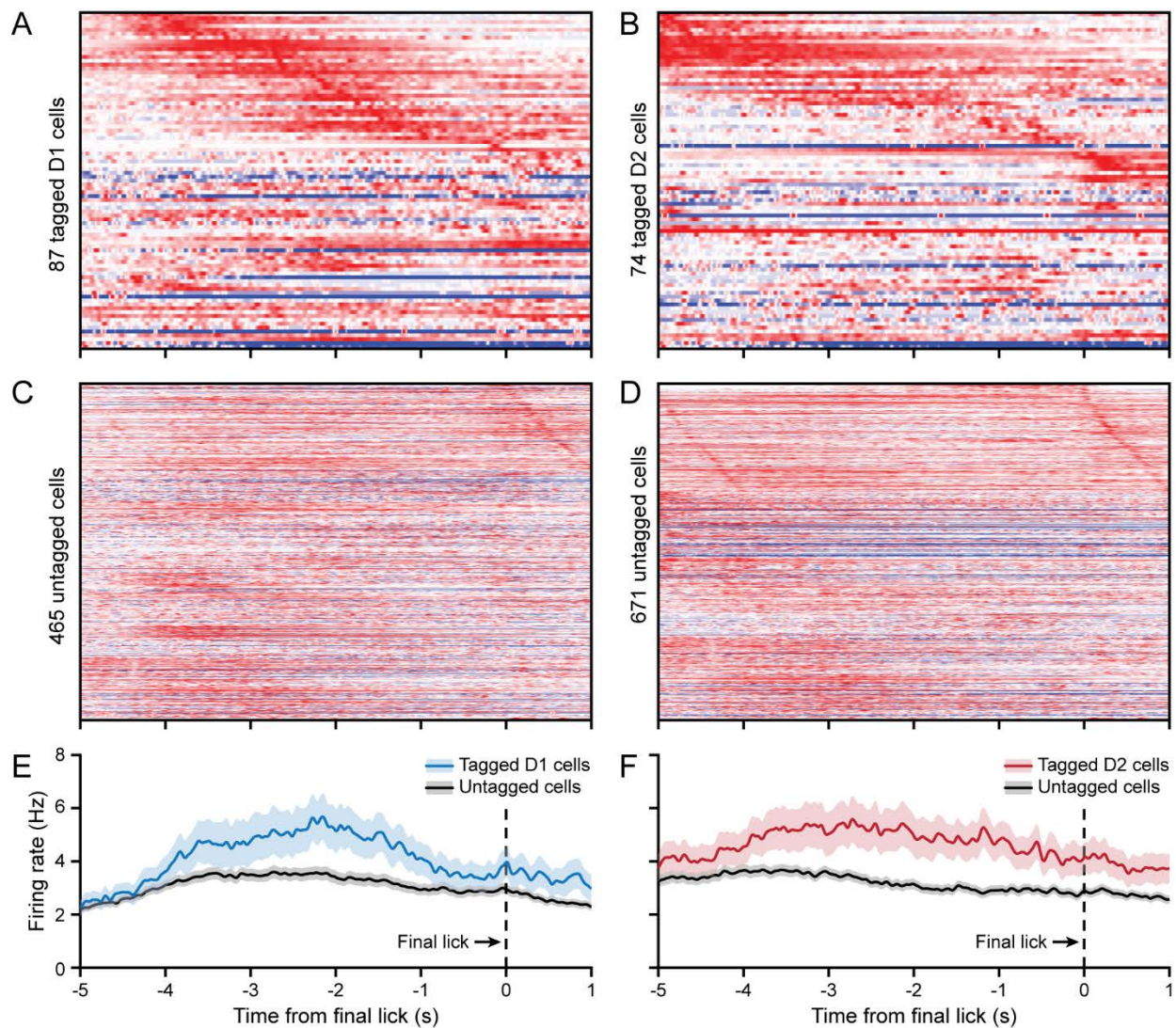**Figure 10: Dynamic activity patterns for D1 and D2 populations aligned to final lick**

A. Mean evoked activity of positively identified D1 cells (n = 87) aligned to final lick for correct trials. Activity is plotted from t = -5 to t = 1 s post lick termination as the normalized difference in firing rate relative to a baseline period prior to trial onset. Units are ordered according to their latency to peak firing.

B. Mean evoked activity of positively identified D2 cells (n = 74).

C. Mean evoked activity of all untagged cells from D1 recordings (n = 465).

D. Mean evoked activity of all untagged cells from A2a recordings (n = 671).

70

E. Mean population firing rate of positively identified D1 cells (blue) and all untagged cells from the D1-cre recordings (black). Activity is plotted from t = -5 to t = 1 s post lick termination. Black dashed line at t = 0 s denotes time of final lick in cue initiated licking bout.

F. Mean population firing rate of positively identified D2 cells (red) and all untagged cells from the A2a-cre recordings (black). Activity is plotted as described in **E**.

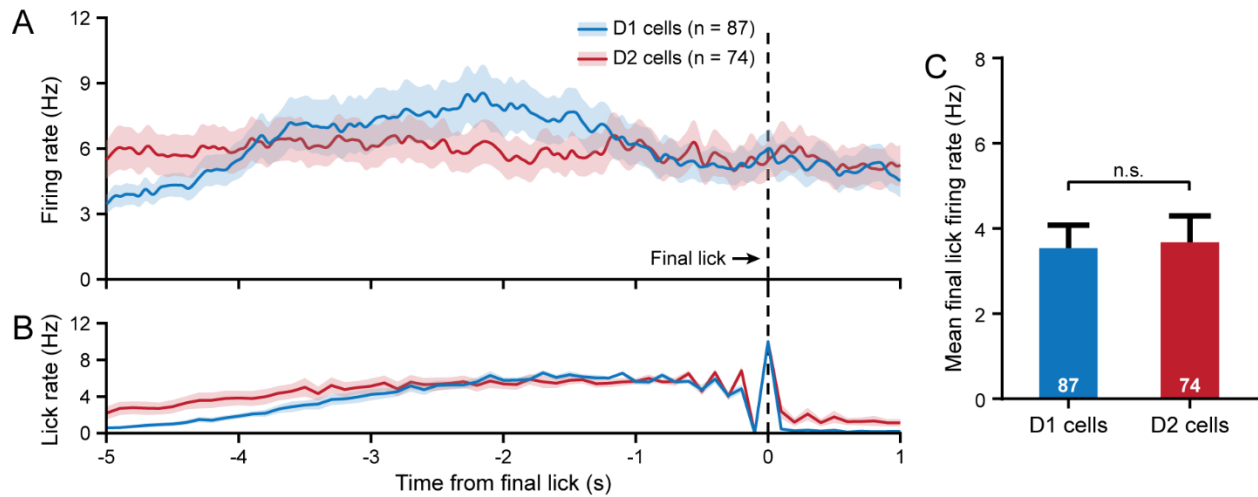**Figure 11: D1 and D2 lick-evoked activation patterns aligned to the final lick are similar**

A. Mean population firing rate of positively identified D1 cells (blue, n = 87) and positively identified D2 cells (red, n = 74). Activity is plotted from t = -5 to t = 1 s post lick termination. Black dashed line at t = 0 s denotes time of final lick in cue-initiated licking bout.

B. Mean lick rate of D1-cre mice (blue, n = 9 mice) and A2a-cre mice (red, n = 8 mice) on correct trials. Licking behavior is plotted as described in **A**.

C. Mean licking-evoked firing rates (t = -0.5 to t = 0.5 s post final lick) for D1 cells (blue) were not significantly different from mean licking-evoked firing rates for D2 cells (red) (n = 87 D1 and 74 D2 cells, unpaired t test, p = 0.8606).

CHAPTER 3

The role and timing of dopaminergic signaling in Pavlovian conditioning

3.1 Introduction

An animal's ability to make accurate predictions about outcomes using environmental stimuli can enhance its chances of survival. A particular scent can warn of an approaching predator or indicate a hidden cache of food. Detection and identification influence an animal's behavioral choice; the right choice leads to survival/reward and the wrong choice could lead to death. Making appropriate predictions allows animals, as well as humans, to prepare reactions in advance, often leading to higher success at avoiding detrimental outcomes. Studying the systems involved in associative learning has also been relevant to the study of the habit-forming properties of drugs of abuse [100], [101]. Beginning in the 1950s, researchers began to identify brain systems involved in reward processing [102]. One such system that has become the principal focus of research pertaining to reward processing is the dopaminergic system [19], [100], [103]–[105].

The seminal theoretical model of learning, reward prediction error (RPE), was described by Rescorla and Wagner in 1972 [106]. They state the central notion of their theory in the following manner: "organisms only learn when events violate their expectations." In the context of a simple Pavlovian conditioning paradigm, if a neutral stimulus (or conditioned stimulus, CS) is repeatedly presented followed by an appetitive stimulus (unconditioned stimulus, US) animals will learn that the CS is predictive of the US and may acquire a specific behavioral response (conditioned response, CR). Animals continue to display the CR when presented with the CS-US pairing. The animal's behavioral response will change only if the nature of the US changes, such as for a different less/more rewarding outcome. Over the last few decades our understanding this type of Pavlovian or associative learning has come a long way. In 1997, Schultz et al. showed that a majority of dopamine neurons (55-80%) exhibited a strong, transient

activation following delivery of a liquid reward to a primate's mouth [19]. Schultz also reported that the phasic response would shift from the US to the CS through repeated presentations of a CS-US pairing. Due to the dopamine neuron activity patterns observed, they suggested that dopamine was very likely a neural substrate for RPE, and posited that dopaminergic signaling was important for the animal to learn the CS-US association.

The dopamine system is commonly studied with respect to reward learning, however it is also implicated in motor control. Parkinson's disease is characterized by degeneration of dopamine cells in the substantia nigra pars compacta (SNc) and causes severe motor impairments, such as bradykinesia and tremors [107]–[109]. It is thought that motor symptoms arise due to abnormal activity of the direct and indirect pathways in the striatum caused by a paucity of dopamine innervation, as normal or near-normal motor function is often rescued by electrical stimulation of the SNc or treatment with dopamine supplements [110]–[112]. Studies in animals have provided evidence to support dopamine's role in movement, showing that dopamine neurons appear to encode movement related information [113]–[117]. Some of these studies provide evidence supporting the role of dopamine in both locomotion and reward processing [113], [115], [117]. While others suggest that, rather than encoding RPE as described by Schultz et al., the dopamine neurons solely play a role in controlling the kinematics of voluntary movements [114], [116].

Subsequent studies have also provided evidence of the correlation between associative learning and dopamine signaling, both in dopamine neurons and their axons in downstream regions [118], [119]. Increasingly meaningful are the studies that sought to disrupt dopamine activity to provide a more causative link between learning and dopamine signaling [22], [23]. These works, however, relied upon genetic knockouts or pharmacological manipulations that

lack the temporal or cell-type specificity to probe the dopamine transients. Optogenetics is a great candidate for studying dopaminergic functions because of the high temporal control it provides over neurons. Optogenetic techniques have recently been employed to study different aspects of dopaminergic signaling with respect to associative learning and movement. Dopamine neurons have been stimulated with excitatory opsins to show that dopamine release can cause conditioned place preference and is reinforcing [21], [120]. It was also demonstrated that dopamine activity can act as a positive RPE signal to unblock learning [121].

While studies have shown that dopamine neuron inhibition can function as negative RPE in an over-expectation paradigm [122] and in an unblocking task [123], there has not been a systematic test of the relevance and timing for dopaminergic activity during a simple Pavlovian conditioning task. Studies have also shown that optogenetic manipulations of dopamine neurons can influence movement initiation [115]–[117], however these studies focus on locomotion only. Many studies have recorded dopaminergic activity in the ventral tegmental area (VTA) and in regions that it projects to such as the striatum and nucleus accumbens, however, there are few reported dopamine manipulations at the level of the axons. To address these experimental gaps, we investigated the role of dopamine in Pavlovian conditioning using optogenetic techniques. This study describes the effects on learning and licking behavior of bidirectionally manipulating dopaminergic signaling at the level of cell bodies and axons at different time points throughout a Pavlovian conditioning task.

3.2 Methods

Surgical procedures

All procedures were approved by the University of California, Los Angeles Chancellor's Animal Research Committee. Singly housed male and female DAT-cre mice (n = 36, 12-16 weeks old, The Jackson Laboratory) were used in the experiments. Animals underwent a surgical procedure under isoflurane anesthesia in a stereotaxic apparatus. The procedure consisted of cementing stainless steel head restraint bars to the skull (10 mm x 7.5 mm, 0.6 g, laser cut at Fab2Order), injecting an adeno-associated virus (AAV, University of North Carolina Vector Core), and implanting permanent optical fibers coupled to ceramic ferrules (200 μm diameter, 0.22 NA, Thorlabs). The AAV was injected using glass micropipettes (Nanoject II, Drummond Scientific) into the ventral tegmental area and substantia nigra pars compacta (VTA/SNc) bilaterally at a volume of 600 nL per hemisphere. Injection coordinates targeting the VTA/SNc were 3.3 mm posterior, 1.2 mm lateral, and 4 mm ventral to bregma. For the dopamine inhibition experiments we used AAV5/EF1a-DIO-eNpHR3.0-eYFP, for excitation experiments we used AAV5/Svn-Flex-Chrimson R-tdTomato, and for control experiments we used AAV5/EF1a-DIO-eYFP. Optical fibers were placed bilaterally 0.2 mm above the injection site for all animals that underwent dopamine cell body manipulations. For the group of ChrimsonR$^+$ mice where we attempted dopamine projection excitation in the lateral striatum, the coordinates used for bilateral optical fiber placement were 1 mm anterior, 2.4 mm lateral, and 3.1 mm ventral from bregma. Mice received a carprofen injection (5 mg/kg, s.c.) on the day of the surgical procedure and daily injections for the subsequent two days. Mice were also given drinking water containing ibuprofen and amoxicillin for a week following surgery.

Behavioral task

After one week of recovery from the surgery, animals were single-housed, food restricted, and fed daily after each training session to maintain ~90% of their baseline weight. They received water ad libitum. During daily training sessions, animals were mounted with the head bar bracket on a behavioral testing rig and on top of a fixed spherical treadmill (200 mm diameter, Graham Sweet Studios). A reward solution (5 µL, 10% sweetened condensed milk) was dispensed from a tube positioned between an infrared beam lick meter (Island Motion), and its delivery was signaled by an audible solenoid valve actuation (Neptune Research 161T010). Initially, animals were habituated to head fixation and trained to consume the reward. During the habituation phase mice learned to associate the solenoid actuation sound with a reward, and after consuming at least 90% delivered rewards for two consecutive days, they began Pavlovian conditioning with olfactory cues. Odorants were introduced via an olfactometer by bubbling air (0.15 L/min) through aromatic liquids diluted 1:10 in mineral oil (Sigma-Aldrich), and mixing this product with the 1.5 L/min main stream of air. The CS odor was amyl acetate (banana). The odor was presented for 1 s, followed by a delay of 2 s, then delivery of 5 µL of the reward solution (18-30 s ITI, 100 rewarded trials per day). During training mice started to lick in anticipation of the reward (in the interval between odor onset and reward; 0-3 s). Mice experienced three to five days of Pavlovian training prior to behavioral tests with optical stimulation.

Optical stimulation

To allow adequate time for opsin expression, mice were given at least three weeks prior to optical stimulation of VTA/SNc dopamine cell bodies and at least four weeks for dopamine projection stimulation in the lateral striatum. On test days, mice experienced 120 trials per day

divided into three consecutive blocks: the first and last block of 40 trials were always normal CS-US pairings and the middle block consisted of 40 test trials often including optical stimulation (except in the case of the extinction only test). Cell bodies or projections expressing opsins were stimulated through the implanted optical fibers via a 50/50 optical splitter (Thorlabs) by a 532 nm or 589 nm laser (Opto Engine). The power output was calibrated to 10 mW per fiber before each behavioral test. Performance on the test days was calculated individually for each block of trials as the percent of trials where the mouse started licking during the CS-US delay (0-3 s from odor onset). Mice experienced as many as six test days (with different laser stimulation timing), which were randomized to counter-balance learning-related effects with respect to the laser.

Histology and optical fiber position determination

Following the completion of the behavioral tests, the brain was coronally sectioned at 100 μm on a vibrating blade microtome (VT1000E, Leica) and individual sections were placed in order into a 24-well plate containing phosphate buffered solution (PBS). Immunohistochemistry was performed on slices using standard procedures to confirm opsin expression and correct placement of the optical fibers in the regions of interest. Sections were stained for the fluorescent tag (YFP or tdTomato) attached to each of the optogenetic constructs. Only mice with equal levels of expression and correct positioning of the optical fibers were included in the analysis.

Statistical Tests

All statistical analyses were performed using standard Matlab functions and Prism software. Information about the exact value of n, what n represents, statistical test used, and p-value is provided in the main text and/or figure captions. All plotted data represent mean ± SEM. In the figure legends, **** denotes $p < 0.0001$, ** $p < 0.01$, and * $p < 0.05$.

3.3 Results

Dopamine signaling is more important after reward

We trained head-fixed mice in a Pavlovian conditioning task in which an olfactory cue (CS) was predictive of a sweetened condensed milk reward (US) (Figure 1A). With continued presentations of the cue-reward pairing, mice started to lick prior to delivery of the US, showing that they associated the odor cue with the reward delivery. Performance was measured as the percentage of trials in which mice initiated a licking response in anticipation of the reward delivery (0-3 s). In order to investigate the role that dopaminergic signaling plays in this task, we injected an adeno-associated virus containing a cre-driven halorhodopsin (NpHR3.0) into the VTA/SNc of DAT-cre mice. We observed good levels of NpHR3.0 expression (bright green, Figure 1B) in the VTA/SNc. Two optical fibers implanted bilaterally over the VTA/SNc allowed us to direct laser light (532 nm) to the opsin-expressing cells with precise temporal resolution (white dashed rectangles, Figure 1B).

After mice reached an asymptotic level of performance on the Pavlovian task (> 80% trials with anticipatory licking), they entered the test phase. On a test day, mice experienced three blocks of forty trials: forty normal CS+ trials, forty CS+ trials with a continuous laser pulse, and then forty more normal CS+ trials. Via the laser, we attempted to depress dopamine neuron activity throughout each trial in the middle block to test whether dopaminergic signaling was necessary during the trial to maintain the cue-reward association. The laser was turned on 1 s prior to cue onset and remained on until 2 s after reward delivery (6 s continuous laser pulse, Figure 1C, top). Soon after the start of the laser block, mice dramatically reduced their anticipatory licking (Figure 1C, bottom). The inhibition of the dopamine neurons was not sufficient to prevent the consummatory licking after reward delivery, however. At the end of the

laser block, when normal CS+ trials resumed, mice resumed anticipatory licking. Performance

was analyzed independently for each block of forty trials to quantify the effect of dopamine

inhibition on the anticipatory licking behavior. Inhibiting dopaminergic signaling significantly

and reversibly reduced the conditioned response in the form of anticipatory licking (Figure 1D).

This behavioral effect mimics extinction because mice did not immediately stop licking once the

laser turned on. In fact, the rate at which they stopped licking was similar to the rate at which

mice stopped licking during actual extinction (Figure 1E).

According to RPE theory, learning occurs when the predicted outcome of a CS differs

from the actual outcome [106]. It has been shown that dopamine activity increases to the CS in

primates and rodents during Pavlovian conditioning and is likely the neural substrate of RPE

[19], [118], [119]. Dopamine has also been shown to be involved in movement generation

[114]–[117]. We wanted to investigate the roles of CS- and US-triggered dopamine signals in

generating the conditioned response and maintaining the CS-US association. We performed

another set of tests with the same cohort of NpHR3.0+ mice where the laser pulse was delivered

at different times during the task. On one test day, the test block trials included a laser pulse

prior to the CS and turned off just before reward delivery (4 s continuous laser pulse). On

another test day, the laser was turned on at the time of US delivery and turned off after 2 s (2 s

continuous laser pulse, Figure 2A). Surprisingly, the CS-dopamine inhibition had no effect on

behavior whereas the US-dopamine inhibition again caused a significant decrease in conditioned

responding (Figure 2B) similar to the 6 s laser test.

Timing of dopaminergic signaling

Next we wanted to interrogate the timing of the US-related dopaminergic signal, since

our optogenetic manipulations offer enhanced temporal resolution over previously used

81

techniques such as lesions and pharmacological manipulations. Studies have found evidence that

the pattern of dopamine neuron activity released levels of dopamine at the projection sites that

remained elevated for around 500 milliseconds [124], [125]. We performed more tests with the

NpHR3.0$^+$ cohort where the 2 s laser pulse was incrementally delayed in time from the reward

delivery. Including the previous test in which the 2 s laser started at the time of US, we tested

0.25, 0.5, and 1 s delay (Figure 3A-B). Behavioral performance incrementally returned to

control group levels as the reward-laser pulse delay increased. When the dopamine inhibition

was more than 0.5 s away from the US, the performance of the NpHR3.0$^+$ group was no longer

significantly different from the YFP$^+$ group (Figure 3C).

Dopamine is sufficient to maintain conditioned responding

In order to test if dopamine is sufficient to maintain the anticipatory behavior, we

performed behavioral tests that included dopamine cell body stimulation in place of the US. For

these experiments we used a cohort of DAT-cre mice expressing the excitatory opsin ChrimsonR

in the VTA/SNc dopaminergic cells with bilateral optical fibers over the area. On test day, again

mice received three sets of 40 trials, the first and last being sets of normal CS+ trials. During the

test block animals experienced 40 test trials consisting of presentation of the CS followed by a 2

s delay and a 2 s bilateral stimulation of the dopamine cell bodies with no US (Figure 4A, top).

During these trials, the mice received a pulse of dopamine in lieu of the actual reward. The

control group (YFP$^+$ mice) extinguished their conditioned responding during the test block as

expected due to omission of the reward (Figure 4A, bottom), whereas ChrimsonR$^+$ mice

continued to perform the anticipatory licking even in the absence of the drop of milk (Figure

4B). Again we quantified performance in each block of trials and found that during the test

block the ChrimsonR[+] group have significantly higher level of performance than the YFP[+] group (Figure 4C).

Stimulation of dopamine projections in the lateral striatum had no significant effect

The VTA/SNc sends dense projections into the striatum [84]. Many studies that have found dopaminergic signaling in the striatum aimed to observe the activity of dopamine axons or to measure dopamine levels rather than to manipulate striatal dopamine [20], [23], [118], [119]. One study has reported effects on locomotion following stimulation of the dopamine axons in the striatum [115]. We attempted to stimulate striatal dopamine projection activity by expressing ChrimsonR in the VTA/SNc dopamine neurons and by implanting bilateral optical fibers in the lateral striatum (Figure 5A). After allowing adequate time for opsin expression to reach the dopamine axons in the striatum (Figure 5B), we performed the same effective extinction test as with the ChrimsonR[+] group that had VTA/SNc fibers. During the middle block of trials, mice experienced the CS paired with a 2 s continuous laser pulse instead of the US. However, with the ChrimsonR[+] group with striatal fibers, the anticipatory licking behavior was not maintained by the laser, as it decreased similarly to the YFP[+] control group (Figure 5C). Stimulation of the dopamine axons in the lateral striatum did not appear to have a reinforcing affect like stimulating the dopamine neurons. Stimulation of the dopamine axons did not appear to elicit any movement initiation in the form of licking either.

3.4 Discussion

To date there is much evidence supporting reward prediction error as a mechanism used in associative learning and supporting dopamine as the neural substrate of the RPE framework. Schultz has shown that dopamine neurons are active during Pavlovian conditioning

[19] and that associative learning suffers without dopamine [22], [23], [121]. Most of the previous studies showing a dependence on dopamine have been correlative and based on large-scale, long-term effects of techniques, such as lesions, pharmacological manipulations, and electrical stimulation. More recently optogenetic perturbations of dopamine have shown that dopamine stimulation is sufficient to establish conditioned place preference [21] and that dopamine inhibition in rats is sufficient to mimic negative RPE [122]. There is also a growing body of evidence supporting the role of dopamine in motor control [112]–[117]. However, the role of both CS- and US-related phasic dopamine responses remains untested, as does the specific time dependence of this signaling. Elucidating the roles of different dopamine transients could lead to better understanding of how dopamine functions as an RPE signal, motor control signal, or both. Confirming the timing of the reward-related dopaminergic response could help identify potential brain circuits involved in the RPE.

This study used both excitatory and inhibitory optogenetic manipulations to bidirectionally modulate dopamine neuron activity during a Pavlovian conditioning task. We were able to show that the phasic dopamine response to the US is both necessary and sufficient to maintain the CS-US association. By controlling the precise timing of dopamine manipulation with respect to the reward, we were able to show that dopaminergic signaling is most effective for the first 500 ms following the US. Previous studies have provided both correlative and causative evidence that dopamine functions as a neural substrate for RPE [19], [21], [121]–[123]. There is evidence that the phasic dopamine responses to the CS and the US are used as readouts of expected and actual outcomes, respectively, and that discrepancies between the two lead to learning. These studies are consistent with our findings that modulating reward-related dopamine can alter the stimulus-reward association and lead to changes in conditioned

responding. In addition, evidence that dopamine concentrations remained elevated following reward delivery for several hundred milliseconds has been shown [124], [125]. This is also consistent with our finding that the first 500 ms following reward delivery are the most important for dopamine signaling.

Existing literature has not yet determined a specific role for the CS-related dopamine transients that were famously discovered in primates by Schultz et al. in 1997 [19], and supported in rodent species as well [20], [118], [119]. According to RPE, one might hypothesize that manipulations of the CS dopamine response could alter the perceived expected outcome and, thus, affect learning. However, in our study, inhibition of the CS dopamine signal ostensibly had no effect on learning or conditioned responding. A decrease in expected outcome coupled with the normal actual outcome might be surprising to the animal and increase conditioned responding. One possibility is that our inhibition was not strong enough to shunt the phasic CS dopamine response. Since the US inhibition has such a large and statistically significant effect on anticipatory licking it seems unlikely that our optical stimulation is not effective. Alternatively, it has been shown that the CS dopamine axon response does not develop until after at least a week of Pavlovian conditioning [118], [119]. The behavioral test with CS inhibition took place after the mice had experienced three to nine days of conditioning. It is possible the manipulation had no effect because the CS dopamine transient had not fully developed yet. Along these lines, it might be that the role of the CS dopamine signaling is not used for maintaining the learned association but only forming new ones, as we performed optogenetic manipulations only on trained mice that had reached a high level of performance. Flagel et al. [23] performed pharmacological manipulations of dopamine and suggested that the CS dopamine

response was important for a type of associative learning involving sign-tracking, where animals develop a reinforcing relationship to the CS.

Based on recent evidence correlating dopaminergic signaling with movement kinematics [113]–[116], one might hypothesize that inhibition of dopamine neurons during the Pavlovian task might impair the licking behavior. While we did observe a disruption of the anticipatory licking during the 6 s laser test, we believe the effect to be related to reward-learning rather than motor function for two reasons. First, we detected changes only in the anticipatory licking; the consummatory licking was not altered nor delayed. Second, the behavioral effect is reproduced during the 2 s post-US test, while the 4 s pre-US test had no effect. It has been shown that stimulation and inhibition of the dopamine neurons in the SNc cause and prevent movement initiation, respectively [116], [117]. It is possible that we are not seeing a change in movement because our optical fibers were targeting the VTA/SNc, as opposed to targeting just the SNc. However, it is likely that the SNc is receiving adequate light stimulation due to scattering by the brain tissue. Alternatively, in this work we are measuring movement in head-fixed mice in the form of licking behavior. The discrepancy may be a consequence of measuring different movement modalities, as the previous studies were measuring locomotion and lever pressing.

Aside from VTA/SNc dopamine neuron recordings, many studies that find similar patterns of dopamine response have done so by measuring dopamine levels at a projection site. Typically, dopaminergic signaling is measured in the striatum, due to the magnitude of dopaminergic innervation found in the striatum [84] via fiber photometry [119] or fast scan cyclic voltammetry [20]. Our study found no significant behavioral effects when stimulating the axonal projections of the VTA/SNc dopamine neurons. Although there is plenty of opsin expression in the lateral striatum where we placed the optical fibers, most of the dopamine

measuring studies were focused on the medial ventral striatum, such as the nucleus accumbens, which has been implicated in reward related activity [23], [105], [115], [118]. Therefore, it is possible that, although there is much dopaminergic innervation all over the striatum, only specific areas or sub-structures experience dopamine-dependent plasticity or are involved in associative learning.

The field would benefit specifically from two aspects of this study being explored further: the CS-dopamine manipulations and the dopamine projection manipulations. The development of a CS-related dopamine transient, both neuron activity as well as striatal dopamine levels, should be studied in head-fixed mice performing a Pavlovian task like the one used in our study. Additionally, more exploration of areas of the striatum involved in dopamine-dependent plasticity would advance this work. There are multiple studies that suggest the nucleus accumbens area might be the most fruitful. Both of these would benefit the study and understanding of dopamine's role in RPE and the relevant circuitry involved.

In this study we used optogenetics to bidirectionally modulate dopamine activity with high temporal resolution during a Pavlovian conditioning task. This work provides strong causal evidence that phasic dopamine responses to the US are important for associative learning. The increased temporal precision provided by optogenetic techniques allowed us to provide behavioral evidence that the US dopaminergic signal is most effective for several hundred milliseconds.

3.5 Figures
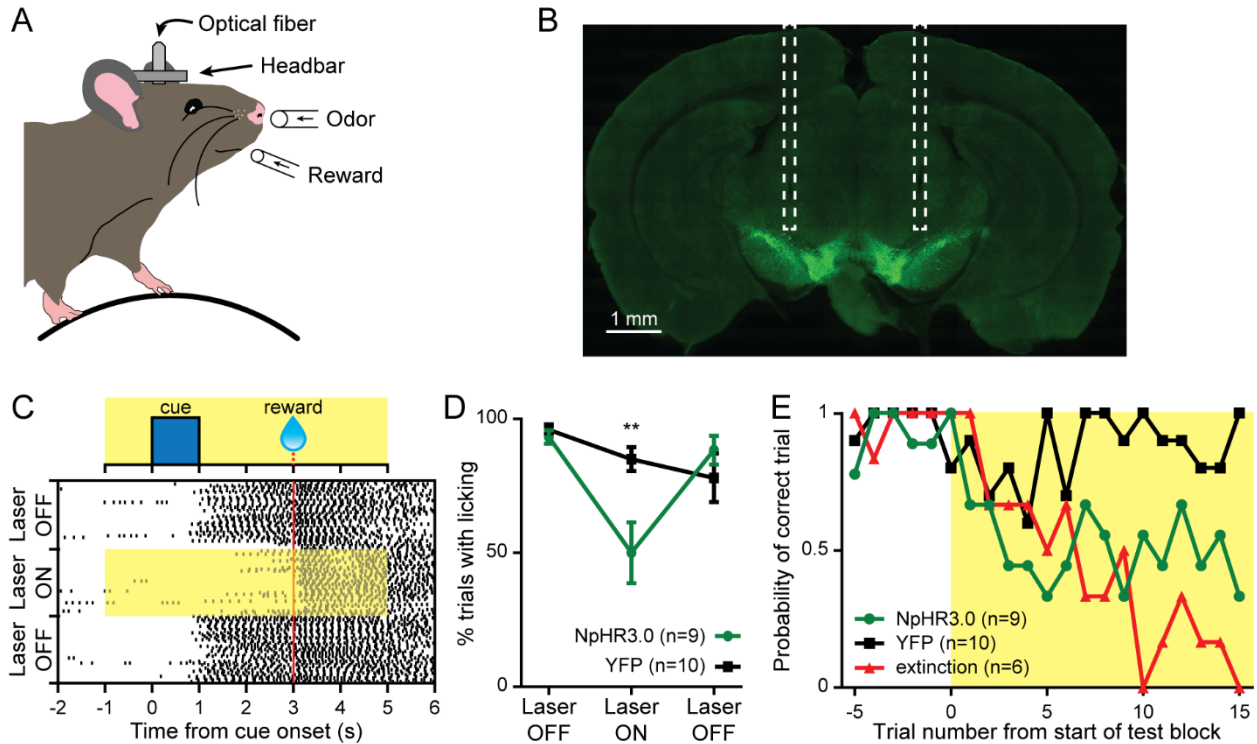
Figure 1: Inhibition of VTA/SNc dopamine neurons during Pavlovian conditioning task mimics extinction

A. Schematic of head-fixed mouse with optical fiber implant on behavioral testing rig. The animal receives a 1 s odor cue (CS) delivered in front of the nose that are predictive of a sweetened condensed milk reward (US).

B. Confocal microscope image of opsin expression and optical fiber placement (white dashed rectangles) in the ventral tegmental area and substantia nigra pars compacta (VTA/SNc). The brain was coronally sectioned at 100 μm and immunostained for the eYFP reporter on the opsin.

C. Top: diagram of Laser ON block trial, 1 s odor cue followed by reward delivery 3 s from cue onset, with 6 s continuous laser pulse beginning 1 s prior to CS onset. Bottom: lick raster

plot from 6 s laser test day for one NpHR3.0$^+$ mouse. The first 40 trials are shown in the bottom Laser OFF block, 40 Laser ON trials are in the middle, highlighted by the yellow bar, and the final 40 Laser OFF trials are at the top. Black tick marks represent licks and the red vertical line indicates US delivery.

D. Performance was independently calculated during each block of 40 trials as the fraction of trials where the mouse initiated licking prior to reward delivery (0-3 s from cue onset). There was a significant effect of block type and a significant interaction of group and block (n = 9 NpHR3.0$^+$ and 10 YFP$^+$ animals, two-way repeated measures (RM) ANOVA, block effect: $F_{2,34}$ = 13.03, p < 0.0001; group-block interaction: $F_{2,34}$ = 9.549, p = 0.0005). Post hoc multiple comparisons analysis revealed a significant reduction in NpHR3.0$^+$ group performance during the Laser ON block (p = 0.0015).

E. Probability of a mouse issuing anticipatory licks during the last 5 trials of the first Laser OFF block and the first 15 trials of the Laser ON block. NpHR3.0$^+$ animals (n = 9) in green circles, YFP$^+$ animals (n = 10) in black squares, and a group of animals who experienced omission of reward (extinction) during the middle block instead of a laser pulse (n = 6).
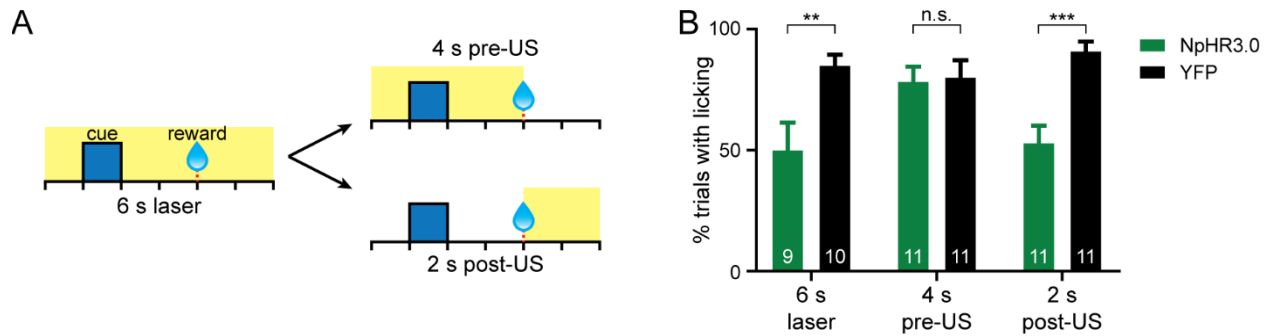
Figure 2: Inhibiting US, but not CS dopamine transient, reduces conditioned responding

A. Diagram of test trials during Laser ON block of subsequent behavior test days. The original test included a 6 s continuous laser pulse beginning 1 s prior to CS onset and ending 2 s after reward delivery. A second test day included a 4 s continuous laser pulse beginning 1 s prior to CS onset and ending prior to US (4 s pre-US). Another test day consisted of a 2 s continuous laser pulse beginning at the time of the US (2 s post-US).

B. Performance during the Laser ON block for each test and group. There was a significant effect of group and a significant interaction of group and block (6 s laser: n = 9 NpHR3.0[+] and 10 YFP[+] animals, 4 s pre-US and 2 s post-US: n = 11 NpHR3.0[+] and 11 YFP[+] animals, two-way ANOVA, group effect: $F_{1,57}$ = 19.61, p < 0.0001; group-block interaction: $F_{2,57}$ = 4.466, p = 0.0158). Post hoc multiple comparisons analysis revealed a significant reduction in NpHR3.0[+] group performance during the Laser ON block for 6 s laser (p = 0.0034) and 2 s post-US (p = 0.0005), but no significant difference for 4 s pre-US (p = 0.9977).

Figure 3: US dopamine signaling necessary for several hundreds of milliseconds

A. Top: diagram of Laser ON block trial with 2 s continuous laser pulse beginning at time of US (0 s delay). Bottom: Performance during first Laser OFF, Laser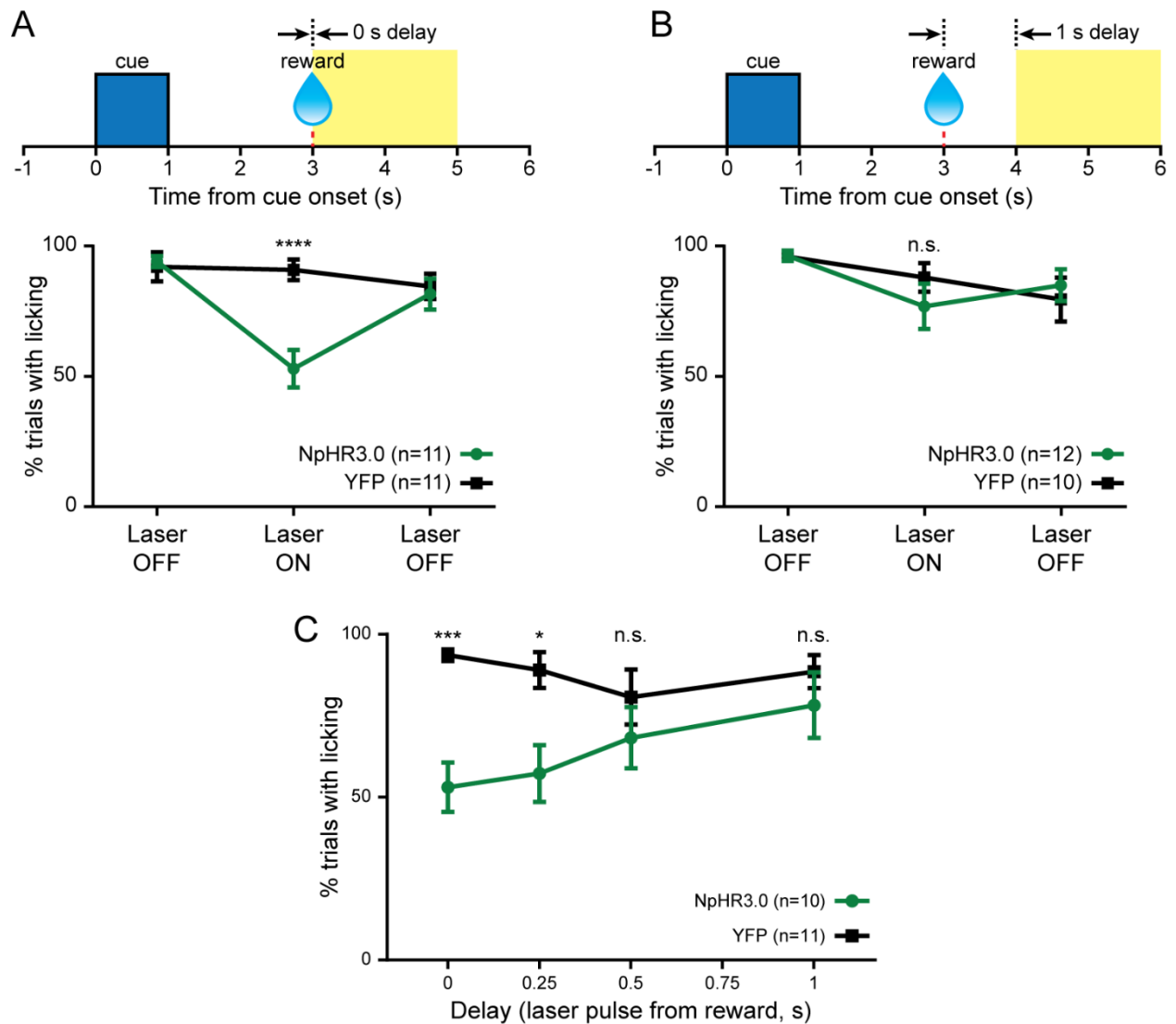 ON, and final Laser OFF block for NpHR3.0[+] and YFP[+] groups. There was a significant effect of block type and a significant interaction of group and block (n = 11 NpHR3.0[+] and 11 YFP[+] animals, two-way RM ANOVA, block effect: $F_{2,40} = 22.18$, p < 0.0001; group-block interaction: $F_{2,40} = 23.56$,

$p < 0.0001$). Post hoc multiple comparisons analysis revealed a significant reduction in NpHR3.0$^+$ group performance during the Laser ON block ($p < 0.0001$).

B. Top: diagram of Laser ON block trial with 2 s continuous laser pulse beginning 1 s after US delivery (1 s delay). Bottom: Performance during first Laser OFF, Laser ON, and final Laser OFF block for NpHR3.0$^+$ and YFP$^+$ groups. There was a significant effect of block type, but not of group or interaction (n = 12 NpHR3.0$^+$ and 10 YFP$^+$ animals, two-way RM ANOVA, block effect: $F_{2,40} = 9.287$, $p = 0.0005$). Post hoc multiple comparisons analysis did not reveal a significant change in NpHR3.0$^+$ group performance during the Laser ON block ($p = 0.5023$).

C. Performance during the Laser ON block for a series of tests where the 2 s laser pulse was incrementally delayed from US delivery. There was a significant effect of group and interaction of group and delay, but no significant effect of delay (n = 10 NpHR3.0$^+$ and 11 YFP$^+$ animals, two-way RM ANOVA, group effect: $F_{1,19} = 8.814$, $p = 0.0079$; group-delay interaction: $F_{3,57} = 3.664$, $p = 0.0174$). Post hoc multiple comparisons analysis revealed a significant reduction in NpHR3.0$^+$ group performance during the Laser ON block for 0 s delay ($p = 0.0009$) and 0.25 s delay ($p = 0.0126$), but no significant difference for 0.5 s delay ($p = 0.6566$) nor 1 s delay ($p = 0.7934$).
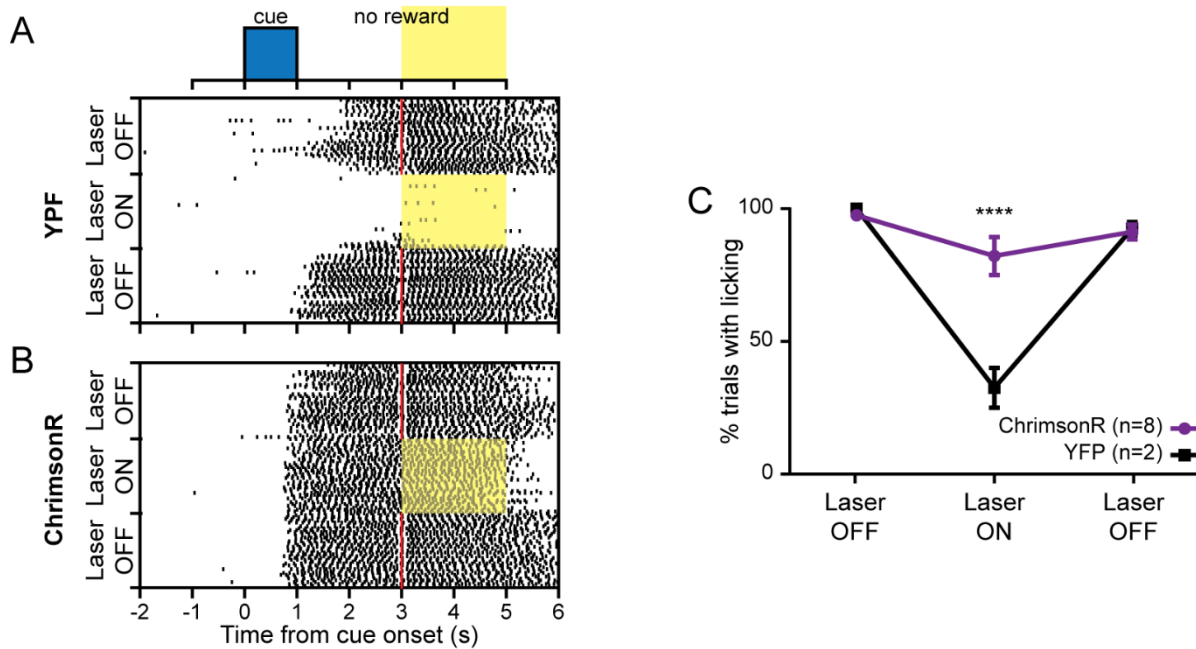
Figure 4: US dopamine signaling sufficient to maintain conditioned responding

A. Top: diagram of Laser ON block trial which consisted of CS presentation followed by no reward and a 2 s continuous laser pulse at the time of omitted reward. Bottom: lick raster plot from 2 s laser during extinction test for one YPF[+] mouse. The first 40 trials are shown in the bottom Laser OFF block, 40 Laser ON extinction trials are in the middle highlighted by the yellow bar, and the final 40 Laser OFF trials are at the top. Black tick marks represent licks and the red vertical line indicates US delivery.

B. Lick raster plot from 2 s laser during extinction test for one ChrimsonR[+] mouse.

C. Performance during the three blocks for ChrimsonR[+] and YFP[+] groups. There was a significant block and group effect and interaction (n = 8 ChrimsonR[+] and 2 YFP[+] animals, two-way RM ANOVA, block effect: $F_{2,16} = 22.03$, $p < 0.0001$; group effect: $F_{1,8} = 7.402$, $p = 0.0262$; block-group interaction: $F_{2,16} = 9.916$, $p = 0.0016$). Post hoc multiple comparisons analysis revealed a significant increase in ChrimsonR[+] group performance compared to YFP[+] performance during the Laser ON extinction block ($p < 0.0001$).

93
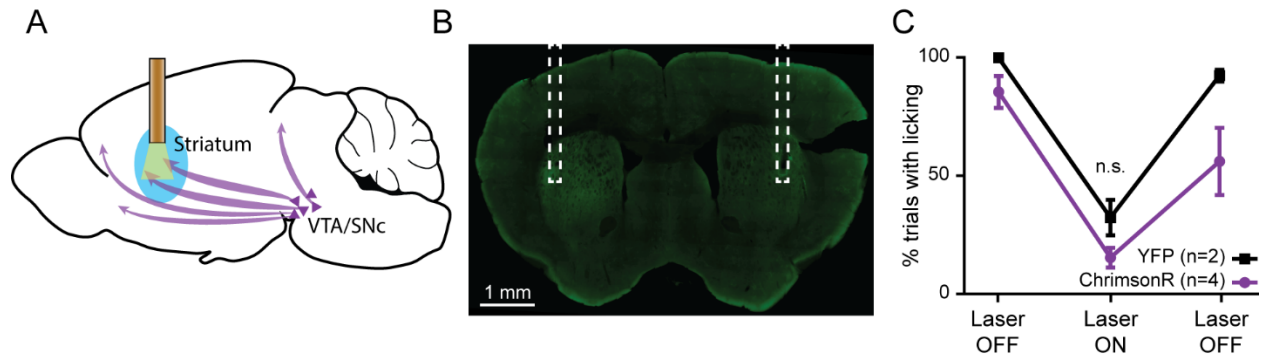
Figure 5: Stimulation of dopaminergic projections in lateral striatum has no effect

A. Schematic of VTA/SNc viral infusions combined with optical fibers implanted in the striatum for projection stimulation.

B. Confocal microscope image of opsin expression in dopamine axons and optical fiber placement (white dashed rectangles) in the lateral striatum. The brain was coronally sectioned at 100 µm and immunostained for the eYFP reporter on the opsin.

C. Mice with terminal fibers experienced the same 2 s laser with extinction test as described in Figure 4. Performance during the three blocks for ChrimsonR[+] and YFP[+] groups. There was a significant block effect, but no significant group effect nor interaction (n = 4 ChrimsonR[+] and 2 YFP[+] animals, two-way RM ANOVA, block effect: $F_{2,8} = 40.43$, $p < 0.0001$). Post hoc multiple comparisons analysis did not reveal a significant difference between ChrimsonR[+] and YFP[+] group performance during the Laser ON extinction block (p = 0.5997).

CONCLUSION

Summary of Research Contributions

The basal ganglia are an important set of structures that exist in all vertebrates [24]. Decades of studying these nuclei and other connected structures have identified a host of processes that involve basal ganglia circuitry such as motor control, action selection, associative learning, timing, memory, and arousal. Despite the accumulation of knowledge regarding the structure and function of the basal ganglia, there is still much to learn about this important network of nuclei. This work presents our attempt to answer some of these remaining questions by investigating basal ganglia function in an associative learning task.

In chapter one we described the development and validation of a three-dimensional silicon microprobe device and accompanied hardware and software that allowed simultaneous data acquisition from 1,024 electrodes distributed in four distal brain regions. We showed that during a Pavlovian conditioning paradigm task-evoked neuron population activity was similar between the rewarded and unrewarded cue at an interregional level. In addition, we identified significant signal and resting state correlations between neurons from the same as well as different regions. Recordings of this scale in awake, behaving mice can reveal multiregional circuit dynamics and can potentially answer long-standing questions concerning basal ganglia function.

In chapter two we described the characterization and implementation of an optogenetic photo-tagging protocol for use with our silicon microprobes with attached optical fibers. We studied Pavlovian task-evoked activity in the direct and indirect pathways of the basal ganglia by performing electrophysiological recordings of striatal neurons and using a light stimulation to identify the D1 and D2 dopamine receptor expressing neuron populations. We showed that D1

and D2 cells showed increased firing rates during initiation of the licking response to the reward-predicting odor stimulus. We also observed a significantly increased reward response in the D1 population compared to the D2 population. Chapter two demonstrates that optogenetic identification of neuronal subtypes in the striatum can further elucidate the role of these two pathways in the basal ganglia.

Chapter three presented a set of experiments involving optogenetic manipulations of dopamine signaling during performance of a learned Pavlovian association task. We showed that dopamine signaling at the time of reward is both necessary and sufficient to maintain the learned association between a conditioned stimulus and a reward. A temporal dissection of the reward-evoked dopamine response provided evidence that the timing of dopamine response to the reward is crucial for maintaining the association.

This work stands as a testament to the advantages offered by utilizing innovative techniques. Large-scale electrophysiological devices increase the number of regions that can be recorded as well as the number of neurons. Tools that allow targeting and modulation of genetically-defined neuronal subtypes give us the ability to perform circuit dissections and observe resulting neural activity and potential behavioral consequences that result. Together the findings presented in this dissertation give a clearer picture of basal ganglia function in a Pavlovian conditioning task and stand as evidence that basal ganglia nuclei appear to be involved in stimulus processing, motivated motor control, and reward learning.

Future Work

Chapter one discussed the development and application of a three-dimensional microprobe device for studying neural dynamics of basal ganglia nuclei in behaving mice. A natural extension of this work would be to use this device to study basal ganglia function (or

dysfunction) in mouse models of basal ganglia disorders such as Parkinson's disease and Huntington's disease. The method we established to build the devices allows the experimenter to customize the configuration of new devices to target different sets of brain regions. A new device could be built to study neural activity dynamics and circuit function in nearly any combination of structures in healthy mice or disease models.

Chapter two detailed our characterization of an optogenetic tagging protocol and subsequent study of the direct and indirect pathways. In this work we analyzed neural activity from approximately 80 positively identified neurons from each pathway. Building a three-dimensional microprobe that consists of two layers surrounding the two attached optical fibers would increase the total number of cells recorded and, likely, the number of positively identified cells, as well. The analysis of neural dynamics in the two pathways would be strengthened by including more identified cells. In addition, direct and indirect pathway function in movement suppression could be examined if the task contained a new trial type that required mice to withhold licking (e.g. an odor cue that is rewarded only if mice do not lick in anticipation).

Chapter three discussed the behavioral effects of dopamine manipulations. A substantial amount of evidence points to the striatum as being a site of dopamine-dependent plasticity. We did not observe a behavioral effect due to dopamine axon stimulation in the lateral striatum, however the ventral striatum/nucleus accumbens is another reasonable area to investigate because it is often linked to reward processing. We were intrigued that the dopamine manipulations performed did not appear to alter any measured motor functions, since others have reported changes in locomotion due to dopamine stimulation. It would be useful to repeat the experiments in mice placed on a treadmill and monitor the locomotion during task performance. In addition, these experiments could be repeated with the optical fibers implanted in a more

97

lateral position, closer to the substantia nigra pars compacta which is thought to be more involved in movement than the ventral tegmental area.

Even after more than a century of research dedicated to elucidating the structure and function of the basal ganglia, many questions persist. Future exploration of the findings discussed in this dissertation, whether in the form of the experiments suggested above or any number of alternatives, will benefit research in the basal ganglia field. Advanced understanding of basal ganglia circuitry in both health and disease will promote improvements in existing therapies and development of new treatments or even cures for disorders affecting the basal ganglia.

REFERENCES

[1]   J. L. Shobe, L. D. Claar, S. Parhami, K. I. Bakhurin, and S. C. Masmanidis, "Brain activity mapping at multiple scales with silicon microprobes containing 1024 electrodes," *J. Neurophysiol.*, vol. 114, pp. 2043–2052, 2015.

[2]   A. M. Graybiel, *The Basal Ganglia*, vol. 10, no. 14. 2000.

[3]   A. Parent, "The History of the Basal Ganglia: The Contribution of Karl Friedrich Burdach," *Neurosci. Med.*, vol. 3, no. 4, pp. 374–379, 2012.

[4]   N. YANAGISAWA, "Historical Review of Research on Functions of Basal Ganglia," *Eur. Neurol.*, vol. 36, no. supple 1, pp. 2–8, 1996.

[5]   R. L. Albin, A. B. Young, and J. B. Penney, "The functional anatomy of basal ganglia disorders," *Trends Neurosci.*, vol. 12, no. 10, pp. 366–375, 1989.

[6]   G. E. Alexander and M. D. Crutcher, "Functional architecture of basal ganglia circuits: neural substrates of parallel processing," *Trends Neurosci.*, vol. 13, no. 7, pp. 266–271, 1990.

[7]   M. R. DeLong, "Primate models of movement disorders of basal ganglia origin," *Trends Neurosci.*, vol. 13, no. 7, pp. 281–285, 1990.

[8]   A. Reiner, R. L. Albin, K. D. Anderson, C. J. D'Amato, J. B. Penney, and A. B. Young, "Differential loss of striatal projection neurons in Huntington disease.," *Proc. Natl. Acad. Sci. U. S. A.*, vol. 85, no. 15, pp. 5733–7, Aug. 1988.

[9]   A. V. Kravitz *et al.*, "Regulation of parkinsonian motor behaviours by optogenetic control of basal ganglia circuitry," *Nature*, vol. 466, no. 7306, pp. 622–626, 2010.

[10]   O. Hikosaka *et al.*, "Role of the basal ganglia in the control of purposive saccadic eye movements.," *Physiol. Rev.*, vol. 80, no. 3, pp. 953–78, 2000.

[11]   J. W. Mink, "The basal ganglia and involuntary movements: Impaired inhibition of competing motor patterns," *Archives of Neurology*, vol. 60, no. 10. pp. 1365–1368, 2003.

[12]   G. Cui *et al.*, "Concurrent activation of striatal direct and indirect pathways during action initiation," *Nature*, vol. 494, no. 7436, pp. 238–242, 2013.

[13]   X. Jin, F. Tecuapetla, and R. M. Costa, "Basal ganglia subcircuits distinctively encode the parsing and concatenation of action sequences," *Nat. Neurosci.*, vol. 17, no. 3, pp. 423–430, 2014.

[14]   B. W. Balleine, M. R. Delgado, and O. Hikosaka, "The Role of the Dorsal Striatum in Reward and Decision-Making," *J. Neurosci.*, vol. 27, no. 31, pp. 8161–8165, 2007.

[15]   C. R. Gerfen and D. J. Surmeier, "Modulation of Striatal Projection Systems by Dopamine," *Annu. Rev. Neurosci.*, vol. 34, pp. 441–466, 2011.

[16]   K. Lee *et al.*, "Parvalbumin Interneurons Modulate Striatal Output and Enhance Performance during Associative Learning," *Neuron*, vol. 93, no. 6, p. 1451–1463.e4, 2017.

[17]   A. C. Kreitzer and R. C. Malenka, "Striatal Plasticity and Basal Ganglia Circuit Function," *Neuron*, vol. 60, no. 4, pp. 543–554, 2008.

[18]   J. P. Bolam, J. J. Hanley, P. A. C. Booth, and M. D. Bevan, "Synaptic organisation of the basal ganglia," *Journal of Anatomy*, vol. 196, no. 4. pp. 527–542, 2000.

[19]   W. Schultz, P. Dayan, and P. R. Montague, "A Neural Substrate of Prediction and

Reward.," *Science (80-.).*, vol. 275, no. 5306, pp. 1593–1599, 1997.

[20] A. A. Hamid *et al.*, "Mesolimbic dopamine signals the value of work," *Nat. Neurosci.*, vol. 19, no. 1, pp. 117–126, 2015.

[21] H.-C. Tsai *et al.*, "Phasic Firing in Dopaminergic Neurons Is Sufficient for Behavioral Conditioning," *Science (80-.).*, vol. 324, no. May, pp. 1080–1084, 2009.

[22] R. D. Palmiter, "Dopamine signaling in the dorsal striatum is essential for motivated behaviors: Lessons from dopamine-deficient mice," *Ann. N. Y. Acad. Sci.*, vol. 1129, pp. 35–46, 2008.

[23] S. B. Flagel *et al.*, "A selective role for dopamine in stimulus-reward learning," *Nature*, vol. 469, no. 7328, pp. 53–59, 2011.

[24] P. Redgrave, T. J. Prescott, and K. Gurney, "The basal ganglia: A vertebrate solution to the selection problem?," *Neuroscience*, vol. 89, no. 4, pp. 1009–1023, 1999.

[25] K. I. Bakhurin, V. Mac, P. Golshani, and S. C. Masmanidis, "Temporal correlations among functionally specialized striatal neural ensembles in reward-conditioned mice," *J. Neurophysiol.*, vol. 115, no. 3, pp. 1521–1532, 2016.

[26] C. Gerfen *et al.*, "D1 and D2 dopamine receptor-regulated gene expression of striatonigral and striatopallidal neurons," *Science (80-.).*, vol. 250, no. 4986, pp. 1429–1432, 1990.

[27] D. Kvitsiani, S. Ranade, B. Hangya, H. Taniguchi, J. Z. Huang, and A. Kepecs, "Distinct behavioural and network correlates of two interneuron types in prefrontal cortex," *Nature*, vol. 498, no. 7454, pp. 363–366, 2013.

[28] H. Planert, T. K. Berger, and G. Silberberg, "Membrane Properties of Striatal Direct and

Indirect Pathway Neurons in Mouse and Rat Slices and Their Modulation by Dopamine," *PLoS One*, vol. 8, no. 3, pp. 1–14, 2013.

[29] G. Buzsáki, "Large-scale recording of neuronal ensembles," *Nature Neuroscience*, vol. 7, no. 5. pp. 446–451, 2004.

[30] R. Paz, E. P. Bauer, and D. Paré, "Measuring correlations and interactions among four simultaneously recorded brain regions during learning.," *J. Neurophysiol.*, vol. 101, no. 5, pp. 2507–15, 2009.

[31] I. H. Stevenson and K. P. Kording, "How advances in neural recording affect data analysis," in *Nature Neuroscience*, 2011, vol. 14, no. 2, pp. 139–142.

[32] D. A. Schwarz *et al.*, "Chronic, wireless recordings of large-scale brain activity in freely moving rhesus monkeys," *Nat. Methods*, vol. 11, no. 6, pp. 670–676, 2014.

[33] A. Berenyi *et al.*, "Large-scale, high-density (up to 512 channels) recording of local circuits in behaving animals," *J. Neurophysiol.*, vol. 111, no. 5, pp. 1132–1149, 2014.

[34] T. J. Blanche, "Polytrodes: High-Density Silicon Electrode Arrays for Large-Scale Multiunit Recording," *J. Neurophysiol.*, vol. 93, no. 5, pp. 2987–3000, 2005.

[35] J. Csicsvari, D. A. Henze, B. Jamieson, K. D. Harris, A. Sirota, and K. D. Wise, "Massively Parallel Recording of Unit and Local Field Potentials With Silicon- Based Electrodes ´," *J. Neurophysiol.*, vol. 90, no. 2, pp. 1314–1323, 2003.

[36] K. D. Wise, A. M. Sodagar, Y. Yao, M. N. Gulari, G. E. Perlin, and K. Najafi, "Microelectrodes, microelectronics, and implantable neural microsystems," *Proc. IEEE*, vol. 96, no. 7, pp. 1184–1202, 2008.

[37] J. Lecoq *et al.*, "Visualizing mammalian brain area interactions by dual-axis two-photon calcium imaging," *Nat. Neurosci.*, vol. 17, no. 12, pp. 1825–1829, 2014.

[38] D. A. Dombeck, A. N. Khabbaz, F. Collman, T. L. Adelman, and D. W. Tank, "Imaging Large-Scale Neural Activity with Cellular Resolution in Awake, Mobile Mice," *Neuron*, vol. 56, no. 1, pp. 43–57, 2007.

[39] D. A. Dombeck and M. B. Reiser, "Real neuroscience in virtual worlds," *Current Opinion in Neurobiology*, vol. 22, no. 1. pp. 3–10, 2012.

[40] J. Du, T. J. Blanche, R. R. Harrison, H. A. Lester, and S. C. Masmanidis, "Multiplexed, high density electrophysiology with nanofabricated neural probes," *PLoS One*, vol. 6, no. 10, 2011.

[41] C. Gold, D. A. Henze, and C. Koch, "Using extracellular action potential recordings to constrain compartmental models," *J. Comput. Neurosci.*, vol. 23, no. 1, pp. 39–58, 2007.

[42] D. a Henze, Z. Borhegyi, J. Csicsvari, a Mamiya, K. D. Harris, and G. Buzsáki, "Intracellular features predicted by extracellular recordings in the hippocampus in vivo.," *J. Neurophysiol.*, vol. 84, no. 1, pp. 390–400, 2000.

[43] G. Alexander, "Parallel Organization of Functionally Segregated Circuits Linking Basal Ganglia and Cortex," *Annu. Rev. Neurosci.*, vol. 9, no. 1, pp. 357–381, 1986.

[44] R. R. Harrison and C. Charles, "A low-power low-noise CMOS amplifier for neural recording applications," *IEEE J. Solid-State Circuits*, vol. 38, no. 6, pp. 958–965, 2003.

[45] C. M. Niell and M. P. Stryker, "Modulation of Visual Responses by Behavioral State in Mouse Visual Cortex," *Neuron*, vol. 65, no. 4, pp. 472–479, 2010.

[46] N. S. Narayanan and M. Laubach, "Methods for studying functional interactions among neuronal populations," *Methods Mol Biol*, vol. 489, pp. 135–165, 2009.

[47] W. Schultz, "Multiple reward signals in the brain," *Nat. Rev. Neurosci.*, vol. 1, no. 3, pp. 199–207, 2000.

[48] P. Bartho, "Characterization of Neocortical Principal Cells and Interneurons by Network Interactions and Extracellular Features," *J. Neurophysiol.*, vol. 92, no. 1, pp. 600–608, 2004.

[49] N. Mallet, "Feedforward Inhibition of Projection Neurons by Fast-Spiking GABA Interneurons in the Rat Striatum In Vivo," *J. Neurosci.*, vol. 25, no. 15, pp. 3857–3869, 2005.

[50] D. a McCormick, B. W. Connors, J. W. Lighthall, and D. a Prince, "Comparative electrophysiology of pyramidal and sparsely spiny stellate neurons of the neocortex.," *J. Neurophysiol.*, vol. 54, no. 4, pp. 782–806, 1985.

[51] J. Y. Cohen, S. Haesler, L. Vong, B. B. Lowell, and N. Uchida, "Neuron-type-specific signals for reward and punishment in the ventral tegmental area," *Nature*, vol. 482, no. 7383, pp. 85–88, 2012.

[52] J. P. Cunningham and B. M. Yu, "Dimensionality reduction for large-scale neural recordings," *Nature Neuroscience*, vol. 17, no. 11. pp. 1500–1509, 2014.

[53] A. Adler, S. Katabi, I. Finkes, Z. Israel, Y. Prut, and H. Bergman, "Temporal Convergence of Dynamic Cell Assemblies in the Striato-Pallidal Network," *J. Neurosci.*, vol. 32, no. 7, pp. 2473–2484, 2012.

[54] D. A. Dombeck, M. S. Graziano, and D. W. Tank, "Functional Clustering of Neurons in Motor Cortex Determined by Cellular Resolution Imaging in Awake Behaving Mice," *J. Neurosci.*, vol. 29, no. 44, pp. 13751–13760, 2009.

[55] A. Ponzi and J. Wickens, "Input Dependent Variability in a Model of the Striatal Medium Spiny Neuron Network," in *Advances in Cognitive Neurodynamics (III)*, 2013, pp. 139–145.

[56] M. A. Smith and A. Kohn, "Spatial and temporal scales of neuronal correlation in primary visual cortex.," *J. Neurosci.*, vol. 28, no. 48, pp. 12591–603, 2008.

[57] H. Ko, S. B. Hofer, B. Pichler, K. A. Buchanan, P. J. Sjöström, and T. D. Mrsic-Flogel, "Functional specificity of local synaptic connections in neocortical networks," *Nature*, vol. 473, no. 7345, pp. 87–91, 2011.

[58] D. A. McCormick, "Spontaneous Activity: Signal or Noise?," *Science (80-.).*, vol. 285, no. 5427, pp. 541–543, 1999.

[59] D. L. Ringach, "Spontaneous and driven cortical activity: implications for computation," *Current Opinion in Neurobiology*, vol. 19, no. 4. pp. 439–444, 2009.

[60] W. E. Skaggs and B. L. McNaughton, "Replay of Neuronal Firing Sequences in Rat Hippocampus During Sleep Following Spatial Experience," *Science (80-.).*, vol. 271, no. 5257, pp. 1870–1873, 1996.

[61] E. Bullmore and O. Sporns, "Complex brain networks: graph theoretical analysis of structural and functional systems," *Nat. Publ. Gr.*, vol. 10, no. 3, pp. 186–198, 2009.

[62] J. L. Vincent *et al.*, "Intrinsic functional architecture in the anaesthetized monkey brain,"

Nature, vol. 447, no. 7140, pp. 83–86, 2007.

[63]   C. M. Gray and W. Singer, "Stimulus-specific neuronal oscillations in orientation columns of cat visual cortex.," *Proc. Natl. Acad. Sci.*, vol. 86, no. 5, pp. 1698–1702, 1989.

[64]   J. D. Berke, M. Okatan, J. Skurski, and H. B. Eichenbaum, "Oscillatory entrainment of striatal neurons in freely moving rats," *Neuron*, vol. 43, no. 6, pp. 883–896, 2004.

[65]   R. Courtemanche, N. Fujii, and A. M. Graybiel, "Synchronous, focally modulated beta-band oscillations characterize local field potential activity in the striatum of awake behaving monkeys.," *J. Neurosci.*, vol. 23, no. 37, pp. 11741–11752, 2003.

[66]   G. Buzsáki, C. A. Anastassiou, and C. Koch, "The origin of extracellular fields and currents-EEG, ECoG, LFP and spikes," *Nature Reviews Neuroscience*, vol. 13, no. 6. pp. 407–420, 2012.

[67]   G. T. Einevoll, C. Kayser, N. K. Logothetis, and S. Panzeri, "Modelling and analysis of local field potentials for studying the function of cortical circuits," *Nature Reviews Neuroscience*, vol. 14, no. 11. pp. 770–785, 2013.

[68]   G. Buzsáki and E. W. Schomburg, "What does gamma coherence tell us about inter-regional neural communication?," *Nature Neuroscience*, vol. 18, no. 4. pp. 484–489, 2015.

[69]   G. Buzsáki and X.-J. Wang, "Mechanisms of Gamma Oscillations," *Annu. Rev. Neurosci.*, vol. 35, no. 1, pp. 203–225, 2012.

[70]   A. Nakhnikian, G. V. Rebec, L. M. Grasse, L. L. Dwiel, M. Shimono, and J. M. Beggs, "Behavior modulates effective connectivity between cortex and striatum," *PLoS One*, vol.

9, no. 3, 2014.

[71] C. C. H. Petersen, T. T. G. Hahn, M. Mehta, A. Grinvald, and B. Sakmann, "Interaction of sensory responses with spontaneous depolarization in layer 2/3 barrel cortex," *Proc. Natl. Acad. Sci.*, vol. 100, no. 23, pp. 13638–13643, 2003.

[72] M. Vinck, R. Batista-Brito, U. Knoblich, and J. A. Cardin, "Arousal and Locomotion Make Distinct Contributions to Cortical Activity Patterns and Visual Encoding," *Neuron*, vol. 86, no. 3, pp. 740–754, 2015.

[73] S. Fujisawa and G. Buzsáki, "A 4 Hz Oscillation Adaptively Synchronizes Prefrontal, VTA, and Hippocampal Activities," *Neuron*, vol. 72, no. 1, pp. 153–165, 2011.

[74] J. H. Siegle, G. J. Hale, J. P. Newman, and J. Voigts, "Neural ensemble communities: Open-source approaches to hardware for large-scale electrophysiology," *Current Opinion in Neurobiology*, vol. 32. pp. 53–59, 2015.

[75] N. Pak, J. H. Siegle, J. P. Kinney, D. J. Denman, T. J. Blanche, and E. S. Boyden, "Closed-loop, ultraprecise, automated craniotomies," *J. Neurophysiol.*, vol. 113, no. 10, pp. 3943–3953, 2015.

[76] A. C. Hoogerwerf and K. D. Wise, "A Three-Dimensional Microelectrode Array for Chronic Neural Recording," *IEEE Trans. Biomed. Eng.*, vol. 41, no. 12, pp. 1136–1146, 1994.

[77] M. W. Cole, D. S. Bassett, J. D. Power, T. S. Braver, and S. E. Petersen, "Intrinsic and task-evoked network architectures of the human brain," *Neuron*, vol. 83, no. 1, pp. 238–251, 2014.

[78]   W. Bair, E. Zohary, and W. T. Newsome, "Correlated firing in macaque visual area MT: time scales and relationship to behavior.," *J. Neurosci.*, vol. 21, no. 5, pp. 1676–97, 2001.

[79]   T. Komiyama *et al.*, "Learning-related fine-scale specificity imaged in motor cortex circuits of behaving mice.," *Nature*, vol. 464, no. 7292, pp. 1182–1186, 2010.

[80]   G. Deco and M. L. Kringelbach, "Great expectations: Using whole-brain computational connectomics for understanding neuropsychiatric disorders," *Neuron*, vol. 84, no. 5. pp. 892–905, 2014.

[81]   M. B. Ahrens *et al.*, "Brain-wide neuronal dynamics during motor adaptation in zebrafish," *Nature*, vol. 485, no. 7399, pp. 471–477, 2012.

[82]   A. H. Gittis and A. C. Kreitzer, "Striatal microcircuitry and movement disorders," *Trends Neurosci.*, vol. 35, no. 9, pp. 557–564, 2012.

[83]   G. A. Graveland and M. Difiglia, "The frequency and distribution of medium-sized neurons with indented nuclei in the primate and rodent neostriatum," *Brain Res.*, vol. 327, no. 1–2, pp. 307–311, 1985.

[84]   W. Schultz, "Predictive Reward Signal of Dopamine Neurons," *J. Neurophysiol.*, vol. 80, no. 1, pp. 1–27, 1998.

[85]   J. Bertran-Gonzalez *et al.*, "Opposing Patterns of Signaling Activation in Dopamine D1 and D2 Receptor-Expressing Striatal Neurons in Response to Cocaine and Haloperidol," *J. Neurosci.*, vol. 28, no. 22, pp. 5671–5685, 2008.

[86]   D. Gagnon *et al.*, "Striatal Neurons Expressing D1 and D2 Receptors are Morphologically Distinct and Differently Affected by Dopamine Denervation in Mice," *Sci. Rep.*, vol. 7, p.

41432, 2017.

[87]   S. Taverna, E. Ilijic, and D. J. Surmeier, "Recurrent Collateral Connections of Striatal
        Medium Spiny Neurons Are Disrupted in Models of Parkinson's Disease," *J. Neurosci.*,
        vol. 28, no. 21, pp. 5504–5512, 2008.

[88]   H. Planert, S. N. Szydlowski, J. J. J. Hjorth, S. Grillner, and G. Silberberg, "Dynamics of
        Synaptic Transmission between Fast-Spiking Interneurons and Striatal Projection Neurons
        of the Direct and Indirect Pathways," *J. Neurosci.*, vol. 30, no. 9, pp. 3499–3507, 2010.

[89]   A. H. Gittis, A. B. Nelson, M. T. Thwin, J. J. Palop, and A. C. Kreitzer, "Distinct Roles of
        GABAergic Interneurons in the Regulation of Striatal Output Pathways," *J. Neurosci.*,
        vol. 30, no. 6, pp. 2223–2234, 2010.

[90]   T. Koós and J. M. Tepper, "Inhibitory control of neostriatal projection neurons by
        GABAergic interneurons," *Nat. Neurosci.*, vol. 2, no. 5, pp. 467–472, 1999.

[91]   F. M. Zhou, C. J. Wilson, and J. A. Dani, "Cholinergic interneuron characteristics and
        nicotinic properties in the striatum," *J. Neurobiol.*, vol. 53, no. 4, pp. 590–605, 2002.

[92]   N. C. Klapoetke *et al.*, "Independent optical excitation of distinct neural populations.,"
        Nat. Methods, vol. 11, no. 3, pp. 338–46, 2014.

[93]   A. V. Kravitz, S. F. Owen, and A. C. Kreitzer, "Optogenetic identification of striatal
        projection neuron subtypes during in vivo recordings," *Brain Res.*, vol. 1511, pp. 21–32,
        2013.

[94]   A. Beyeler *et al.*, "Divergent Routing of Positive and Negative Information from the
        Amygdala during Memory Retrieval," *Neuron*, vol. 90, no. 2, pp. 348–361, 2016.

[95]   D. A. Burke, H. G. Rotstein, and V. A. Alvarez, "Striatal Local Circuitry: A New Framework for Lateral Inhibition," *Neuron*, vol. 96, no. 2, pp. 267–284, 2017.

[96]   T. S. Gertler, C. S. Chan, and D. J. Surmeier, "Dichotomous Anatomical Properties of Adult Striatal Medium Spiny Neurons," *J. Neurosci.*, vol. 28, no. 43, pp. 10814–10824, 2008.

[97]   F. Tecuapetla, S. Matias, G. P. Dugue, Z. F. Mainen, and R. M. Costa, "Balanced activity in basal ganglia projection pathways is critical for contraversive movements," *Nat. Commun.*, vol. 5, 2014.

[98]   G. Barbera *et al.*, "Spatially Compact Neural Clusters in the Dorsal Striatum Encode Locomotion Relevant Information," *Neuron*, vol. 92, no. 1, pp. 202–213, 2016.

[99]   F. Tecuapetla, X. Jin, S. Q. Lima, and R. M. Costa, "Complementary Contributions of Striatal Projection Pathways to Action Initiation and Execution," *Cell*, vol. 166, no. 3, pp. 703–715, 2016.

[100]   R. A. Wise, "Neurobiology of addiction," *Curr. Opin. Neurobiol.*, vol. 6, no. 2, pp. 243–251, 1996.

[101]   T. E. Robinson and K. C. Berridge, "The neural basis of drug craving: An incentive-sensitization theory of addiction," *Brain Res. Rev.*, vol. 18, no. 3, pp. 247–291, 1993.

[102]   J. Olds, "Pleasure Centers in the Brain," *Sci. Am.*, vol. 195, no. 4, pp. 105–117, 1956.

[103]   G. Di Chiara, "The role of dopamine in drug abuse viewed from the perspective of its role in motivation," *Drug Alcohol Depend.*, vol. 38, no. 2, pp. 95–137, 1995.

[104]   H. C. Fibiger and A. G. Phillips, "Reward, Motivation, Cognition: Psychobiology of

Mesotelencephalic Dopamine Systems," *Compr. Physiol.*, no. January 2011, 1986.

[105] T. W. Robbins and B. J. Everitt, "Fuctions of dopamine in the dorsal and ventral striatum," *Semin. Neurosci.*, vol. 4, no. 2, pp. 119–128, 1992.

[106] R. A. Rescorla and A. R. Wagner, "A theory of Pavlovian conditioning: Variations in the effectiveness of reinforcement and nonreinforcement," *Class. Cond. II Curr. Res. Theory*, vol. 21, no. 6, pp. 64–99, 1972.

[107] J. Jankovic, "Parkinson's disease: clinical features and diagnosis," *J. Neurol. Neurosurg. Psychiatry*, vol. 79, pp. 368–376, 2008.

[108] W. Dauer and S. Przedborski, "Parkinson's disease: mechanisms and models.," *Neuron*, vol. 39, no. 6, pp. 889–909, Sep. 2003.

[109] A. Carlsson, "Evidence for a role of dopamine in extrapyramidal functions," *Acta Neuroveg. (Wien).*, vol. 26, no. 4, pp. 484–493, Dec. 1964.

[110] A. L. Benabid *et al.*, "Functional neurosurgery for movement disorders: a historical perspective," *Prog. Brain Res.*, vol. 175, pp. 379–391, Jan. 2009.

[111] B. Rosin *et al.*, "Closed-Loop Deep Brain Stimulation Is Superior in Ameliorating Parkinsonism," *Neuron*, vol. 72, no. 2, pp. 370–384, 2011.

[112] B. Panigrahi *et al.*, "Dopamine Is Required for the Neural Representation and Control of Movement Vigor," *Cell*, vol. 162, no. 6, pp. 1418–1430, 2015.

[113] X. Jin and R. M. Costa, "Start/stop signals emerge in nigrostriatal circuits during sequence learning," *Nature*, vol. 466, pp. 457–462, 2010.

[114] N. Kim, J. W. Barter, T. Sukharnikova, and H. H. Yin, "Striatal firing rate reflects head

movement velocity," *Eur. J. Neurosci.*, vol. 40, no. 10, pp. 3481–3490, 2014.

[115] M. W. Howe and D. A. Dombeck, "Rapid signalling in distinct dopaminergic axons during locomotion and reward," *Nature*, vol. 535, pp. 505–510, 2016.

[116] J. W. Barter *et al.*, "Beyond reward prediction errors: the role of dopamine in movement kinematics," *Front. Integr. Neurosci.*, vol. 9, p. 39, 2015.

[117] J. Alves Da Silva, F. Tecuapetla, V. Paixão, and R. M. Costa, "Dopamine neuron activity before action initiation gates and invigorates future movements," *Nature*, vol. 554, pp. 244–248, 2018.

[118] J. J. Day, M. F. Roitman, R. M. Wightman, and R. M. Carelli, "Associative learning mediates dynamic shifts in dopamine signaling in the nucleus accumbens," *Nat. Neurosci.*, vol. 10, no. 8, pp. 1020–1028, 2007.

[119] W. Menegas, B. M. Babayan, N. Uchida, and M. Watabe-Uchida, "Opposite initialization to novel cues in dopamine signaling in ventral and posterior striatum in mice," *Elife*, vol. 6, pp. 1–26, 2017.

[120] K. M. Kim, M. V. Baratta, A. Yang, D. Lee, E. S. Boyden, and C. D. Fiorillo, "Optogenetic mimicry of the transient activation of dopamine neurons by natural reward is sufficient for operant reinforcement," *PLoS One*, vol. 7, no. 4, pp. 1–8, 2012.

[121] E. E. Steinberg, R. Keiflin, J. R. Boivin, I. B. Witten, K. Deisseroth, and P. H. Janak, "A causal link between prediction errors, dopamine neurons and learning," *Nat. Neurosci.*, vol. 16, no. 7, pp. 1–19, 2014.

[122] C. Y. Chang, G. R. Esber, Y. Marrero-Garcia, H. J. Yau, A. Bonci, and G. Schoenbaum,

"Brief optogenetic inhibition of dopamine neurons mimics endogenous negative reward prediction errors," *Nat. Neurosci.*, vol. 19, no. 1, pp. 111–116, 2015.

[123] C. Y. Chang, M. Gardner, M. G. Di Tillio, and G. Schoenbaum, "Optogenetic Blockade of Dopamine Transients Prevents Learning Induced by Changes in Reward Features," *Curr. Biol.*, vol. 27, no. 22, p. 3480–3486.e3, 2017.

[124] K. CHERGUI, M. F. SUAUDCHAGNY, and F. GONON, "Nonlinear Relationship Between Impulse Flow, Dopamine Release and Dopamine Elimination in the Rat-Brain in-Vivo," *Neuroscience*, vol. 62, no. 3, pp. 641–645, 1994.

[125] C. Dugast, M. F. Suaud-Chagny, and F. Gonon, "Continuous in vivo monitoring of evoked dopamine release in the rat nucleus accumbens by amperometry," *Neuroscience*, vol. 62, no. 3, pp. 647–654, 1994.